GEORG-AUGUST-UNIVERSITÄT
GÖTTINGEN

DLR Deutsches Zentrum
für Luft- und Raumfahrt
German Aerospace Center

Master's Thesis

Implementation and Comparison of Slip-flow Boundary Conditions for Perfect Gas Hypersonic Flow Simulations

Implementierung und Gegenüberstellung von Schlupfrandbedingungen zur Simulation von hypersonischen Idealgasströmungen

prepared by

Theresa Hoppe

from Witzenhausen

at the **Deutsches Zentrum für Luft- und Raumfahrt** e.V. (DLR)
German Aerospace Center, Institute of Aerodynamics and Flow Technology,
Spacecraft Department

Thesis period:	6th June 2019 until 21st December 2019
Supervisor:	Prof. Dr. Klaus Hannemann
First referee:	Prof. Dr. rer. nat. Dr.-Ing. habil. Andreas Dillmann
Second referee:	Prof. Dr. Klaus Hannemann

Contents

Nomenclature

Latin Letters

Scalar Quantities

A	Reference area	$[\mathrm{m}^2]$
A_i	Area of surface segment	$[\mathrm{m}^2]$
c_p	Specific heat at constant pressure	$[\mathrm{J\,kg^{-1}\,K^{-1}}]$
c_v	Specific heat at constant volume	$[\mathrm{J\,kg^{-1}\,K^{-1}}]$
C_D	Drag coefficient	–
C_f	Friction coefficient	–
C_h	Heating coefficient	–
C_L	Lift coefficient	–
C_N	Normal-force coefficient	–
C_p	Pressure coefficient	–
C_T	Tangential-force coefficient	–
D	Drag	[N]
e	Internal energy per unit mass	$[\mathrm{J\,kg^{-1}}]$
E	Energy per unit mass	$[\mathrm{J\,kg^{-1}}]$
E_in	Energy from heat conduction	$[\mathrm{J\,s^{-1}}]$
E_S	Work done by surface forces	$[\mathrm{J\,s^{-1}}]$
E_V	Work done by body forces	$[\mathrm{J\,s^{-1}}]$
f	Product of surface and face normal vector	$[\mathrm{m}^2]$
f_S	Surface forces	[N]
f_V	Body forces	[N]
h	Wall distance	[m]
Kn	Knudsen number	–
Kn_GLL	Gradient-length local Knudsen number	–
L_c	Characteristic dimension	[m]
L	Lift	[N]
M	Total mass in control volume	[kg]
Ma	Mach number	–
N	Number of grid points	
p	Pressure	$[\mathrm{N\,m^{-2}}]$
Pr	Prandtl number	–
q	Heat flux	$[\mathrm{J\,s^{-1}\,m^{-2}}]$
q_i	Components of heat flux vector	$[\mathrm{J\,s^{-1}\,m^{-2}}]$
Q	Heat flow	$[\mathrm{J\,s^{-1}}]$

r, s, t	Wall normal and tangential velocity components	$[\mathrm{m\,s^{-1}}]$
r_c	Convergence order	–
R	Specific gas constant	$[\mathrm{J\,kg^{-1}\,K^{-1}}]$
Re	Reynolds number	–
S	Surface of the control volume	$[\mathrm{m^2}]$
S_c	Sutherland constant	[K]
S_i	Surface segment of the control volume	$[\mathrm{m^2}]$
T	Temperature	[K]
ΔT	Temperature jump	[K]
t	Time	[s]
U	Velocity	$[\mathrm{m\,s^{-1}}]$
u, v, w	Velocity components in Cartesian coordinates	$[\mathrm{m\,s^{-1}}]$
V	Control volume	$[\mathrm{m^3}]$

Vector Quantities

$\mathbf{F}, \mathbf{G}, \mathbf{H}$	Flux vectors	$[\mathrm{kg\,m^{-2}\,s^{-1}}]$, $[\mathrm{J\,m^{-2}\,s^{-1}}]$, $[\mathrm{N\,m^{-1}\,s^{-1}}]$
$\mathbf{F}_i$	Face normal vector of face F_i	$[\mathrm{m^2}]$
$\mathbf{f}$	Force vector	[N]
$\mathbf{f}_\mathrm{loc}$	Local force on surface element	[N]
$\mathbf{f}_\mathrm{N}$	Local normal force on surface element	[N]
$\mathbf{f}_\mathrm{T}$	Local tangential force on surface element	[N]
$\mathbf{g}$	Volume force vector	[N]
$\mathbf{l}, \mathbf{m}$	Tangential basis vectors	–
$\mathbf{n}$	Surface normal vector	–
$\mathbf{Q}$	Heat flux vector	$[\mathrm{J\,s^{-1}\,m^{-2}}]$
$\mathbf{Q}_\mathrm{T}$	Heat flux tangential to surface	$[\mathrm{J\,s^{-1}\,m^{-2}}]$
$\mathbf{T}$	Stress vector	$[\mathrm{N\,m^{-2}}]$
$\mathbf{u}$	Velocity vector	$[\mathrm{m\,s^{-1}}]$
$\mathbf{U}$	Vector of conserved variables	$[\mathrm{kg\,m^{-3}}]$, $[\mathrm{kg\,m^{-2}\,s^{-1}}]$, $[\mathrm{N\,m^{-2}}]$
$\bar{\mathbf{x}}$	Centre of control volume	[m]
$\bar{\mathbf{x}}_i$	Centre of surface segment	[m]

Tensor Quantities

$\mathcal{H}$	Flux tensor	$[\mathrm{kg\,m^{-2}\,s^{-1}}]$, $[\mathrm{J\,m^{-2}\,s^{-1}}]$, $[\mathrm{N\,m^{-1}\,s^{-1}}]$
K	Transformation matrix	–

$\mathcal{S}$	Tensor that eliminates normal components	–
$\mathcal{T}$	Stress tensor	$[\mathrm{N\,m^{-2}}]$
I	Unit tensor	–
$\mathit{\Pi}$	Viscous component of stress tensor	$[\mathrm{N\,m^{-2}}]$

Greek Letters

α	Thermal accommodation coefficient	–
γ	Ratio of specific heats	–
ε	Deviation from finest grid	–
κ	Thermal conductivity	$[\mathrm{J\,s^{-1}\,m^{-1}\,K^{-1}}]$
λ	Mean free path	[m]
λ_T	"Thermal" mean free path	[m]
μ	Dynamic viscosity	[Pa s]
ρ	Density	$[\mathrm{kg\,m^{-3}}]$
σ	Momentum accommodation coefficient	–
τ	Shear stress	$[\mathrm{N\,m^{-2}}]$
$\boldsymbol{\tau}$	Tangential shear stress vector	$[\mathrm{N\,m^{-2}}]$
Φ	Cylinder angle	[deg]

Super- and subscripts

i	inviscid
np	near point
ref	reference property
s	slip property
v	viscous
w	wall property
wp	wall point
λ	At a distance of one mean free path from the surface
∞	Free-stream property

Abbreviations

AOA	Angle of attack
CFD	Computational fluid dynamics
DSMC	Direct simulation Monte Carlo
MEMS	Microelectromechanical systems
SPARTA	Stochastic PArallel Rarefied-gas Time-accurate Analyzer
SHEFEX	SHarp-Edge-Flight-EXperiment

1. Introduction

1.1. Motivation

Upon re-entry into the earth's atmosphere, a hypersonic vehicle experiences a continuous increase in the density of the surrounding fluid. Coming from a highly rarefied atmosphere, the vehicle passes various flow regimes. At high altitudes, molecular collisions with the vehicle's surface dominate the airflow around the vehicle. This regime is known as the *free molecular regime*. While approaching the earth's surface, the atmosphere will get progressively denser until the vehicle reaches the *continuum regime*, in which the surrounding gas is no longer considered as individual molecules but as a continuum. In between these two regimes, the vehicle passes the *transition* and *slip regime*, where slip effects at the surface, such as *velocity slip* and *temperature jump*, become relevant [1, p. 20f.]. For the design and construction of hypersonic vehicles and re-entry configurations, it is essential to accurately predict the aerodynamic forces and the heat transfer throughout all of those flow regimes. Rarefaction effects impact the design of the thermal protection system and compromise the aerodynamic efficiency of the vehicle [2].

In the last decades, computing capacities have increased majorly and computational fluid dynamics has become a popular tool for simulations in the rarefied flow regime, where experiments become rather complex and hard to conduct. The Direct Simulation Monte Carlo (DSMC) method provides accurate results in the complete Knudsen number range, but it becomes computationally expensive towards lower Knudsen numbers. Common Navier-Stokes solvers are more efficient but they are limited to the continuum regime due to the range of validity of the Navier-Stokes equations. Therefore, it is the subject of current research to extend the validity of the Navier-Stokes equations by applying a set of non-equilibrium boundary conditions. To do so, the conventional *no-slip* boundary condition is replaced by a velocity slip condition and a temperature jump condition is introduced at the solid-fluid interface.

1.2. Review of Non-Equilibrium Boundary Conditions

Non-equilibrium boundary conditions are widely researched in the field of hypersonics. With the increasing popularity of microelectromechanical systems (MEMS) [3], slip-flow conditions are becoming of interest in small-scale flows through micro- or nanochannels (microfluidics) [4, 5]. Due to the complexity of the topic, this review focuses merely on the field of hypersonics.

Over the last decades, a wide variety of non-equilibrium boundary conditions has been proposed in the literature. The most commonly used conditions are the velocity slip given by Maxwell [6] combined with the temperature jump condition from Smoluchowski [7]. The Maxwell slip condition allows a finite fluid velocity at the wall, which is proportional to the tangential shear stress at the wall. The Smoluchowski condition introduces a temperature jump at the surface so that the fluid at the wall and the wall itself are no longer in thermal equilibrium. The temperature jump depends on the temperature gradient normal to the wall. From here on, both conditions are referred to as the Maxwell boundary conditions for simplicity.
In contrast to the conventional no-slip condition, the use of Maxwell boundary conditions improves the prediction of surface properties, such as drag, surface pressure and heat transfer for non-continuum flows. Though, towards larger Knudsen numbers, the results obtained with the Maxwell conditions still show significant deviations from reference DSMC data [8–10]. Votta et al. [11], however, found them to be a "good compromise between computational cost and accuracy".

Based on the Maxwell boundary conditions, Gökçen et al. [9] introduced a generalised form of the velocity slip and temperature jump equations. In their study, Gökçen et al. extended the applicability of the Maxwell conditions into the transition and free-molecule regime. In contrast to computing the velocity and temperature slip directly at the wall, the generalised boundary conditions calculate the velocity and temperature of the fluid at a distance of one mean free path away from the wall (see sec. 2.3.2). At large Knudsen numbers, these conditions showed a significant improvement in the prediction of the integral drag coefficient of a flat plate compared to the standard Maxwell conditions.
Lofthouse et al. [8, 12] tested various slip boundary conditions and found the generalised slip conditions to agree best with the surface properties predicted by DSMC

simulations. However, in contrast to the Maxwell boundary conditions, the generalised conditions increased the computational expense [8, 13].

Lockerby et al. [14] comment that the application of the standard Maxwell slip condition is inaccurate for curved surfaces or surfaces that are moved in space. The original Maxwell velocity slip condition was derived for a planar wall. Expressing the slip condition in its three-dimensional tensor form, yields an additional curvature term, that is proportional to the change of the wall-normal velocity along the wall. Including the curvature term in the common Maxwell conditions reduces the deviation from DSMC results or theoretical values for the drag force and the slip velocity [13–16].

The contribution of thermal creep, describing a fluid motion from colder to warmer regions, was already included in Maxwell's originally derived slip condition. Lofthouse [2] states that the contribution of thermal creep is negligible for isothermal walls and the term is ignored further in the generalised conditions by Gökçen et al. [9]. Though, in newer studies [17–19] the thermal creep term, as well as the curvature term, is treated as a fundamental component of the slip-flow boundary conditions.

Le et al. [18] extended the temperature jump condition to incorporate the effect of heat generation due to "sliding friction". In the slip regime, the heat transfer to the wall is composed of two terms, the general heat conduction term based on Fourier's law and a friction term based on the slip velocity of the fluid [9, 20]. Incorporating the friction term into the derivation of the temperature jump condition extends the condition by a velocity-dependent term.
The boundary condition was tested for a hypersonic flow over a flat plate and a sharp biconic configuration, as well as for a supersonic flow over a microairfoil [21]. Improved agreement of computational fluid dynamics (CFD) simulations with DSMC data was observed for the surface gas temperature and the heat flux.

Assam et al. [22] investigated Le's new temperature jump condition for a hypersonic flat plate case and found that the surface pressure is overestimated at the leading edge. They include an additional pressure jump condition, as previously proposed by Greenshields et al. [19], to correct the observed pressure overshoot. If combined

with the Le temperature jump condition, the pressure jump condition gives good results without substantially influencing other flow properties. Adding the pressure jump condition to the standard Maxwell conditions showed only minor changes of the heat flux and surface pressure distribution along the plate. Overall, the use of a pressure jump condition is unclear and requires further testing [19, 22].

A different approach to enhance the standard Maxwell conditions is to expand it to higher orders. In contrast to the conditions described above, higher-order boundary conditions use the Burnett formulation of the stress tensor and heat flux vector instead of the formulations used in the Navier-Stokes equations. Inserting the Burnett formulations into the Maxwell conditions yields conditions of second order in the velocity and temperature derivatives. The results from this boundary condition agree well with experimental data for a Poiseuille flow. [14]
When applying a simplified version of the second-order conditions to a flat plate case, Le et al. [16] found that there is only a slight improvement of the surface pressure, surface gas temperature and slip velocity compared to the standard Maxwell conditions. In general, there exists a large variety of second-order conditions, reviewed e.g. in [4, 5, 23], but their application appears to be focused mainly on small-scale topologies, such as micro- or nanochannels.

In her master's thesis, Winkler [24] integrated the Maxwell conditions into the DLR TAU-code by approximating the velocity and temperature derivatives through a difference quotient between neighbouring grid points. When compared to DSMC data, the slip-flow conditions showed clear improvements in the predicted skin friction and heat transfer coefficients for a cylinder case. However, changes in the pressure coefficient were only minor or showed even stronger deviations from the DSMC data compared to the no-slip solution.
When tested on the SHEFEX III (SHarp-Edge-Flight-EXperiment) configuration for Knudsen numbers near the continuum regime, the Maxwell conditions slightly improved the prediction of the aerodynamic efficiency. Simultaneously, the surface pressure and shear stress on the leeward side of the configuration were over-predicted with and without slip conditions. [25]

1.3. Scope of this Work

The goal of this work is to improve the existing implementation of the Maxwell boundary conditions in the DLR TAU-code. Due to its simplicity and fundamental role in the derivation of more complex boundary conditions, we choose to re-implement the Maxwell boundary conditions. In contrast to the difference quotient approach by Winkler [24], we attempt using the code's existing velocity and temperature gradient data structure. Proceeding from this, we extended the code with the generalised slip conditions proposed by Gökçen et al. [9]. In a final step, the curvature and thermal creep terms were incorporated to use with both conditions.
We analysed whether the new implementation compromises the convergence order of the TAU-solver and subsequently applied it to a variety of test cases. As a first test case, we simulated Gökçen's flat plate case [9] for the whole Knudsen number range and analysed how the boundary conditions affect the drag coefficient of the plate. The second test case was Metcalf's flat plate case [26], which is widely used to assess new boundary conditions [16, 18, 22, 27]. Furthermore, to investigate the effect of the curvature term, we simulated Lofthouse's cylinder case [8] and then proceeded to the three-dimensional SHEFEX III configuration for angles of attack of 30° and 0°.
For each case, the different boundary conditions were compared based on the aerodynamic and heat transfer coefficients, and their agreement with reference DSMC and experimental data, if available, was tested.

2. Theoretical Background

This section introduces the governing equations in fluid dynamics and discusses their validity throughout the different flow regimes. The range of validity of the Navier-Stokes equations can be extended through the choice of different slip flow boundary conditions, that are presented here.

2.1. Flow Regimes and Gas Models

Generally, a gas flow can be described on the macroscopic or microscopic scale. On the macroscopic level, the gas is treated as a continuum and the macroscopic flow properties, including velocity, temperature, density and pressure, are given by the Navier-Stokes equations. On the microscopic level, a gas flow is described by the molecular model or discrete particle model, which treats the gas as individual particles. The governing equation for this model is the Boltzmann equation [28, p. 1f.].

While the Boltzmann equation is valid for all dilute flow regimes, the Navier-Stokes and Euler equations are only valid for continuum flows (fig. 2.1). In the case of continuum flow, the mean free path λ of the gas is considerably smaller than the characteristic dimension of the body and the gas particles collide so frequently with the body that it experiences the gas as a continuum. On the other hand, if the mean free path is of the same dimension as the body, collisions are less frequent and the body can distinguish between individual particles. This kind of flow is called free molecular flow [29]. To better categorise the different flow regimes, the *Knudsen number* is introduced as a similarity parameter [1, p. 21]:

$$\mathrm{Kn} = \frac{\lambda}{L_\mathrm{c}}$$

where L_c denotes the characteristic dimension of the body. For a flat plate, the characteristic dimension is given by the length of the plate. In continuous media,

the mean free path is calculated based on the viscosity μ, density ρ and temperature T of the gas [2]:

$$\lambda = \frac{\mu}{\rho}\sqrt{\frac{\pi}{RT}}$$

with the specific gas constant R.

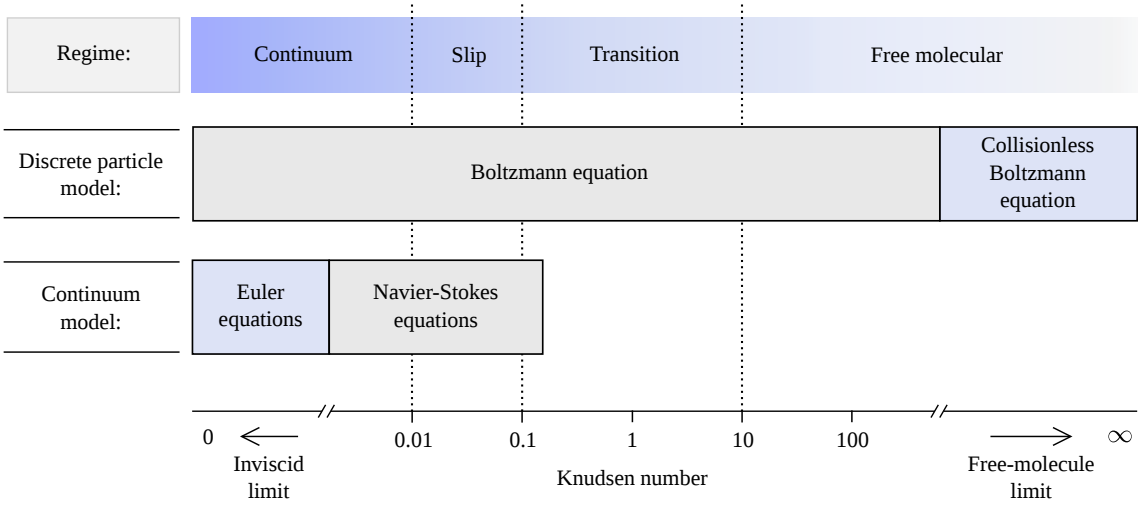

Figure 2.1.: Limits of the governing equations in fluid dynamics. Adapted from [5, 30].

Based on the Knudsen number, Schaaf and Chambre [31] originally introduced a classification of gas flows into four flow regimes, as depicted in fig. 2.1. In their review, Zhang et al. [5] summarise this classification and support it with examples from current research:

Continuum regime ($\mathrm{Kn} < 10^{-2}$): In this regime, the description of the fluid as a continuum in thermodynamic equilibrium is valid and the Navier-Stokes equations with the ordinary no-slip boundary condition apply.

Slip flow regime ($10^{-2} < \mathrm{Kn} < 10^{-1}$): The no-slip boundary condition is no longer valid but the Navier-Stokes equations still provide an accurate description of the bulk flow. Introducing the slip flow boundary conditions at the wall extends the range of validity of the Navier-Stokes equations.

Transition regime ($10^{-1} < \mathrm{Kn} < 10$): The continuum and thermodynamic equilibrium assumptions start to collapse because rarefaction effects prevail. Close to the Knudsen layer the relation between stress and strain develops non-linearities, making the slip boundary conditions more complex. Here the use of other methods,

such as DSMC or higher order methods should be considered.

Free molecular regime (Kn $>$ 10): Gas-surface interactions dominate the flow behaviour, thus collisions between the individual gas molecules become negligible. The Navier-Stokes equations no longer apply.

2.2. Governing Equations

In the previous section, the validity of the governing equations throughout the different flow regimes was discussed. This section summarises the derivation of the Navier-Stokes equations and the concepts behind them.

In general, the Navier-Stokes equations are based on the conservation of *mass*, *momentum* and *energy*. These conservation laws can be expressed through a set of differential equations or a set of integral equations, which are referred to as their differential or integral forms. [32, p. 3ff.]
Since the integral form is based on relations for a fixed control volume and its surface, it is well suited for a computational approach, such as the finite volume method (sec. 3.1). Only the integral form of the governing equations is presented here, the differential form can be found for example in [32, p. 25f.].

The description and interpretation of the equations mentioned in this section are taken from [32, Ch. 1] if not stated otherwise.

2.2.1. Conservation of Mass

Beginning with the conservation of mass, the total mass M inside of a control volume V is given through the volume integral of the density ρ. The time rate of change of the total mass M is then given by the material derivative:

$$\frac{\mathrm{D}M}{\mathrm{D}t} = \iiint_V \frac{\partial \rho}{\partial t}\,\mathrm{d}V + \iint_S \mathbf{n}\cdot(\rho\mathbf{u})\,\mathrm{d}S \qquad \text{with} \qquad M = \iiint_V \rho\,\mathrm{d}V \tag{2.1}$$

Here, S denotes the surface of the control volume, $\mathbf{n}$ the outward pointing normal vector and $\mathbf{u}$ the fluid velocity. Without sources or sinks of mass inside of the control volume the material derivative is equal to zero and equ. (2.1) turns into the *continuity equation*. For a finite control volume fixed in space and time the continuity equation

is given by:

$$\frac{\mathrm{d}}{\mathrm{d}t}\iiint_V \rho \,\mathrm{d}V = -\iint_S (\rho\mathbf{u})\cdot\mathbf{n}\,\mathrm{d}S \tag{2.2}$$

The left-hand side of equ. (2.2) is the time rate of change of mass contained within the control volume. The right-hand side describes the net mass flow through the boundaries of the control volume. Thus, with no sources or sinks the only way to change the enclosed mass inside of the control volume is by a flux of mass through the volume's surface.

2.2.2. Conservation of Momentum

The conservation law of momentum is a direct result from Newton's second law: "the time rate of change of the momentum in V is equal to the total force acting on the volume V" [32, p. 22]. The total force on the volume is composed of two components: *body forces* and *surface forces*. Body forces act on the whole volume of the body, such as gravity or electromagnetic forces. In contrast, surface forces act solely on the surface of the body, such as pressure or viscous forces. [33, p. 61–63] Let Φ be the total momentum in the control volume V, then Newton's second law states:

$$\frac{\mathrm{D}\Phi(t)}{\mathrm{D}t} = f_S + f_V \qquad \text{with} \qquad \Phi(t) = \iiint_V \rho\mathbf{u}\,\mathrm{d}V$$

where the terms f_S and f_V denote the surface and body forces. Applying the material derivative to the total momentum yields the conservation law of momentum for a fixed control volume:

$$\begin{aligned}\frac{\mathrm{d}}{\mathrm{d}t}\iiint_V (\rho\mathbf{u})\,\mathrm{d}V &= -\iint_S \mathbf{u}(\mathbf{n}\cdot\rho\mathbf{u})\,\mathrm{d}S + f_S + f_V \\ &= -\iint_S \mathbf{u}(\mathbf{n}\cdot\rho\mathbf{u})\,\mathrm{d}S + \iint_S \mathbf{T}\,\mathrm{d}S + \iiint_V \rho\mathbf{g}\,\mathrm{d}V \end{aligned} \tag{2.3}$$

The body forces are given by the volume integral over the specific volume-force vector $\mathbf{g}$, which summarises all contributing volume forces. The surface forces f_S are given through the surface integral over the stress vector $\mathbf{T} = \mathbf{n}\cdot\mathcal{T}$, with $\mathcal{T}$ denotes the stress tensor. The stress tensor may be separated into two components,

a pressure component $-pI$, where I is the unit tensor, and a viscous component $\mathit{\Pi}$:

$$I = \begin{pmatrix} 1 & 0 & 0 \\ 0 & 1 & 0 \\ 0 & 0 & 1 \end{pmatrix} \qquad \text{and} \qquad \mathit{\Pi} = \begin{pmatrix} \tau_{xx} & \tau_{xy} & \tau_{xz} \\ \tau_{yx} & \tau_{yy} & \tau_{yz} \\ \tau_{zx} & \tau_{zy} & \tau_{zz} \end{pmatrix}$$

By inserting the stress tensor components into equ. (2.3), one obtains the Navier-Stokes equation in its integral form:

$$\frac{\mathrm{d}}{\mathrm{d}t} \iiint_V (\rho \mathbf{u})\, \mathrm{d}V = - \iint_S \left[\mathbf{u}(\mathbf{n} \cdot \rho\mathbf{u}) + p\mathbf{n} - \mathbf{n} \cdot \mathit{\Pi}\right]\, \mathrm{d}S + \iiint_V \rho \mathbf{g}\, \mathrm{d}V \tag{2.4}$$

The left-hand side of equ. (2.4) describes the time rate of change of the total momentum inside of the control volume. The right-hand side describes the sources of this change, which are the net flux of momentum into the control volume along with the surface and body forces.

2.2.3. Conservation of Energy

Given the total energy $\Psi(t)$ of the control volume, one obtains its rate of change by summing up the inflow of energy due to heat conduction E_{in}, and the work done by the body and surface forces E_S and E_V:

$$\frac{\mathrm{D}\Psi}{\mathrm{D}t} = E_{\text{in}} + E_S + E_V \qquad \text{with} \qquad \Psi(t) = \iiint_V \rho E\, \mathrm{d}V$$

The work done by body and surface forces, per unit time, is easily attained from $E = \mathbf{u} \cdot \mathbf{f}$, where $\mathbf{f}$ is the corresponding force. Applying the material derivative as before and introducing the heat flux vector $\mathbf{Q}$ yields the formulation of the conservation law of energy:

$$\begin{aligned} \frac{\mathrm{d}}{\mathrm{d}t} \iiint_V \rho E\, \mathrm{d}V &= - \iint_S (\mathbf{n} \cdot E\mathbf{u})\, \mathrm{d}S + E_{\text{in}} + E_S + E_V \\ &= - \iint_S \left[\mathbf{n} \cdot (E\mathbf{u} + p\mathbf{u} + \mathbf{Q}) - \mathbf{u} \cdot (\mathbf{n} \cdot \mathit{\Pi})\right]\, \mathrm{d}S + \iiint_V \rho(\mathbf{u} \cdot \mathbf{g})\, \mathrm{d}V \end{aligned} \tag{2.5}$$

Again, the left-hand side describes the time rate of change of the total energy inside of the control volume. The right-hand side contains the net flux of energy through

the volume's boundaries, the work done by the pressure, viscous and volume forces, and the heat flux driven by gradients in the temperature distribution.

Strictly speaking, the Navier-Stokes-equations only describe the law of conservation of momentum (equ. (2.3)). However, often the whole set of equ. (2.2),(2.4) and (2.5) is referred to as the Navier-Stokes equations, as is the case here.

2.2.4. Closure Conditions

The Navier-Stokes equations, containing more unknowns than equations, are an undetermined system. Thus, closure conditions are required to fully describe the dynamics of the system. This section is based on [33, p. 79].

The total energy per unit mass E is given through the internal energy e of the gas and its kinetic energy:

$$E = \left(e + \frac{\mathbf{u}^2}{2} \right)$$

So far, this only substitutes E with the internal energy e in the list of unknowns. Assuming a perfect gas, the internal energy is determined by the temperature T:

$$e = c_v T$$

with the specific heat at constant volume c_v. The temperature required to compute the internal energy is obtained by the equation of state:

$$p = \rho R T$$

For a given temperature, the viscosity is calculated through Sutherland's viscosity law [34]:

$$\frac{\mu}{\mu_{\text{ref}}} = \left(\frac{T}{T_{\text{ref}}} \right)^{\frac{3}{2}} \cdot \frac{T_{\text{ref}} + S_{\text{c}}}{T + S_{\text{c}}}$$

where S_{c} is the material-specific Sutherland constant and μ_{ref} and T_{ref} denote the reference viscosity and temperature. Furthermore, the heat flux $\mathbf{Q}$ is given by

Fourier's law of heat conduction [32, p. 17]:

$$\mathbf{Q} = -\kappa \cdot \boldsymbol{\nabla} T$$

with the thermal conductivity κ, which can be computed from the Prandtl number Pr [1, p. 292]

$$\mathrm{Pr} = \frac{\mu c_p}{\kappa} \quad \Rightarrow \quad \kappa = \frac{\mu c_p}{\mathrm{Pr}}$$

where c_p denotes the specific heat at constant pressure.

2.3. Slip-Flow Boundary Conditions

Conventionally, the Navier-Stokes equations are solved using the no-slip boundary condition, which states that the gas velocity at a stationary wall is equal to zero. In a rarefied regime, however, this assumption appears to be invalid. As depicted in figure 2.2, the slip boundary condition allows the gas at the wall to possess a finite velocity u_s, called the *slip velocity* [1, p. 20][35].
In the following, only stationary surfaces are considered and thus the velocity of the wall is always equal to zero.

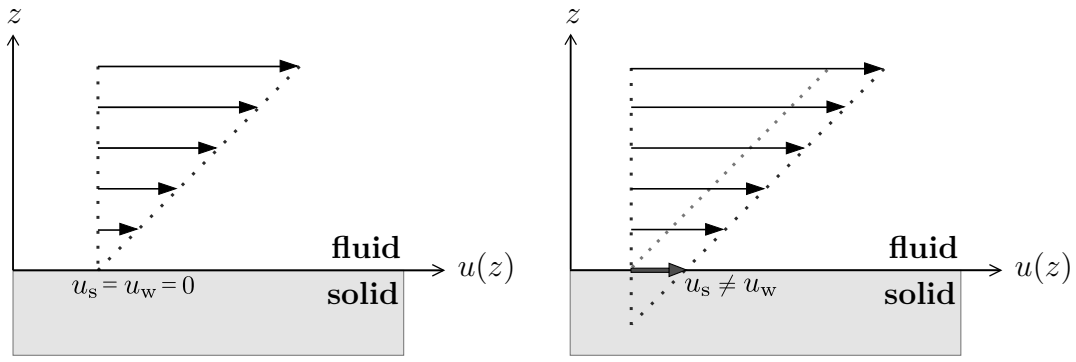

Figure 2.2.: Schematic depiction of the velocity profile close to the wall with the no-slip boundary condition (left) and with slip-flow boundary conditions (right). The slip-flow conditions allow for a finite velocity at the wall, enabling the gas to flow faster over the surface. Adapted from [35].

Similarly, for an isothermal wall in the continuum regime the gas and the wall are assumed to be in thermal equilibrium. Yet, the temperature of a rarefied gas at the surface is not restricted to the wall temperature. The slip-flow boundary conditions

allow a temperature jump ΔT between the wall temperature and the temperature of the gas in contact with the wall [1, p. 20][35], depicted in fig. 2.3.

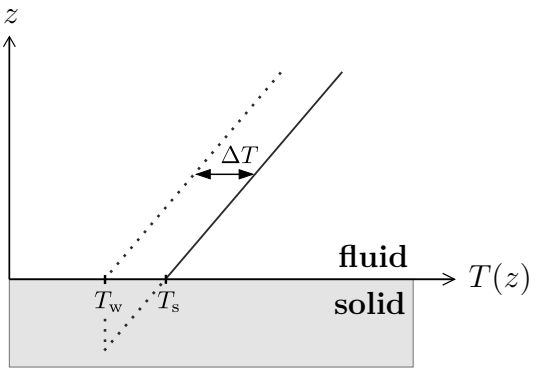

Figure 2.3.: Depiction of the temperature jump ΔT in a rarefied gas. With the no-slip boundary condition, the gas temperature is equal to the wall temperature T_w. The slip condition, however, allows for a different slip temperature T_s. Adapted from [35].

2.3.1. Maxwell Slip

As proposed by Maxwell [6], a velocity slip at an object's surface occurs when the characteristic length of the object is of the same order of magnitude as the mean free path λ of the surrounding fluid. Maxwell originally derived the following expression for the slip velocity u_s along a flat plate at rest [2]:

$$u_\mathrm{s} = \left(\frac{2-\sigma}{\sigma}\right)\lambda\frac{\partial u}{\partial n} + \frac{3}{4}\frac{\mu}{\rho T}\frac{\partial T}{\partial x} \tag{2.6}$$

with u marking the x-component of the velocity and σ the tangential momentum accommodation coefficient. Here, the plate is aligned parallel to the x-direction and n is marking the direction normal to the wall. The second term on the right-hand side of equ. (2.6) accounts for the effect of thermal creep, describing the flow of a rarefied gas from colder to warmer areas. This phenomenon was first observed by Reynolds [14]. According to Lofthouse [2], the thermal creep term is negligible for isothermal walls. In the following sections, only the first term in equ. (2.6) will be referred to as Maxwell slip and the thermal creep term will be treated as an additional term. Based on the velocity slip, a similar relation was derived for the temperature jump [2]:

$$\Delta T = T_\mathrm{s} - T_\mathrm{w} = \frac{2-\alpha}{\alpha}\frac{2\gamma}{(\gamma+1)\mathrm{Pr}}\lambda\frac{\partial T}{\partial n} \tag{2.7}$$

with the thermal accommodation coefficient α and the ratio of specific heats γ. In this work, the thermal accommodation coefficient is assumed to be equal to the

momentum accommodation coefficient σ. Introducing a "thermal" mean free path λ_T, the equation for the temperature jump is transformed into a similar form as equ. (2.6) [8]:

$$T_\mathrm{s} - T_\mathrm{w} = \frac{2-\sigma}{\sigma}\lambda_T \frac{\partial T}{\partial n} \qquad \text{with} \qquad \lambda_T = \frac{2}{(\gamma+1)}\frac{\kappa}{\rho c_v}\sqrt{\frac{\pi}{2RT}} \tag{2.8}$$

A derivation of equ. (2.6) and (2.7) can be found in [27].

2.3.2. Generalised Slip

The Maxwell slip conditions were derived for flows near the continuum regime. For large Knudsen numbers near the free molecular regime, these conditions fail to accurately predict the surface properties, such as skin friction and heat transfer. Gökçen and McCormack [9] introduced a generalised velocity slip condition, that reduces to equ. (2.6) for near-continuum Knudsen numbers but approaches the correct limits of skin friction and heat transfer in the free molecular regime [9]:

$$u_\lambda = \frac{2\lambda}{\sigma}\frac{\partial u}{\partial n} \tag{2.9}$$

Here, u_λ describes the tangential velocity at a distance of one mean free path away from the wall. Analogously, the temperature jump can be generalised to [8]:

$$T_\lambda - T_\mathrm{w} = \frac{2\lambda_T}{\sigma}\frac{\partial T}{\partial n} \tag{2.10}$$

where T_λ denotes the temperature at a distance of one mean free path away from the wall. The velocity and temperature at the wall are then computed through interpolation or, for small Knudsen numbers, by evaluating u_λ and T_λ through a Taylor expansion.

In order to maintain the same computational expense as the Maxwell slip, we treat the generalised slip as boundary conditions at the wall. Thus, instead of computing the flow properties at one mean free path away from the wall, we calculate them directly at the wall:

$$u_\mathrm{s} = \frac{2\lambda}{\sigma}\frac{\partial u}{\partial n} \quad \text{and} \quad T_\mathrm{s} - T_\mathrm{w} = \frac{2\lambda_T}{\sigma}\frac{\partial T}{\partial n} \tag{2.11}$$

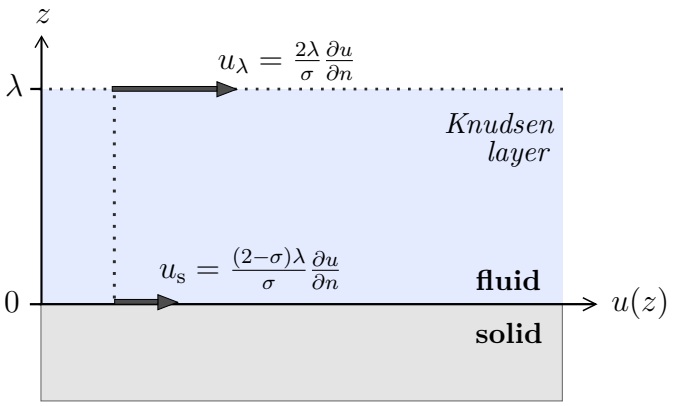

Figure 2.4.: Comparison between the Maxwell and generalised slip condition. The Maxwell slip computes the velocity and temperature values at the solid-fluid interface, while the generalised slip condition calculates the velocity and temperature at a distance of one mean free path away from the surface.

2.3.3. Additional Terms

For the application to three-dimensional flows, Maxwell's original slip condition can be converted into tensorial form [27]:

$$\begin{aligned}\mathbf{u}_\mathrm{s} &= \left(\frac{2-\sigma}{\sigma}\right)\frac{\lambda}{\mu}\cdot\boldsymbol{\tau} - \frac{3}{4}\frac{\mathrm{Pr}(\gamma-1)}{\gamma p}\cdot\mathbf{Q}_\mathrm{T} \\ &= \left(\frac{2-\sigma}{\sigma}\right)\frac{\lambda}{\mu}\cdot\mathcal{S}\cdot(\mathbf{n}\cdot\mathit{\Pi}) - \frac{3}{4}\frac{\mathrm{Pr}(\gamma-1)}{\gamma p}\cdot(\mathbf{Q}\cdot\mathcal{S})\end{aligned} \tag{2.12}$$

where $\boldsymbol{\tau}$ denotes the tangential shear stress and $\mathbf{Q}_\mathrm{T}$ the tangential heat flux at the surface. To eliminate the normal components of the shear stress vector $(\mathbf{n}\cdot\mathit{\Pi})$ and the heat flux vector $\mathbf{Q}$, they are multiplied with the tensor $\mathcal{S} = I - \mathbf{n}\otimes\mathbf{n}$. Here, $\mathbf{n}$ is the surface normal vector pointing into the flow domain and I the unit tensor. The tensor product is given by $\mathbf{n}\otimes\mathbf{n}$.
The second term on the right-hand side of equ. (2.12) describes the thermal creep term, as discussed before in sec. 2.3.1. For a flat plate aligned in the xy-plane and a given velocity vector $\mathbf{u} = (u, v, w)$, the above equation simplifies to:

$$\begin{pmatrix} u_\mathrm{s} \\ v_\mathrm{s} \\ w_\mathrm{s} \end{pmatrix} = \left(\frac{2-\sigma}{\sigma}\right)\lambda\cdot\left[\begin{pmatrix} \partial_z u \\ \partial_z v \\ 0 \end{pmatrix} + \begin{pmatrix} \partial_x w \\ \partial_y w \\ 0 \end{pmatrix}\right] + \frac{3}{4}\frac{\mathrm{Pr}(\gamma-1)}{\gamma p}\cdot\kappa\begin{pmatrix} \partial_x T \\ \partial_y T \\ 0 \end{pmatrix} \tag{2.13}$$

Comparing the first term on the right-hand side of equ. (2.13) with equ. (2.6), one observes that the expression for the shear stress is extended by an additional term. This term is accounting for surface curvature and moving surfaces [14].

2.3.4. Heat Transfer Extension

With conventional boundary conditions, the heat transfer at the wall is given by Fourier's law of heat conduction [1, p. 26]:

$$q = -\kappa \cdot \frac{\partial T}{\partial n}$$

When slip-flow boundary conditions are employed, the wall experiences an additional heat transfer due to the sliding friction of the fluid. This heat transfer is proportional to the slip velocity and the shear stress at the wall [18]:

$$q = -\kappa \cdot \frac{\partial T}{\partial n} - \mathbf{u}_\mathrm{s} \cdot \boldsymbol{\tau}$$

where the shear stress is given through $\boldsymbol{\tau} = \mathcal{S} \cdot (\mathbf{n} \cdot \mathit{\Pi})$, as in the previous section. For planar geometries, the shear stress is reduced to the velocity gradient normal to the surface [9]:

$$q = -\kappa \cdot \frac{\partial T}{\partial n} - \mathbf{u}_\mathrm{s} \cdot \frac{\partial \mathbf{u}_\mathrm{s}}{\partial n} \tag{2.14}$$

For non-planar surfaces, however, the complete shear stress has to be adapted. With z marking the surface normal direction and x, y the direction tangential to the surface, the heat transfer is then given by:

$$q = -\kappa \cdot \frac{\partial T}{\partial z} - \mu \cdot \begin{pmatrix} u_\mathrm{s} \\ v_\mathrm{s} \\ w_\mathrm{s} \end{pmatrix} \cdot \left[\begin{pmatrix} \partial_z u \\ \partial_z v \\ 0 \end{pmatrix} + \begin{pmatrix} \partial_x w \\ \partial_y w \\ 0 \end{pmatrix} \right] \tag{2.15}$$

3. Numerical Methods

The CFD-solutions in this study are computed with the DLR TAU-code [36], a numerical solver for the Navier-Stokes equations based on a finite volume approach. Furthermore, reference DSMC data are either taken from literature or calculated with the Stochastic PArallel Rarefied-gas Time-accurate Analyzer (SPARTA) code [37, 38]. This section shortly introduces the finite volume method and the DSMC method.

3.1. Finite Volume Method

For hypersonic flows, like the ones considered in this study, the body forces on a control volume become negligible compared to the surface forces. The Navier-Stokes equations may then be written as one single equation [32, p. 103]:

$$\frac{\mathrm{d}}{\mathrm{d}t}\iiint_V \mathbf{U}\,\mathrm{d}V = -\iint_S \mathcal{H}\cdot\mathbf{n}\,\mathrm{d}S \tag{3.1}$$

where $\mathbf{U}$ is the vector of the conserved variables and $\mathcal{H} = (\mathbf{F}, \mathbf{G}, \mathbf{H})$ is the flux tensor given by the flux vectors. The flux vectors consist of a viscous and an inviscid component, indicated by the superscripts i and v, so that $\mathbf{F} = \mathbf{F}^{\mathrm{i}} + \mathbf{F}^{\mathrm{v}}$, $\mathbf{G} = \mathbf{G}^{\mathrm{i}} + \mathbf{G}^{\mathrm{v}}$ and $\mathbf{H} = \mathbf{H}^{\mathrm{i}} + \mathbf{H}^{\mathrm{v}}$ [32, p. 3ff.]. In this form, the equations for inviscid flows (*Euler equations*) are given through equ. (3.1), simply by neglecting the viscous part of the flux vectors.

$$\mathbf{U} = \begin{pmatrix} \rho \\ \rho u \\ \rho v \\ \rho w \\ \rho E \end{pmatrix}, \quad \mathbf{F}^{\mathrm{i}} = \begin{pmatrix} \rho u \\ \rho u^2 + p \\ \rho uv \\ \rho uw \\ u(\rho E + p) \end{pmatrix}, \quad \mathbf{F}^{\mathrm{v}} = \begin{pmatrix} 0 \\ \tau_{xx} \\ \tau_{xy} \\ \tau_{xz} \\ u\tau_{xx} + v\tau_{xy} + w\tau_{xz} - q_1 \end{pmatrix},$$

$$\mathbf{G}^{\mathrm{i}} = \begin{pmatrix} \rho v \\ \rho uv \\ \rho v^2 + p \\ \rho vw \\ v(\rho E + p) \end{pmatrix}, \quad \mathbf{G}^{\mathrm{v}} = \begin{pmatrix} 0 \\ \tau_{yx} \\ \tau_{yy} \\ \tau_{yz} \\ u\tau_{yx} + v\tau_{yy} + w\tau_{yz} - q_2 \end{pmatrix},$$

$$\mathbf{H}^{\mathrm{i}} = \begin{pmatrix} \rho w \\ \rho uw \\ \rho vw \\ \rho w^2 + p \\ w(\rho E + p) \end{pmatrix}, \quad \mathbf{H}^{\mathrm{v}} = \begin{pmatrix} 0 \\ \tau_{zx} \\ \tau_{zy} \\ \tau_{zz} \\ u\tau_{zx} + v\tau_{zy} + w\tau_{zz} - q_3 \end{pmatrix}.$$

In the finite volume method, the region of interest is divided into non-overlapping control volumes. For each control volume, equ. (3.1) is solved. To do so, the average values of the conserved variables in $\mathbf{U}$ are expressed as [32, p. 545]:

$$\overline{\mathbf{U}}_V(t) = \frac{1}{|V|} \iiint_V \mathbf{U}(\mathbf{x}, t)\, \mathrm{d}V$$

The time rate of change of these averages is then given by the right-hand side of equ. (3.1) divided by the size of the control volume:

$$\frac{\mathrm{d}}{\mathrm{d}t}\overline{\mathbf{U}}_V(t) = -\frac{1}{|V|} \iint_S \mathcal{H} \cdot \mathbf{n}\, \mathrm{d}S \tag{3.2}$$

Now the left-hand side contains all the time derivatives and all the spatial derivatives are on the right-hand side. Equ. (3.2) is then discretised through an appropriate time stepping scheme.

For the discretisation in space, the integral on the right-hand side of equ. (3.2) is simplified to the sum over the individual straight segments S_i of the control volume, as depicted in fig. (3.1) [39]:

$$\begin{aligned} \iint_S \mathcal{H} \cdot \mathbf{n}\, \mathrm{d}S &= \sum_{i=1} \int_{S_i} \mathcal{H}\left(\mathbf{V}(\bar{\mathbf{x}})\right) \cdot \mathbf{n}_i\, \mathrm{d}S \\ &\approx \sum_{i=1} |S_i|\, \mathcal{H}\left(\mathbf{V}(\bar{\mathbf{x}}_i)\right) \cdot \mathbf{n}_i \end{aligned}$$

where $\mathbf{n}_i$ denotes the normal vector and $|S_i|$ the surface area of the corresponding segment. The flux variables at the centre of the control volume $\bar{\mathbf{x}}$ and the centre of the surface segment $\bar{\mathbf{x}}_i$ are described by $\mathbf{V}(\bar{\mathbf{x}})$ and $\mathbf{V}(\bar{\mathbf{x}}_i)$.

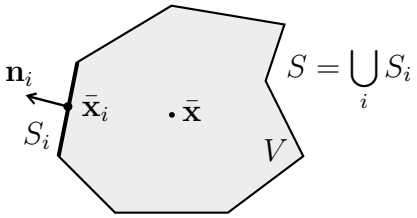

Figure 3.1.: Control volume V with surface segments S_i.

To obtain a second-order discretisation in space, the TAU-code uses a MUSCL (Monotone Upstream centred Schemes for Conservation Laws)[40] reconstruction of the variables at the control volume surface [39]:

$$\mathcal{H}(\mathbf{V}(\bar{\mathbf{x}}_i)) \approx \mathcal{H}\left(\mathbf{V}(\bar{\mathbf{x}}) + \left.\frac{\partial \mathbf{V}}{\partial \mathbf{x}}\right|_{\bar{\mathbf{x}}} \cdot (\bar{\mathbf{x}}_i - \bar{\mathbf{x}})\right)$$

3.2. Direct Simulation Monte Carlo

The DSMC method simulates gas flows on the molecular level, in contrast to other CFD approaches that model flows on a macroscopic scale. The DSMC method is based on a physical approach. Thus, instead of attempting to solve the Boltzmann equation, it directly models the physical processes in the gas based on probabilistic particle interactions. The gas is described by a large number of simulated particles, each representing a fixed amount of real molecules. The positions, velocities and internal states of all simulated particles are modified for each time step based on particle-surface interactions and intermolecular collisions. The macroscopic flow properties, such as velocity and temperature, are given by the cell-averages of the microscopic particle attributes within a grid cell.

The essential aspect of the DSMC method is that it uncouples molecular motion and intermolecular collisions. For each time step, the particles are first moved in space and may interact with the surface elements of the considered object. Subsequently, inter-particle collisions and chemical reactions are modelled but only particles within the same cell are able to interact with each other. To obtain solutions independent of the time step or grid spacing, the time step should be smaller than the mean

collision time and the grid should be resolved higher than the local mean free path. [28, Ch. 9-10] [37]
Due to the microscopic modelling, the computational expense of the DSMC method is quite high, especially towards the lower Knudsen number range. However, it provides results with great accuracy, as DSMC solutions are proven to agree with solutions of the Boltzmann equation for a monatomic gas [41].

The SPARTA-code is a DSMC-solver to simulate rarefied gases, using a Cartesian grid in two or three dimensions. It includes different collision, chemistry and boundary condition models [37, 38].

4. Implementation of Slip-Flow Boundary Conditions

This section describes the main concepts of implementing the slip-flow boundary conditions into the DLR TAU-code. The derivations in this section are based on the generalised slip conditions due to their compactness. Implementing the Maxwell conditions follows the same procedure, only the factor containing the accommodation coefficients has to be adjusted in the slip equations.

4.1. Existing Implementation

The old implementation [24] of the slip boundary conditions approximated the derivatives in equ. (2.11) through a difference quotient between the wall point and near point. *Wall points* (*wp*) refer to the grid points directly on the wall and their neighbouring grid points inside of the flow domain are referred to as *near points* (*np*). Every wall point possesses a clearly defined near point.

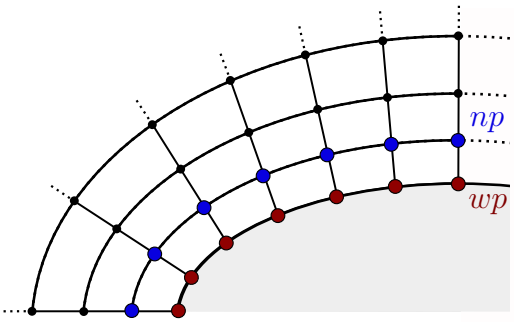

Figure 4.1.: Schematic depiction of a grid and the distribution of wall points (wp) in red and near points (np) in blue.

The velocity derivative in equ. (2.11) is then approximated as follows:

$$\frac{\partial u}{\partial n} = \frac{u_{\mathrm{np}} - u_{\mathrm{wp}}}{\Delta n}$$

where Δn describes the distance between the wall point and near point. The temperature derivative is approximated analogously. Inserting the difference quotients into equ. (2.11) and setting the wall point properties (u_{wp} and T_{wp}) equal to the slip

properties (u_s and T_s) yields an expression for the velocity and temperature slip:

$$u_\mathrm{s} = \frac{2\lambda}{2\lambda + \Delta n\sigma} \cdot u_\mathrm{np}$$

$$T_\mathrm{s} = \frac{2\lambda_T}{2\lambda_T + \Delta n\sigma} T_\mathrm{np} + \frac{\Delta n\sigma}{2\lambda_T + \Delta n\sigma} T_\mathrm{w}$$

4.2. Coordinate Transformation

In the new implementation, the existing gradient data structures in the TAU-code are used to compute the velocity and temperature slip. TAU calculates the velocity and temperature gradients in a Cartesian coordinate system (xyz-system) but the slip equations require the derivatives in the direction normal and tangential to the body's surface. Through a simple coordinate transformation, it is possible to express the gradients from the Cartesian xyz-system as gradients in a new orthonormal system with surface normal and tangential basis vectors.

4.2.1. Basis Vectors

The basis vectors of the new coordinate system have to be chosen in such a way, that they form a right-handed system. To do so, the outer normal vector of the surface is set as the first basis vector **n**. The second basis vector **m** is then calculated as proposed by Rhode [42]. Subsequently, both vectors are normalised and the third basis vector **l** is generated from the cross product of **n** and **m**. The cross product ensures that the system is right-handed and since **n** and **m** are orthogonal unit vectors, **l** does not require normalisation.

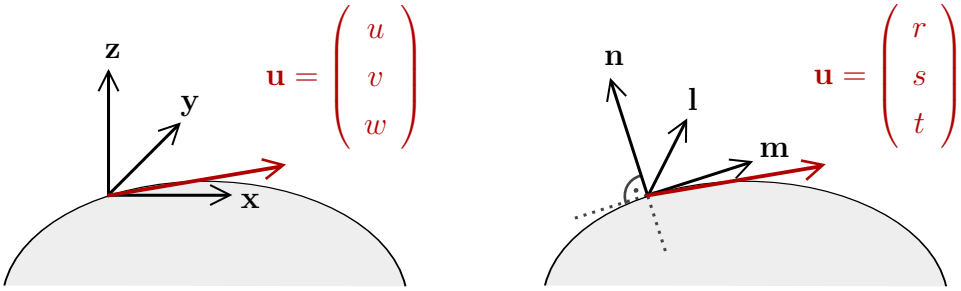

Figure 4.2.: Schematic depiction of the old coordinate system (xyz) on the left and the new coordinate system (nml) on the right.

Figure 4.2 depicts the standard Cartesian coordinate system, in which the basis vectors $\left\{\mathbf{x}, \mathbf{y}, \mathbf{z}\right\}$ are not necessarily aligned with the normal and tangential vectors of the surface. The new coordinate system, however, consists of one basis vector normal to the surface and two basis vectors tangential to the surface. The new coordinate system is generated for each grid point on the wall, to compute the normal and tangential derivatives over the whole surface.

In the following sections, the components of the velocity vector $\mathbf{u}$ in the xyz-system are referred to as u, v, w and the components in the new nml-system are referred to as r, s, t, as shown in fig. 4.2.

4.2.2. Transformation Matrix

In order to transform the gradients from one coordinate system into the other, the transformation matrix T, transforming the basis $\{\mathbf{x}, \mathbf{y}, \mathbf{z}\}$ into the new basis $\{\mathbf{n}, \mathbf{m}, \mathbf{l}\}$, is required. The row vectors of the matrix K are constructed from the new basis vectors with respect to the basis $\left\{\mathbf{x}, \mathbf{y}, \mathbf{z}\right\}$ [43, p. 45]:

$$K = \begin{pmatrix} n_x & n_y & n_z \\ m_x & m_y & m_z \\ l_x & l_y & l_z \end{pmatrix}$$

The indices indicate the x-,y- and z-components of each basis vector. Since the basis vectors form an orthonormal system, the transformation matrix is an orthogonal matrix and thus, its inverse is equal to its transpose [44, p. 155]. A given velocity vector $\mathbf{u}$ transforms from one system into the other as follows:

$$\begin{pmatrix} r \\ s \\ t \end{pmatrix} = K \cdot \begin{pmatrix} u \\ v \\ w \end{pmatrix} \qquad \text{and} \qquad \begin{pmatrix} u \\ v \\ w \end{pmatrix} = K^{-1} \cdot \begin{pmatrix} r \\ s \\ t \end{pmatrix} \tag{4.1}$$

For the transformed components, the gradients with respect to the $\{\mathbf{x}, \mathbf{y}, \mathbf{z}\}$ basis are calculated through:

$$\begin{aligned} \boldsymbol{\nabla} r = \boldsymbol{\nabla}(\mathbf{n} \cdot \mathbf{u}) &= \boldsymbol{\nabla}(n_x u + n_y v + n_z w) \\ &= n_x \boldsymbol{\nabla} u + n_y \boldsymbol{\nabla} v + n_z \boldsymbol{\nabla} w \end{aligned}$$

Introducing the gradient matrix, containing the velocity gradients $\boldsymbol{\nabla} u\,, \boldsymbol{\nabla} v$ and $\boldsymbol{\nabla} w$ as column vectors, leads to an expression for the gradients of the transformed velocities:

$$\begin{pmatrix} \partial_x r & \partial_x s & \partial_x t \\ \partial_y r & \partial_y s & \partial_y t \\ \partial_z r & \partial_z s & \partial_z t \end{pmatrix} = \begin{pmatrix} \partial_x u & \partial_x v & \partial_x w \\ \partial_y u & \partial_y v & \partial_y w \\ \partial_z u & \partial_z v & \partial_z w \end{pmatrix} \cdot K^{-1}$$

Applying the formula for directional derivatives [45] gives the gradients of the velocity components r, s and t with respect to the new basis $\{\mathbf{n}, \mathbf{m}, \mathbf{l}\}$:

$$\frac{\partial r}{\partial n} = \boldsymbol{\nabla} r \cdot \mathbf{n} \tag{4.2}$$

In matrix notation, this yields:

$$\begin{pmatrix} \partial_n r & \partial_n s & \partial_n t \\ \partial_m r & \partial_m s & \partial_m t \\ \partial_l r & \partial_l s & \partial_l t \end{pmatrix} = K \cdot \begin{pmatrix} \partial_x u & \partial_x v & \partial_x w \\ \partial_y u & \partial_y v & \partial_y w \\ \partial_z u & \partial_z v & \partial_z w \end{pmatrix} \cdot K^{-1} \tag{4.3}$$

Equ. (4.3) provides a relation between the normal and tangential derivatives of the transformed velocity components and the gradients in the Cartesian system.

4.2.3. Velocity and Temperature Slip

In the *nml*- system, the slip velocity $\mathbf{u}_\mathrm{s}$ is computed by inserting the derivative $\partial_n s$ into equ. (2.11):

$$\mathbf{u}_\mathrm{s} = \begin{pmatrix} r_\mathrm{s} \\ s_\mathrm{s} \\ t_\mathrm{s} \end{pmatrix} = \frac{2\lambda}{\sigma} \cdot \begin{pmatrix} 0 \\ \partial_n s \\ \partial_n t \end{pmatrix} \tag{4.4}$$

Subsequently, the slip velocity has to be transformed back into the Cartesian *xyz*-system via equ. (4.1) to conform with the TAU velocity data structures:

$$\mathbf{u}_\mathrm{s} = \begin{pmatrix} u_\mathrm{s} \\ v_\mathrm{s} \\ w_\mathrm{s} \end{pmatrix} = K^{-1} \cdot \begin{pmatrix} r_\mathrm{s} \\ s_\mathrm{s} \\ t_\mathrm{s} \end{pmatrix} = K^{-1} \cdot \left[\frac{2\lambda}{\sigma} \cdot \begin{pmatrix} 0 \\ \partial_n s \\ \partial_n t \end{pmatrix} \right]$$

The temperature is a scalar and is thus not affected by the coordinate transformation. To compute the derivative $\partial_n T$ normal to the wall, equ. (4.2) is applied:

$$\frac{\partial T}{\partial n} = \boldsymbol{\nabla} T \cdot \mathbf{n}$$

Inserting this expression into equ. (2.11) yields the following formulation for the slip temperature:

$$T_s = \frac{2\lambda_T}{\sigma} \cdot \boldsymbol{\nabla} T \cdot \mathbf{n} + T_\mathrm{w} \tag{4.5}$$

4.2.4. Implementation Test

To test this new formulation of the slip conditions using the existing gradients computed by TAU, we set up a simple flat plate case, as proposed by Gökçen [9]. When starting the simulation with free-stream conditions at all grid points, including the ones on the wall, the TAU-solver would terminate within the first iteration steps. The computed gradients were initially so large, that the velocity diverged and the temperature became negative.
One approach to solve this problem was to use the gradients of the near points, instead of using the gradients directly at the wall. However, a detailed examination revealed that the problem persists. Furthermore, attempts to find an appropriate relaxation scheme for the first time-steps were unsuccessful. If a suitable condition for the relaxation routine had been found, the TAU-solver would not be able to get out of the relaxation procedure and into the actual computation routine of the slip values.

The overall issue with this type of boundary condition is that within one time-step the flow variables are updated at all grid points except for the wall points. The velocity and temperature values at the wall points are set at the end of each time-step. In the next time-step, the gradients are then calculated with the old values at the wall, yielding wrong gradients at the wall and thus leading to wrong velocities and temperatures at the wall. A simplified scheme of the current implementation is displayed in fig. A.1.

4.3. Gradient Update

A new approach to set the velocity and temperature values at the wall is to calculate them after the initial gradient computation and then updating the gradients with the set values (fig. A.1). This method uses the Green-Gauss scheme to compute and update the gradients.

4.3.1. Green-Gauss Gradient Computation

The Green-Gauss method approximates the gradients in a control volume V based on the Green-Gauss theorem. For a scalar property a, the Gauss theorem states [44, p. 578f.]:

$$\iiint_V \boldsymbol{\nabla} a \, \mathrm{d}V = \oiint_{\partial V} a \, \mathrm{d}\mathbf{S} \quad \text{with} \quad \mathrm{d}\mathbf{S} = \mathbf{n} \cdot \mathrm{d}S \tag{4.6}$$

Here, $\mathrm{d}S$ describes the surface element, $\mathbf{n}$ the corresponding normal vector, pointing outwards of the control volume, and ∂V the surface of the control volume.

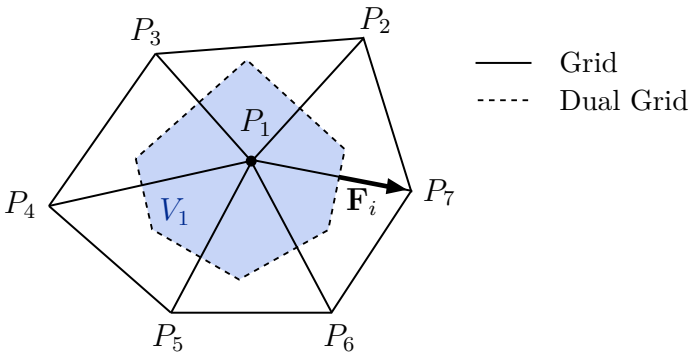

Figure 4.3.: Illustration of the control volume V_1 surrounding point P_1. Adapted from [48].

Let the control volume be a dual grid cell surrounding point P_1, as depicted in fig. 4.3. The gradients within a dual cell are assumed to be constant and equ. (4.6) then simplifies to [46]:

$$\boldsymbol{\nabla} a = \frac{1}{V_1} \iiint_{V_1} \boldsymbol{\nabla} a \, \mathrm{d}V = \frac{1}{V_1} \oiint_{\partial V_1} a\mathbf{n} \, \mathrm{d}S$$

with V_1 being the volume of the dual grid cell. The surface integrals are then

replaced by the sum over all straight surface segments (faces) F_i of the control volume, yielding the following discrete expression [47]:

$$\boldsymbol{\nabla} a = \frac{1}{V_1} \cdot \sum_{i=2}^{n} \frac{1}{2} \cdot (a_1 + a_i) \cdot \mathbf{F}_i \quad \text{with} \quad \mathbf{F}_i = \mathbf{n}_i \cdot |F_i| \tag{4.7}$$

where a_i denotes the value of a in point P_i and $\mathbf{n}_i$ describes the normal vector affiliated with the corresponding mesh face F_i. The area of the surface segments is described by $|F_i|$ and n is the number of grid points connecting to P_1.

4.3.2. Velocity and Temperature Slip

For the control volume V_{np} surrounding the near point, there is only one term in equ. (4.7) that contains the velocity at the wall. This term, containing the wall point velocity $u_{\text{wp,old}}$ from the previous time-step, is subtracted and then replaced by a term containing the new slip velocity u_{s} at the wall:

$$\begin{aligned} (\boldsymbol{\nabla} u)_{\text{np,new}} &= (\boldsymbol{\nabla} u)_{\text{np,old}} - \frac{u_{\text{np}} + u_{\text{wp,old}}}{2V_{\text{np}}} \cdot \mathbf{F}_{\text{wp}} + \frac{u_{\text{np}} + u_{\text{s}}}{2V_{\text{np}}} \cdot \mathbf{F}_{\text{wp}} \\ &= (\boldsymbol{\nabla} u)_{\text{np,old}} + \frac{u_{\text{s}} - u_{\text{wp,old}}}{2V_{\text{np}}} \cdot \mathbf{F}_{\text{wp}} \end{aligned} \tag{4.8}$$

where $\mathbf{F}_{\text{wp}}$ is the face normal vector pointing in the direction of the wall point, as defined in equ. (4.7). For simplicity, in the following steps the volume of the near point cell V_{np} will be denoted as V and the gradients will no longer be marked specifically as near point gradients.

Since equ. (4.7) is independent of the coordinate system, equ. (4.8) also holds for the gradients of the transformed velocity components r, s, t. The only condition here is that the face normal vector $\mathbf{F}_{\text{wp}}$ has to be expressed in the *nml*-system too. The slip velocity components are then calculated by inserting the new corrected gradient into equ. (4.4) and solving for s_{s}:

$$\begin{aligned} s_{\text{s}} &= \frac{2\lambda}{\sigma} \cdot \left(\frac{\partial s}{\partial n} \right)_{\text{new}} = \frac{2\lambda}{\sigma} \cdot \mathbf{n} \cdot (\boldsymbol{\nabla} s)_{\text{new}} \\ &= \underbrace{\frac{\lambda}{V\sigma - \lambda f}}_{=a} \cdot \Big(2V \cdot \mathbf{n} \cdot (\boldsymbol{\nabla} s)_{\text{old}} - f \cdot s_{\text{wp,old}} \Big) \end{aligned}$$

Here, f describes the scalar product of the basis vector $\mathbf{n}$ and the face normal vector $\mathbf{F}_{\mathrm{wp}}$. The other component t_{s} of the slip velocity is calculated analogously. Using equ. (4.2), the slip velocity is then given by:

$$\mathbf{u}_{\mathrm{s}} = \begin{pmatrix} r_{\mathrm{s}} \\ s_{\mathrm{s}} \\ t_{\mathrm{s}} \end{pmatrix} = a \cdot \left[2V \cdot \begin{pmatrix} 0 \\ (\partial_n s)_{\mathrm{old}} \\ (\partial_n t)_{\mathrm{old}} \end{pmatrix} - f \cdot \begin{pmatrix} 0 \\ s_{\mathrm{wp,old}} \\ t_{\mathrm{wp,old}} \end{pmatrix} \right] \tag{4.9}$$

Subsequently, the slip velocity vector has to be transformed back into the xyz-system via equ. (4.1). The slip temperature T_s is calculated analogously. The temperature gradient is corrected through equ. (4.7) and subsequently inserted into equ. (4.5):

$$\begin{aligned} T_s &= \frac{2\lambda_T}{\sigma} \cdot \mathbf{n} \cdot (\boldsymbol{\nabla} T)_{\mathrm{new}} + T_{\mathrm{w}} \\ &= \underbrace{\frac{\lambda_T}{V\sigma - \lambda_T f}}_{=b} \cdot (2V \cdot \mathbf{n} \cdot (\boldsymbol{\nabla} T)_{\mathrm{old}} - f \cdot T_{\mathrm{wp,old}}) + \frac{V\sigma}{V\sigma - \lambda_T f} \cdot T_{\mathrm{w}} \\ &= b \cdot \left[2V \cdot \left(\frac{\partial T}{\partial n} \right)_{\mathrm{old}} - f \cdot T_{\mathrm{wp,old}} \right] + (1 + f \cdot b) \cdot T_{\mathrm{w}} \end{aligned} \tag{4.10}$$

After the slip velocity and temperature at the wall have been set, the gradients are recomputed to provide the correct gradients for the remaining calculations in this iteration step (fig. A.1).

4.3.3. Additional Terms

For the additional terms, equ. (4.9) is extended by the curvature and thermal creep term introduced in sec. 2.3.3.
To do so, first the slip temperature is computed via equ. (4.10) and subsequently, the temperature gradient is updated using equ. (4.8). The slip velocity, extended with the curvature term, is then given by:

$$\mathbf{u}_{\mathrm{s}} = a \cdot \left[2V \cdot \begin{pmatrix} 0 \\ (\partial_n s)_{\mathrm{old}} \\ (\partial_n t)_{\mathrm{old}} \end{pmatrix} - f \cdot \begin{pmatrix} 0 \\ s_{\mathrm{wp,old}} \\ t_{\mathrm{wp,old}} \end{pmatrix} \right] + (1 + a \cdot f) \cdot \frac{3\mu}{4\rho T_{\mathrm{s}}} \cdot \begin{pmatrix} 0 \\ (\partial_m T)_{\mathrm{new}} \\ (\partial_l T)_{\mathrm{new}} \end{pmatrix}$$

For the additional curvature term, the tangential derivatives of the normal velocity component are required. However, setting the slip velocity changes only the tangen-

tial velocity components and thus, the gradient of the normal velocity component remains unchanged $(\boldsymbol{\nabla} r)_{\text{old}} = (\boldsymbol{\nabla} r)_{\text{new}}$. The curvature term is then incorporated as follows:

$$\mathbf{u}_{\text{s}} = a \cdot \left[2V \cdot \begin{pmatrix} 0 \\ (\partial_n s)_{\text{old}} \\ (\partial_n t)_{\text{old}} \end{pmatrix} + 2V \cdot \begin{pmatrix} 0 \\ \partial_m r \\ \partial_l r \end{pmatrix} - f \cdot \begin{pmatrix} 0 \\ s_{\text{wp,old}} \\ t_{\text{wp,old}} \end{pmatrix} \right]$$
$$+ (1 + a \cdot f) \cdot \frac{3\mu}{4\rho T_{\text{s}}} \cdot \begin{pmatrix} 0 \\ (\partial_m T)_{\text{new}} \\ (\partial_l T)_{\text{new}} \end{pmatrix}$$

5. Results and Discussion

In this chapter, the aerodynamic forces acting on the test objects are compared for the different slip boundary conditions based on the aerodynamic force coefficients. Given the drag D and the lift L, the force coefficients are computed as follows [1, p. 24]:

$$C_D = \frac{D}{\frac{1}{2}\rho_\infty U_\infty^2 \cdot A} \quad \text{and} \quad C_L = \frac{L}{\frac{1}{2}\rho_\infty U_\infty^2 \cdot A}$$

where ρ_∞ and U_∞ describe the free-stream density and velocity, and A denotes the reference area of the object. Furthermore, the local skin friction coefficient C_f, the pressure coefficient C_p and the heating coefficient C_h are given by [1, 2]:

$$C_f = \frac{\tau_\mathrm{w}}{\frac{1}{2}\rho_\infty U_\infty^2} \quad \text{and} \quad C_p = \frac{p - p_\infty}{\frac{1}{2}\rho_\infty U_\infty^2} \quad \text{and} \quad C_h = \frac{q}{\frac{1}{2}\rho_\infty U_\infty^3}$$

with the tangential shear stress at the wall τ_w.

In the following sections, the term "boundary conditions" refers to the different slip and no-slip boundary conditions applied at the wall and not to the different simulation conditions.

5.1. Test Case 1: Flat Plate

For the first test case, we simulated the two flat plate cases from Gökçen et al. [9] and Metcalf [26]. Gökçen's case [9] consists of a hot plate in a cold flow, that was modelled throughout the whole Knudsen number range. In contrast, Metcalf's case [18, 26] models a cold plate in a warm flow at a near-continuum Knudsen number. In both cases, the wall is isothermal and the test gas is nitrogen. Here, nitrogen is treated as an ideal gas in thermal equilibrium and the gas properties are displayed in table 5.1.

Table 5.1.: Gas constants and transport coefficients for nitrogen.

γ	R	S_c [K]	μ_{ref} [Pa s]	T_{ref} [K]	Pr
1.4	296.8	107	$1.663 \cdot 10^{-5}$	273	0.72

The simulation conditions of both cases are listed in table 5.2. For Gökçen's case, only the wall-to-stagnation temperature ratio of $T_w/T_0 = 0.7$ was known from the literature, so we set a fixed value for the free-stream temperature T_∞ and calculated the corresponding stagnation and wall temperature from there. Furthermore, to model the flat plate throughout the whole Knudsen number range, the plate length is held constant and the density is varied accordingly. Changes in the free-stream density also affect the free-stream pressure for each Knudsen number and thus, only the constant flow parameters are displayed in tab. 5.2.

Table 5.2.: Simulation conditions for the flat plate cases.

	p_∞ [Pa]	Ma_∞	U_∞ [m s^{-1}]	T_∞ [K]	T_w [K]	Gas	Kn
Gökçen case [9]	-	7	2358.3	273.15	2065.02	N_2	-
Metcalf case [26]	2.97	6.1	1129	83.4	77	N_2	0.004

5.1.1. Gökçen Case

We simulated this flat plate case to test the current implementation of the slip boundary conditions and in particular, the method for updating the gradients. Furthermore, we assessed whether treating the generalised slip condition as a boundary condition directly at the wall (sec. 2.3.2) still yields the same benefits as the original generalised slip condition [9].

5.1.1.1. Grid Independence Study

In order to compute the drag coefficient throughout the whole Knudsen number range, we generated various computational grids for the different Knudsen numbers. An example of the computational grids is depicted in fig. 5.1.
We performed a grid independence study based on the drag coefficient C_D for the different Knudsen numbers. Successive grids were generated by doubling the number of points normal to the wall and doubling the number of points along the plate. The

resolution parallel to the plate showed only minor effects on the drag coefficient. The number of points normal to the wall and the wall distance, describing the distance between the wall and the layer of grid points closest to the wall, are the dominating parameters. Fig. A.2 shows the drag coefficient in dependence of the normal resolution and wall distance for the no-slip condition at Re = 100. Similar studies were performed for Re = 10 and Re = 10000. The final grid was determined, if the drag coefficient changed by less than 1 % between consecutive grids and wall distances.

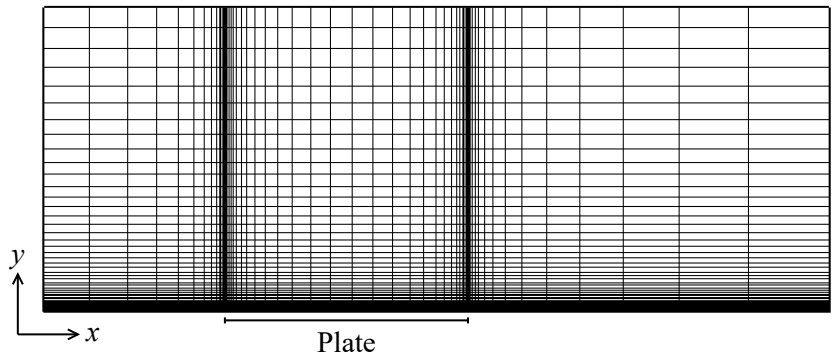

Figure 5.1.: Computational grid for the flat plate case at Re = 10000 and Kn = 0.001.

For the slip boundary conditions, we performed a more detailed grid independence study to ensure that the current implementation does not compromise the convergence order of the TAU-solver. Here, successive grids were generated by doubling the points in x- and y- direction and simultaneously halving the wall distance. The grid parameters and the corresponding drag coefficient for the generalised slip condition are displayed in tab. 5.3. For all grids, the drag coefficient differs by less than 1 % and the distributions of the local friction coefficient C_f agree closely with each other for the majority of the plate (fig. 5.2). The largest differences between the individual grids are observed at the leading and trailing edge of the plate. The same trends were observed for the Maxwell condition and Grid 3 was chosen as the final grid for this Reynolds number.

Table 5.3.: Grid parameters and drag coefficient for Re = 100 and Kn = 0.104.

	points in x	points in y	wall distance h [m]	drag C_D
Grid 1	17	17	$4 \cdot 10^{-4}$	0.1214
Grid 2	33	33	$2 \cdot 10^{-4}$	0.1219
Grid 3	65	65	$1 \cdot 10^{-4}$	0.1221

To determine the convergence order of the solver, the deviation ε from the finest grid (Grid 3) is calculated as follows:

$$\varepsilon = \frac{1}{N}\sum_{i=0}^{N}(C_{f,i} - C_{f,\text{fine},i})^2$$

where N is the number of grid points and $C_{f,i}$ the friction coefficient at the i-th grid point. The friction coefficient at the corresponding grid point of the finest grid is given by $C_{f,\text{fine},i}$. The order r_c of the method is then given by [49]:

$$\varepsilon = C \cdot h^{r_\text{c}}$$

with a constant C and the wall distance h. The ε-values for all grids are displayed fig. 5.2. For Grid 2, the deviation from the finest grid is one order of magnitude smaller compared to Grid 1. For the convergence order of the solver a value of $r_\text{c} = 2.72$ is obtained. The TAU-code is a method of approximately 2nd order and thus the addition of slip boundary conditions does not seem to compromise the order of the solver. However, the discussed convergence order is based only on two ε-values and thus gives merely a rough estimate of the actual order. A more systematic study, based on a larger sample size, could be performed in future studies to determine a more accurate value.

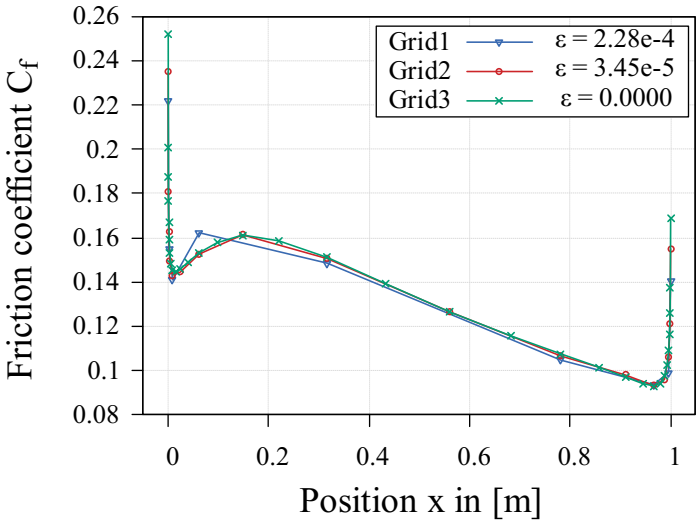

Figure 5.2.: Grid independence study based on the friction coefficient C_f for the generalised slip condition at Re = 100 and Kn = 0.104.

5.1.1.2. Drag Coefficient

To analyse whether the current implementation of the generalised slip condition still shows the benefits of the original condition, we attempted to reproduce the results from Gökçen et al. [9]. Fig. 5.3 shows Gökçen's results and the results from the current implementation for the drag coefficient C_D in dependence of the Reynolds and Knudsen numbers. The reference experiments [50] were performed for a flat plate fully immersed inside of a flow, creating drag on the top and bottom of the plate. In contrast, the TAU and DSMC results were computed for a flat plate that experiences a flow merely on one side and thus, the resulting drag coefficient is doubled in fig. 5.3. Since the exact free-stream and wall temperatures were not provided, we performed our own DSMC simulations[1] as a reference. The Knudsen number is calculated via [51]:

$$\mathrm{Kn} = \frac{\mathrm{Ma}}{\mathrm{Re}} \cdot \sqrt{\frac{\gamma\pi}{2}}$$

For the TAU solutions, the conventional no-slip condition shows increasingly high deviations from the DSMC data for Knudsen numbers larger than $\mathrm{Kn} = 0.001$. The Maxwell slip condition captures the plateau at large Knudsen numbers, as predicted by the DSMC solution. However, it still shows strong deviations from the DSMC data for $\mathrm{Kn} > 0.01$ and overestimates the free molecular limit. In contrast, the generalised slip condition agrees well with the DSMC data throughout the whole Knudsen number range and approaches the theoretical value in the free molecular limit. In the limit of small Knudsen numbers ($\mathrm{Kn} < 0.01$), the DSMC data and the results obtained with both slip boundary conditions converge towards the no-slip solution.

Comparing the TAU results to Gökçen's results, the overall trends observed for the different boundary conditions are the same. However, Gökçen's generalised slip results match the Maxwell results closely up to a Knudsen number of $\mathrm{Kn} > 0.1$ and then approach the free molecular limit. In contrast, the generalised slip TAU results agree with the Maxwell solution only at small Knudsen numbers and generally match the DSMC data better. The same behaviour is observed for Gökçen's results when the temperature jump condition is neglected and only velocity slip condition is applied.

[1] C. Hepp, personal communication

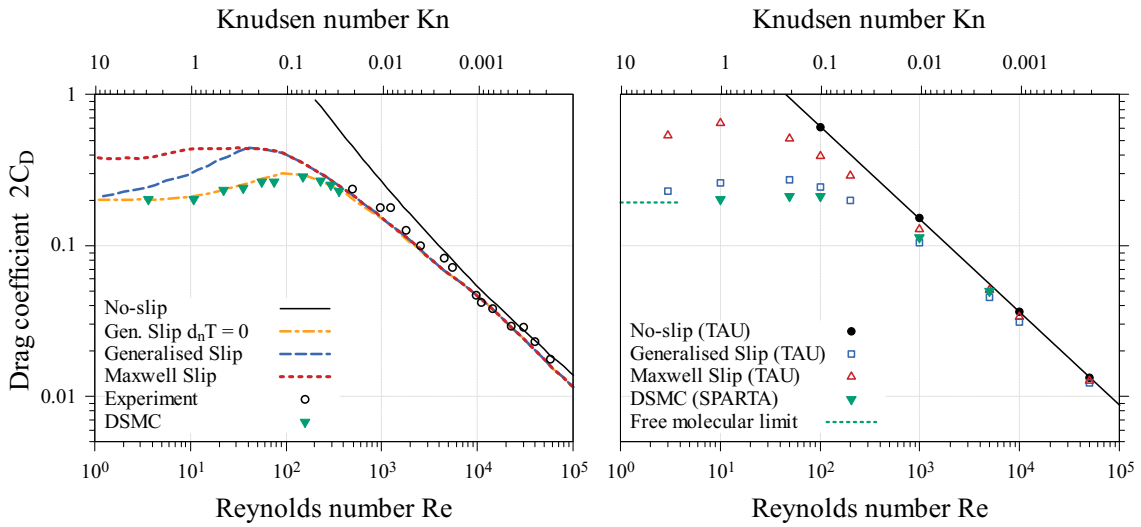

Figure 5.3.: Drag coefficient in dependence of the Reynolds and Knudsen numbers for the flat plate case. Results from Gökçen et al. [9] on the left and results from the TAU-code on the right. DSMC data from C. Hepp and free molecular limit from [52].

In general, a slight offset between the TAU results and Gökçen's results is observed for all boundary conditions as well as for the DSMC results. This offset is attributed to a possible difference in the choice of the wall and free-stream temperature. Furthermore, in Gökçen's study [9] the generalised slip condition refers to the combination of the generalised velocity slip and Maxwell's temperature jump condition. For the TAU results, the generalised velocity slip was combined with the generalised temperature jump condition. Overall, the current implementation reproduces Gökçen's results sufficiently well and does not compromise the effect of the generalised slip boundary condition. On the contrary, the agreement with DSMC data is improved by the current interpretation of the generalised slip condition compared to Gökçen's original condition. From here on, the generalised slip refers to the current implementation and no longer to the original boundary condition.

5.1.1.3. Surface Properties

In addition to the drag coefficient, we investigated the effect of the slip boundary conditions on the distribution of the skin friction coefficient C_f, the heat flux q and the pressure p along the plate (fig. 5.4).
The no-slip condition drastically overestimates the skin friction at the leading and trailing edge of the plate but matches the DSMC data well along the middle of the plate. Applying the Maxwell slip condition decreases the values at the edges of the

plate but the strong overestimation remains. Along the middle of the plate, however, the Maxwell solution agrees precisely with the DSMC solution. The generalised slip condition further reduces the skin friction values at the edges of the plate but slightly underestimates the friction for the majority of the plate. The drag coefficient C_D (tab. 5.4) is approximated best by the generalised slip condition, showing the smallest deviation ($\approx 5\,\%$) from the DSMC value. The no-slip condition deviates by approximately $40\,\%$ from the DSMC solution and the Maxwell solution by more than $15\,\%$ due to the overprediction of the skin friction at the edges of the plate.

Table 5.4.: Surface properties for Gökçen's flat plate case and the percentage deviation from DSMC data for the individual boundary conditions at Re = 1000 and Kn = 0.01.

Surf. Property (% dev.)	Drag C_D	Heat flow Q [W]	Lift C_L
DSMC	0.0550 (0.0 %)	368.8 (0.0 %)	−0.111 (0.0 %)
No-Slip	0.0769 (39.8 %)	401.3 (8.81 %)	−0.241 (117.1 %)
Maxwell	0.0641 (16.6 %)	422.8 (14.7 %)	−0.186 (67.6 %)
Gen. Slip	0.0521 (-5.3 %)	501.0 (35.9 %)	−0.136 (22.5 %)

Similar to the skin friction, the heat flux is overpredicted at the leading edge by all boundary conditions, where the generalised slip solution shows the least deviation from the DSMC value followed by the Maxwell solution. The no-slip and Maxwell solution then proceed to underestimate the heat flux for the majority of the plate, while the generalised slip condition gives good agreement with the DSMC data for $x > 0.2$. At the trailing edge, the generalised slip and Maxwell slip condition both eliminate the strong overestimation observed for the no-slip solution. Surprisingly, the integral heat flow Q (tab. 5.4) shows the least deviation from the DSMC value for the no-slip solution. The generalised slip solution shows the highest deviation ($\approx 35\,\%$), despite the good agreement with the DSMC solution for the local heat flux distribution. For the no-slip and Maxwell slip conditions, the overestimation of the local heat flux at the edges of the plate seems to compensate the underestimation along the middle of the plate. This leads to a better prediction of the integral heat flow than compared to the generalised slip condition.

Here, the heat flux q was calculated via equ. (2.14), taking the sliding friction due to the velocity slip into account. Using only Fourier's law to compute the heat flux results in a negative heat transfer (fig. A.3) due to the high wall temperature of the plate. Including the friction term in the heat flux computation yields a positive heat

transfer along the whole plate, as predicted by the DSMC solution. Extending the heat transfer with the sliding friction term is thus essential to correctly describe the physics at the wall.

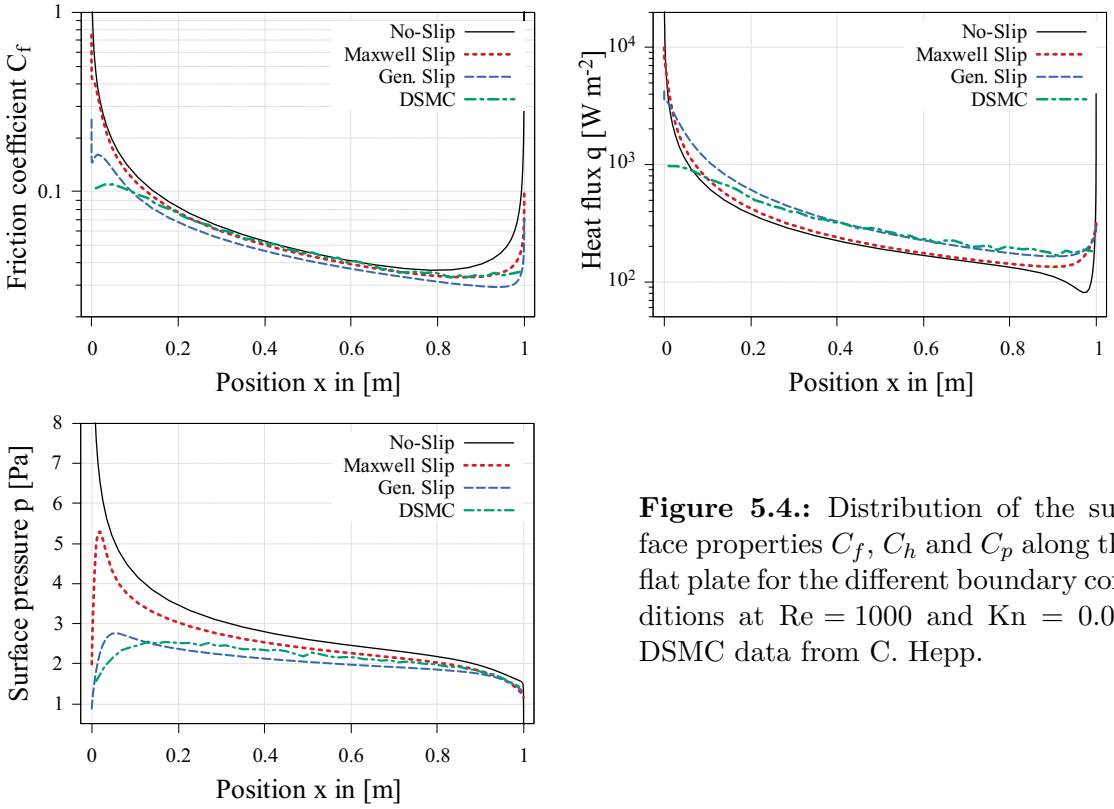

Figure 5.4.: Distribution of the surface properties C_f, C_h and C_p along the flat plate for the different boundary conditions at Re = 1000 and Kn = 0.01. DSMC data from C. Hepp.

For the surface pressure p, the generalised slip condition captures the course of the DSMC curve best and agrees well with the DSMC solution towards the trailing edge. The Maxwell solution shows the same trend but strongly overpredicts the pressure near the leading edge of the plate. Directly at the leading edge, the generalised slip solution slightly underestimates the DSMC data and the Maxwell solution shows the smallest deviation from the DSMC solution. The no-slip solution agrees the least with the DSMC data, strongly overestimating the pressure at the leading edge and underestimating it at the trailing edge. The same trend is reflected in the lift coefficient C_L (tab. 5.4) of the plate. The generalised slip condition shows the smallest deviation from the DSMC value, followed by the Maxwell slip condition. The no-slip condition overestimates the lift coefficient by more than 100 %.

Fig. 5.5 shows the slip temperature T_s and slip velocity U_s along the plate. Here, the no-slip solution marks the wall temperature, since a temperature jump does not

exist for this condition and the fluid is in thermal equilibrium with the wall. As expected from equ. (2.6), (2.8) and (2.11), the generalised slip condition computes a higher temperature jump ΔT and slip velocity U_s compared to the Maxwell slip condition. Thus, the generalised slip solution shows larger deviations from the no-slip solution than the Maxwell solution along the whole plate. Interestingly, the DSMC solution predicts a slip temperature T_s that is even higher than the wall temperature. This phenomenon appears to be a non-equilibrium effect, that is more prominent at higher Knudsen numbers and weaker towards the continuum limit.

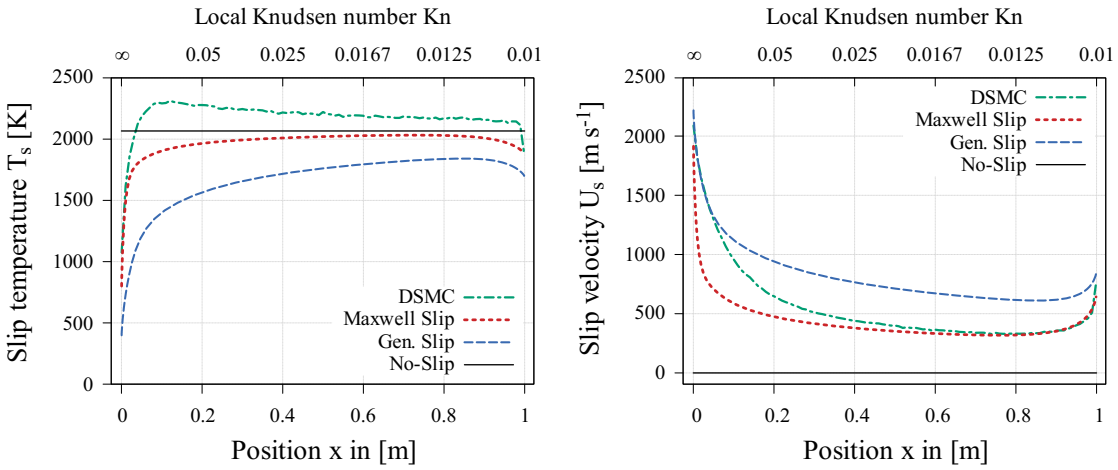

Figure 5.5.: Slip temperature T_s and slip velocity U_s along the plate at Re = 1000 and Kn = 0.01. DSMC data from C. Hepp.

Both slip boundary conditions capture the shape of the DSMC curves better compared to the no-slip condition. For the slip temperature, the Maxwell solution agrees well with DSMC data at the leading and trailing edge, while the generalised slip underestimates the slip temperature along the whole plate. For the majority of the plate, however, the no-slip solution is closest to the DSMC curve. For the slip velocity, the generalised slip curve agrees precisely with the DSMC solution at the leading edge but then proceeds to deviate significantly. From $x > 0.2$, the Maxwell slip predicts the slip velocity more precisely than the generalised slip and accurately matches the DSMC solution near the trailing edge.

Here, the effect of the local Knudsen number, calculated with the local position x on the plate instead of the plate length, can be observed clearly. At the leading edge, where the local Knudsen number is large, the generalised slip agrees better with the DSMC data compared to the Maxwell solution. In contrast, towards the trailing edge, where the local Knudsen number becomes smaller, the Maxwell solu-

tion matches the DSMC curve better. Furthermore, some correlation between the slip velocity and slip temperature can be observed here. The slip temperature is lowest when the slip velocity is at its highest, since there is less time to exchange heat with the wall compared to lower velocities. At the leading edge, the fluid decelerates quickly due to friction at the wall and accelerates again towards the trailing edge. As the slip velocity is decreasing, the slip temperature increases and vice versa.

5.1.1.4. Additional Terms

We analysed the influence of the additional terms, introduced in sec. 2.3.3, at a Reynolds number of Re = 100, since the differences between the individual boundary conditions become more prominent towards higher Knudsen numbers and lower Reynolds numbers. Fig. 5.6 shows the skin friction and heat flux distribution along the plate for the Maxwell slip condition.

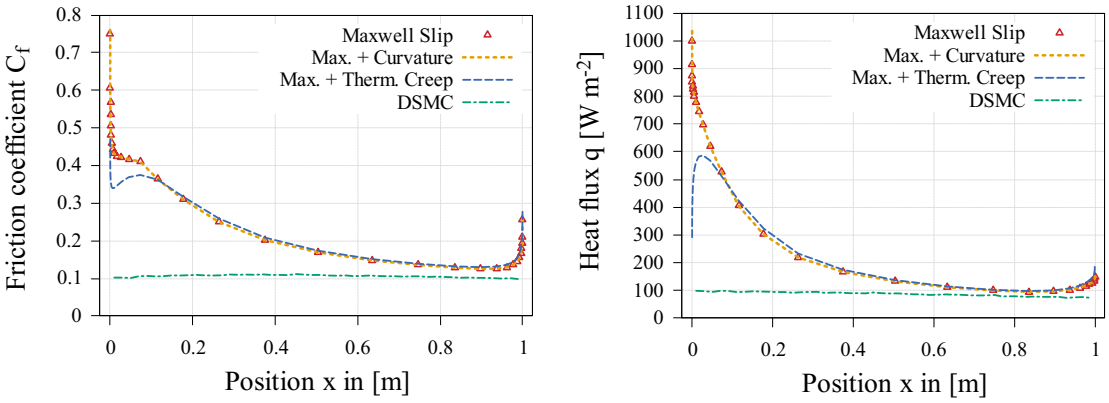

Figure 5.6.: Skin friction C_f and heat flux q along the plate for the Maxwell slip condition with and without the additional terms at Re = 100 and Kn = 0.104. DSMC data from C. Hepp.

As expected, extending the Maxwell slip condition with the curvature term does not affect the surface properties of the planar plate. The skin friction and heat flux distributions remain unchanged under the addition of the curvature term except for the peak values directly at the leading edge. The peak values are slightly increased compared to the simple Maxwell solution but the integral variables (tab. 5.5) remain unchanged. In contrast, the thermal creep term influences the skin friction and heat flux at the leading and trailing edge of the plate. The effects at the trailing edge, however, are minor compared to the effects at the leading edge, where the deviation

from the DSMC solution is decreased significantly. Along the middle of the plate, the solution for the Maxwell condition extended by the thermal creep term is in close agreement with the simple Maxwell solution. For the distribution of the surface pressure along the plate (fig. A.4), the same trend is observed. The impact of the thermal creep term on the integral drag and heat flow values is rather small. The deviations from the DSMC values are reduced by less than 2 % compared to the Maxwell solution. The deviation for the lift coefficient, however, is decreased by approximately 8 %. Including the additional terms in the generalised slip condition showed the same tendencies.
For the prediction of the integral variables, the thermal creep term may be neglected for isothermal walls. However, the changes in the local distributions of all three surface properties are relevant at high Knudsen numbers and generally not negligible.

Table 5.5.: Surface properties for Gökçen's flat plate case and the percentage deviation from DSMC data for the additional terms at Re = 100 and Kn = 0.104.

Surf. Property (% dev.)	Drag C_D	Heat flow Q [W]	Lift C_L
DSMC	0.1058 (0.0 %)	87.05 (0.0 %)	−0.1032 (0.0 %)
Maxwell	0.1972 (86.4 %)	206.82 (137.6 %)	−0.2374 (130.0 %)
Maxwell + Curv.	0.1972 (86.4 %)	206.82 (137.6 %)	−0.2374 (130.0 %)
Maxwell + Therm.	0.1955 (84.8 %)	205.70 (136.3 %)	−0.2294 (122.3 %)

5.1.2. Metcalf Case

To further test the current implementation, we simulated Metcalf's flat plate case [26] that models a less extreme temperature difference between the plate and the free-stream temperature. Here, no separate grid independence study was conducted. Instead, we used one of the grids generated for the small Knudsen number range of Gökçen's case [9]. As for the case discussed above, reference DSMC simulations were provided by C. Hepp[2].

5.1.2.1. Surface Properties

Fig. 5.7 shows the skin friction, heat flux and surface pressure along the plate. As in the previous section, the heat flux is calculated through equ. (2.14). Since this case

[2]Personal communication

models a Knudsen number that is closer to the continuum compared to the previous case, the differences between the different boundary conditions are generally less distinct here.

Overall, the results at the leading edge of the plate follow the same trend as in Gökçen's case. All boundary conditions overestimate the skin friction and heat flux directly at the leading edge, where the generalised slip shows the least deviation from the DSMC data and the no-slip shows the highest deviation. The skin friction computed with the generalised slip agrees precisely with the DSMC data for the majority of the plate and only deviates slightly at the edges. Along the middle of the plate, the no-slip and Maxwell slip solutions underestimate the skin friction slightly and overpredict it at the trailing edge. The drag coefficient C_D (tab. 5.6) shows the same tendency. The no-slip and Maxwell slip show rather high deviations ($\geqslant 8.0\,\%$) from the DSMC value, while the generalised slip solution deviates by less than $2\,\%$.

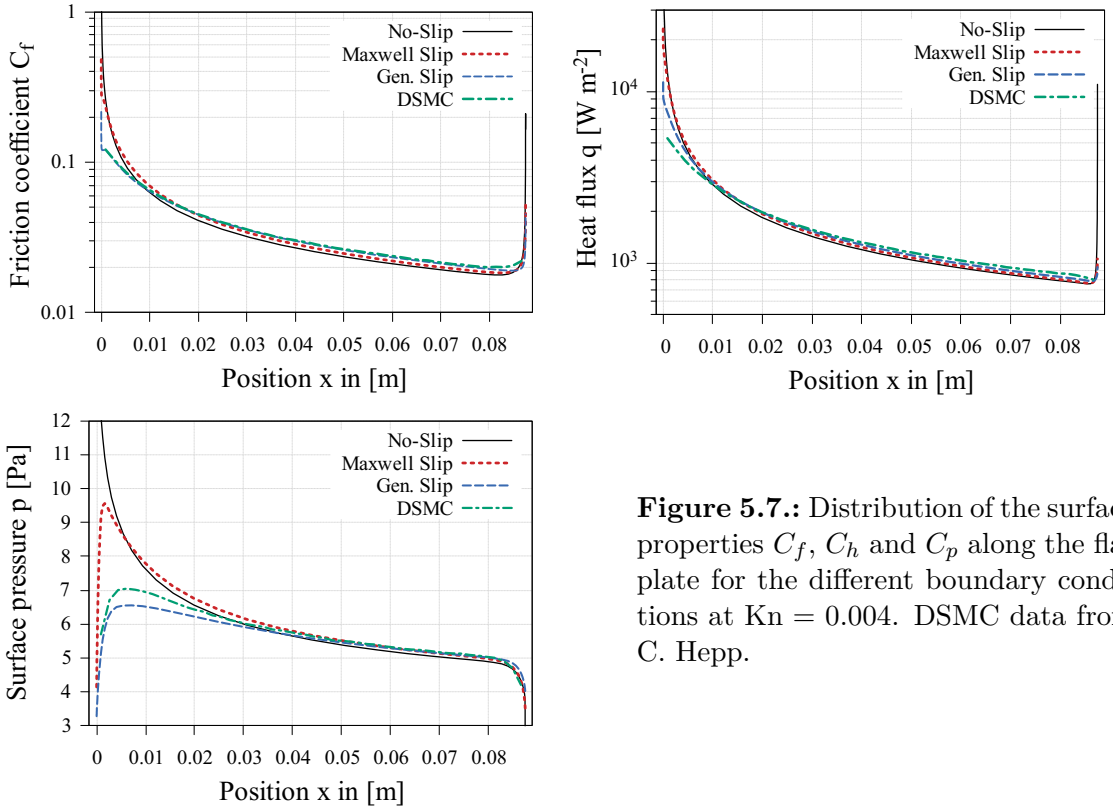

Figure 5.7.: Distribution of the surface properties C_f, C_h and C_p along the flat plate for the different boundary conditions at Kn = 0.004. DSMC data from C. Hepp.

The heat flux is overestimated at the edges of the plate with and without slip boundary conditions. However, the use of slip boundary conditions significantly decreases

the deviation from the DSMC solution at the trailing edge. For $x > 0.04$, all conditions slightly underestimate the heat flux but the generalised slip condition matches the DSMC curve best, followed by the Maxwell solution. Along the whole plate, the generalised slip solution shows the least deviation from the DSMC solution. For the integral heat flow (tab. 5.6), the same behaviour as for the drag coefficient is observed. However, for all conditions the deviations from the DSMC data are slightly higher for the heat flow compared to the drag coefficient.

The no-slip solution strongly overestimates the surface pressure near the leading edge and underestimates it for the rest of the plate. In contrast, the Maxwell slip underpredicts the pressure directly at the leading edge but then proceeds to overestimate it up to $x = 0.04$. The generalised slip underestimates the surface pressure for $x < 0.05$ but captures the general shape of the DSMC curve best. For $x > 0.05$, the Maxwell and generalised slip solution agree well with the DSMC data but slightly miscalculate the pressure at the trailing edge. The lift coefficient C_L (tab. 5.6) is predicted best by the Maxwell slip with a deviation from the DSMC value of 1 %. Surprisingly, the no-slip solution shows less deviation from the DSMC data than the generalised slip solution, which shows the highest deviation. For the no-slip condition, the strong overestimation of the surface pressure at the leading edge appears to compensate the underestimation at the trailing edge almost completely, leading to a rather precise prediction of the lift coefficient.

Table 5.6.: Surface properties for Metcalf's flat plate case and the percentage deviation from DSMC data for the different boundary conditions at Kn = 0.004.

Surf. Property (% dev.)	Drag C_D	Heat flow Q [W]	Lift C_L [10^{-2}]
DSMC	0.0375 (0.0 %)	143.7 (0.0 %)	−7.541 (0.0 %)
No-Slip	0.0414 (10.4 %)	166.2 (15.7 %)	−8.052 (6.8 %)
Maxwell	0.0405 (8.0 %)	160.1 (11.4 %)	−7.618 (1.0 %)
Gen. Slip	0.0369 (-1.6 %)	149.8 (4.2 %)	−6.476 (-14.1 %)

Fig. 5.8 shows the slip temperature and slip velocity at the wall. As observed in the previous case, the temperature jump ΔT computed with the generalised slip condition is larger compared to the Maxwell slip for most of the plate. Furthermore, the generalised slip predicts a higher slip velocity along the whole plate, which is consistent with the findings in Gökçen's case.

For the slip temperature, both boundary conditions fail to predict the peak near the leading edge. The Maxwell slip shows a maximum close to the leading edge but still significantly underestimates the DSMC value. In contrast, the generalised slip solution has no distinct peak and the position of the maximum is shifted slightly towards the middle of the plate. In general, the generalised slip solution fails to capture the shape of the DSMC curve and shows quite strong deviations from the DSMC solution along the whole plate. The Maxwell slip solution, in contrast, matches the DSMC curve accurately for $x > 0.03$.

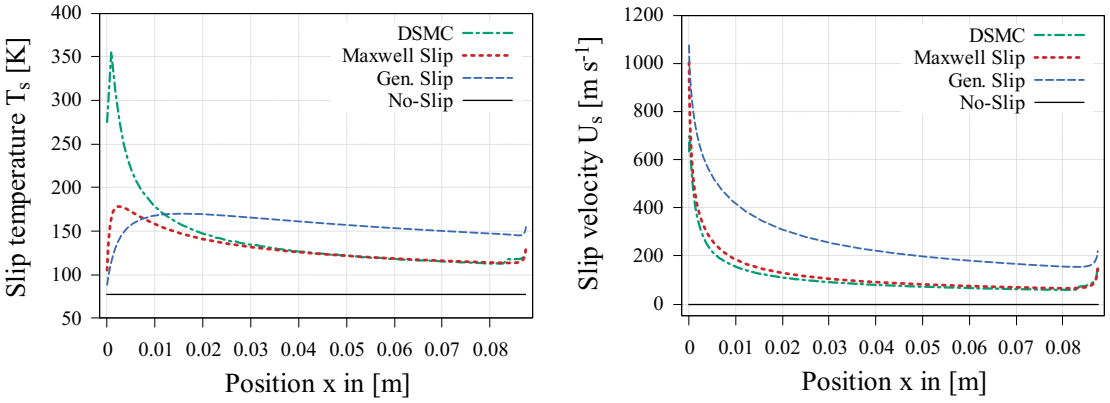

Figure 5.8.: Slip temperature T_s and slip velocity U_s along the plate at Kn = 0.004. DSMC data from C. Hepp.

The slip velocity directly at the leading edge is overestimated by both slip conditions but the Maxwell solution agrees closely with the DSMC curve for the rest of the plate. The generalised slip solution also captures the shape of the DSMC curve well but shows a rather strong offset to the DSMC data for the entire plate. Towards the trailing edge, the no-slip solution shows less deviation from the DSMC data compared to the generalised slip but fails to provide any information on the actual velocity distribution along the plate.

In this case, the plate has a cooling effect on the fluid due to the high free-stream temperature and low wall temperature. Here, the opposite relation between the slip velocity and slip temperature is observed. When the slip velocity is high there is less time for heat exchange between the fluid and the wall, leading to a higher slip temperature than compared to lower velocities. The DSMC solution clearly shows this relation but it cannot be observed for the slip solutions.

5.1.3. Discussion

Comparing the two flat plate cases, the same trends regarding the local surface properties are observed. Here, the use of slip boundary conditions clearly improves the agreement with the DSMC data compared to the no-slip condition. For both cases, the effects of the slip boundary conditions are strongest at the leading and trailing edge of the plate, where the no-slip solution shows a strong over- or underestimation of the surface properties. Furthermore, applying slip boundary conditions leads to a clear reduction in the deviation from the DSMC data for the drag coefficient, whereas no general trend is observed for the integral heat flow and lift coefficient. However, Gökçen's case models a rather extreme wall-to-free-stream temperature ratio and the choice of a particularly high wall temperature might influence the accuracy of the heat flow predictions. In contrast, Metcalf's case appears to model a more realistic scenario, where an improved agreement with the DSMC value for the heat flow is observed for both slip conditions.

5.2. Test Case 2: Cylinder

As a second test case, we simulated Lofthouse's cylinder case [2] to test our implementation on a more complex configuration. Furthermore, we investigated the influence of the additional terms on a non-planar geometry. For this case, Lofthouse's dissertation [2] provides reference DSMC data and reference solutions for the Maxwell slip and generalised slip conditions.

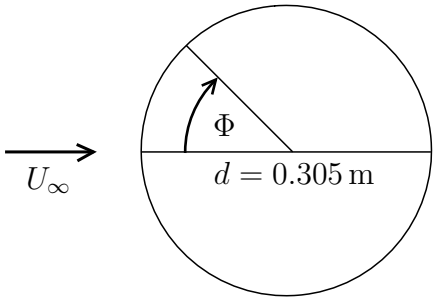

Figure 5.9.: Cylinder case with the cylinder angle Φ. Adapted from [2].

The test case models a two-dimensional 12-inch diameter cylinder (fig. 5.9) in a Mach-10 flow of argon. Argon is a monatomic gas without internal energy modes and thus no thermal non-equilibrium is possible in this case. The gas properties of argon are displayed in tab. 5.7. In his dissertation, Lofthouse simulated this case at

four different Knudsen numbers, ranging from the continuum to the free molecular regime. We chose to simulate this case for the Knudsen numbers of Kn = 0.05 and Kn = 0.25 because the strongest differences between the individual slip boundary conditions were observed at these Knudsen numbers. Here, the Knudsen number is calculated based on the cylinder diameter.

Table 5.7.: Gas constants and transport coefficients for argon.

γ	R	S_c [K]	μ_{ref} [Pa s]	T_{ref} [K]	Pr
1.667	208	144	$2.125 \cdot 10^{-5}$	273	0.667

The wall of the cylinder is treated as an isothermal wall with a wall temperature of $T_w = 500\,\mathrm{K}$ and the cylinder diameter is held constant. Similar to the plate, the different Knudsen numbers are simulated by changing the free-stream density. The simulation conditions for both Knudsen numbers are displayed in tab. 5.8.

Table 5.8.: Simulation conditions for the cylinder case.

Kn	ρ_∞ [kg/m^3]	Ma_∞	U_∞ [m s^{-1}]	T_∞ [K]	T_w [K]	Gas
0.05	$5.636 \cdot 10^{-6}$	10	2624	200	500	Ar
0.25	$1.127 \cdot 10^{-6}$	10	2624	200	500	Ar

Furthermore, we confirmed the accuracy of Lofthouse's DSMC solutions for the case of Kn = 0.25 with our own DSMC calculations[3]. The results are displayed in fig. A.5 in the appendix.

5.2.1. Grid Independence Study

A detailed grid independence study was conducted based on the local friction, pressure and heating coefficient distributions along the cylinder surface. The results shown in this section were obtained for the generalised slip condition at a Knudsen number of Kn = 0.25. For the no-slip condition and the Kn = 0.05 case, similar studies were performed.
Successive grids were generated by doubling the number of points parallel or normal to the wall. If the resolution normal to the wall is doubled, the wall distance is

[3]F. Ziese and C. Hepp, personal communication

divided in half. Here, the wall distance describes the distance between the layer of grid points closest to the wall and the wall itself. The grid parameters for the individual grids are given in tab. 5.9 and a section of the computational grid is displayed in fig. 5.10.

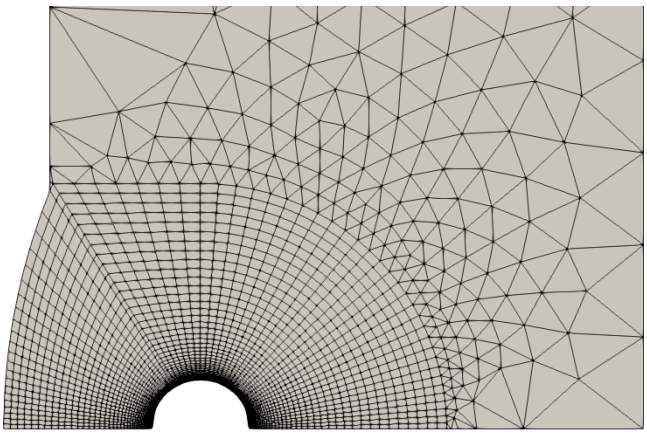

Figure 5.10.: Section of the computational grid for the cylinder case for Kn = 0.25.

Table 5.9.: Grid parameters for the Kn = 0.25 case. 1 grid unit = 0.1524 m.

	points parallel	points normal	wall distance [grid units]
Grid 1	60	60	$5 \cdot 10^{-3}$
Grid 2	120	60	$5 \cdot 10^{-3}$
Grid 3	120	120	$2.5 \cdot 10^{-3}$
Grid 4	60	60	$2.5 \cdot 10^{-3}$
Grid 5	60	60	$1 \cdot 10^{-3}$

Fig. 5.11 shows the skin friction distribution along the cylinder surface for the different computational grids. In general, all curves agree closely with each other but some minor differences can be identified in the magnified view in fig. 5.11. Compared to the solution of Grid 1, the solution obtained with Grid 2 is resolved better along the surface but the maximum friction value remains unchanged. The same tendency is observed when comparing Grid 3 and 4, indicating that the impact of the resolution parallel to the wall on the overall skin friction distribution is negligible. Furthermore, Grid 3 shows a reduction in the maximum of the skin friction distribution compared to Grid 1 and 2. However, comparing Grid 3 and Grid 4, it becomes clear that the change in the maximum skin friction is mainly due to the

change in the wall distance and not due to a higher resolution. Since the curves of Grid 3 and 4 agree well with each other except for changes in the parallel resolution, the resolution normal to the wall appears to have only a minor effect on the skin friction distribution. Thus, the dominating grid parameter is the wall distance, which is also observed for the heating and pressure coefficient (fig. A.6 and A.7).

Comparing the solutions of Grid 1, 4 and 5, a clear trend towards a lower skin friction maximum is observed. A similar behaviour is observed for the pressure coefficient, whereas the heating coefficient appears to be less sensitive to changes in the wall distance. The maximum skin friction, pressure and peak heating values computed with Grid 5 deviate by less than 1 % from the solution obtained with Grid 4 and thus, Grid 5 was determined as the final grid.

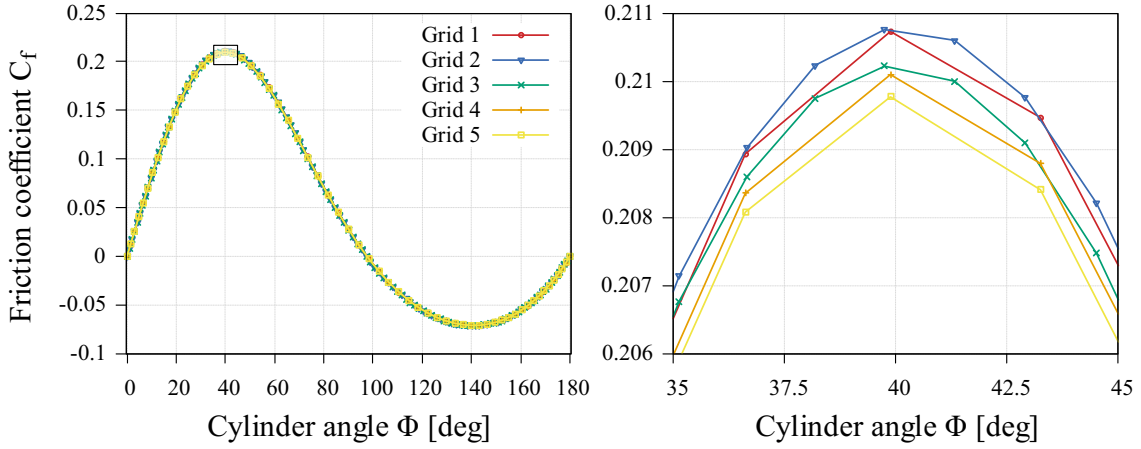

Figure 5.11.: Grid independence study for the generalised slip condition based on the friction coefficient C_f, plotted along the cylinder surface at Kn = 0.25. The box in the left plot marks the magnified area displayed on the right.

5.2.2. Surface Properties

Fig. 5.12 shows the skin friction coefficient C_f along the cylinder surface for both Knudsen numbers. On the left, the Maxwell slip condition was extended by the additional terms from sec. 2.3.3 and compared to the no-slip solution and reference data from Lofthouse [2]. The Maxwell condition was extended by the curvature term alone and by both, the curvature and the thermal creep term. On the right, the same was done for the generalised slip condition. However, due to the rather bad performance of the generalised slip condition at predicting the skin friction and

heating coefficient, we chose to not extend this condition with both additional terms but only with the curvature term.

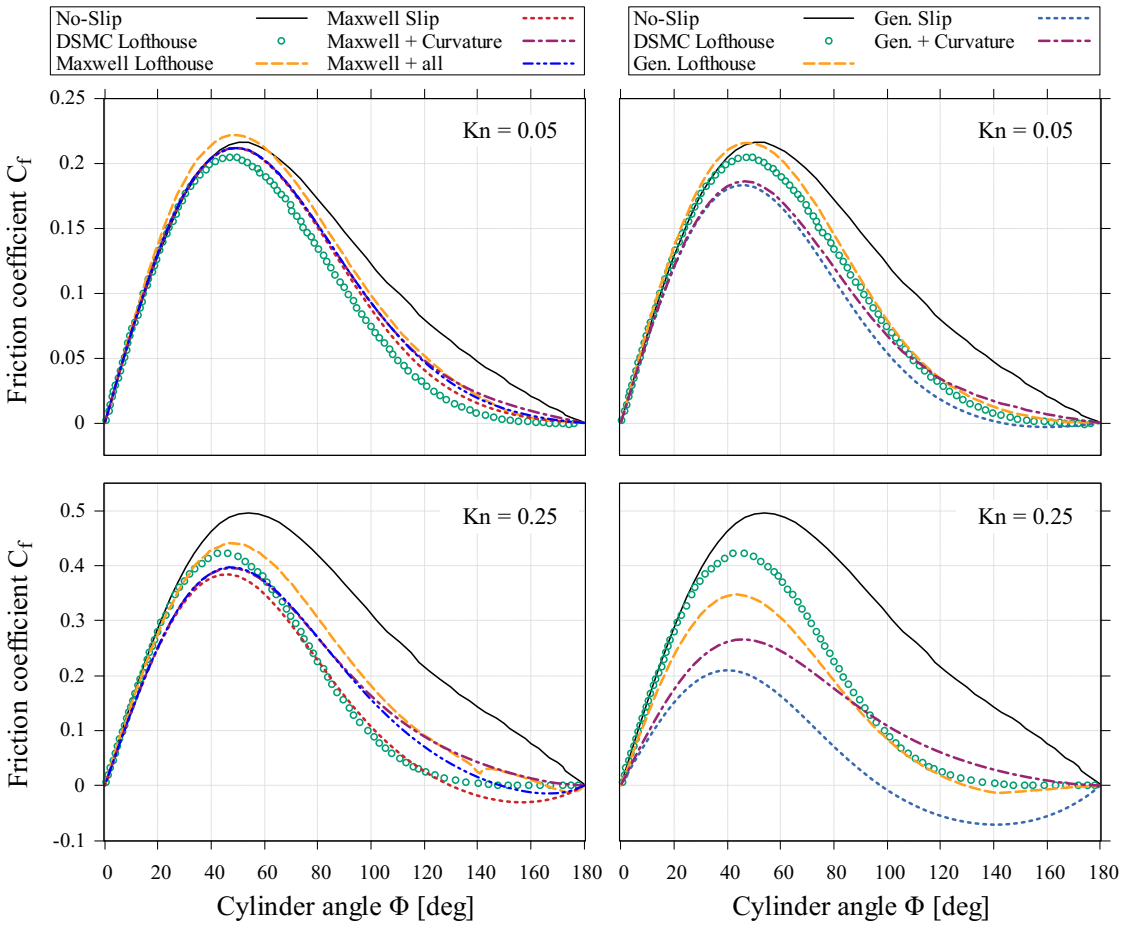

Figure 5.12.: Friction coefficient C_f along the cylinder surface at Kn = 0.05 and Kn = 0.25. The Maxwell slip conditions are displayed on the left and the generalised slip conditions on the right. Reference Lofthouse data from [2].

For Kn = 0.05, the different Maxwell slip solutions and the no-slip solution agree accurately with the DSMC data up to an angle of 40°. The no-slip solution then proceeds to overestimate the skin friction for the rest of the cylinder and the position of the maximum is shifted to the right, compared to the DSMC data. All of the Maxwell conditions show a clear decrease in the overestimation of the skin friction but a slight shift of the position of the maximum remains. The Lofthouse solution obtained with the Maxwell slip accurately predicts the position of the maximum skin friction but starts to deviate from the DSMC solution already at an angle of 20°. Additionally, the maximum friction is overestimated even stronger than compared to the no-slip solution. The additional terms only affect the skin friction for

$\Phi > 90°$ and slightly increase the deviation from the DSMC curve compared to the simple Maxwell solution. The thermal creep term only impacts the skin friction for $\Phi > 120°$ and the changes compared to the other Maxwell solutions are minor. In general, the simple Maxwell solution obtained with the current implementation matches the DSMC data best for this case.
The generalised slip condition, in contrast, begins to deviate from the DSMC data at an angle of 20° and generally underestimates the skin friction. However, the position of the maximum is predicted better by the generalised slip solutions than compared to the Maxwell solutions. Lofthouse's generalised slip solution agrees closely with the DSMC solution for the majority of the cylinder surface and only slightly overestimates the maximum friction. Here, including the curvature term in the generalised slip condition shows a larger effect compared to the Maxwell condition and improves the agreement with DSMC data for most of the cylinder.

For $\mathrm{Kn} = 0.25$, similar trends are observed. The no-slip solution matches the DSMC data up to an angle of 25° and then shows strong deviations towards the leeward side of the cylinder. The Maxwell slip solutions tend to deviate from the DSMC solution for $\Phi > 20°$ and, in this case, underestimate the maximum skin friction. The simple Maxwell solution agrees precisely with the DSMC curve for $70° < \Phi < 120°$ but then predicts negative skin friction values. The Lofthouse solution obtained with the Maxwell slip matches the DSMC data well up to the position of the maximum and then overestimates the friction for the rest of the cylinder. Here, the additional terms impact the friction already at an angle of $\Phi \approx 40°$ and slightly improve the agreement with the DSMC solution at the maximum of the curve. The curvature term eliminates the negative values observed for the simple Maxwell slip solution but overestimates the friction for $\Phi > 70°$. Adding the curvature and thermal creep term simultaneously slightly decreases the overprediction observed for the curvature term but also reintroduces negative values at the leeward side of the cylinder.
The generalised slip solution only agrees with the DSMC data at the stagnation points but strongly underestimates the friction for the whole cylinder. The Lofthouse generalised slip solution captures the course of the DSMC curve well but underpredicts the maximum skin friction rather strongly. Again, adding the curvature term eliminates the negative friction values and, in this case, it slightly improves the agreement with the DSMC data for the whole cylinder.

For the conventional no-slip condition, negative skin friction values indicate a recirculation in the flow field. For zero velocity at the wall, the velocity gradient in the tangential shear stress can only change from positive to negative values if the direction of the flow is reversed. For slip boundary conditions, however, the slip velocity at the wall allows negative skin friction values without the occurrence of recirculation. By allowing a non-zero velocity at the wall, the velocity gradients can be inverted without reversing the flow. As seen in fig. A.9, this is the case at the leeward side of the cylinder for the Kn = 0.25 case. Since the negative values are only observed for the high Knudsen number case, this phenomenon appears to be a rarefaction effect.

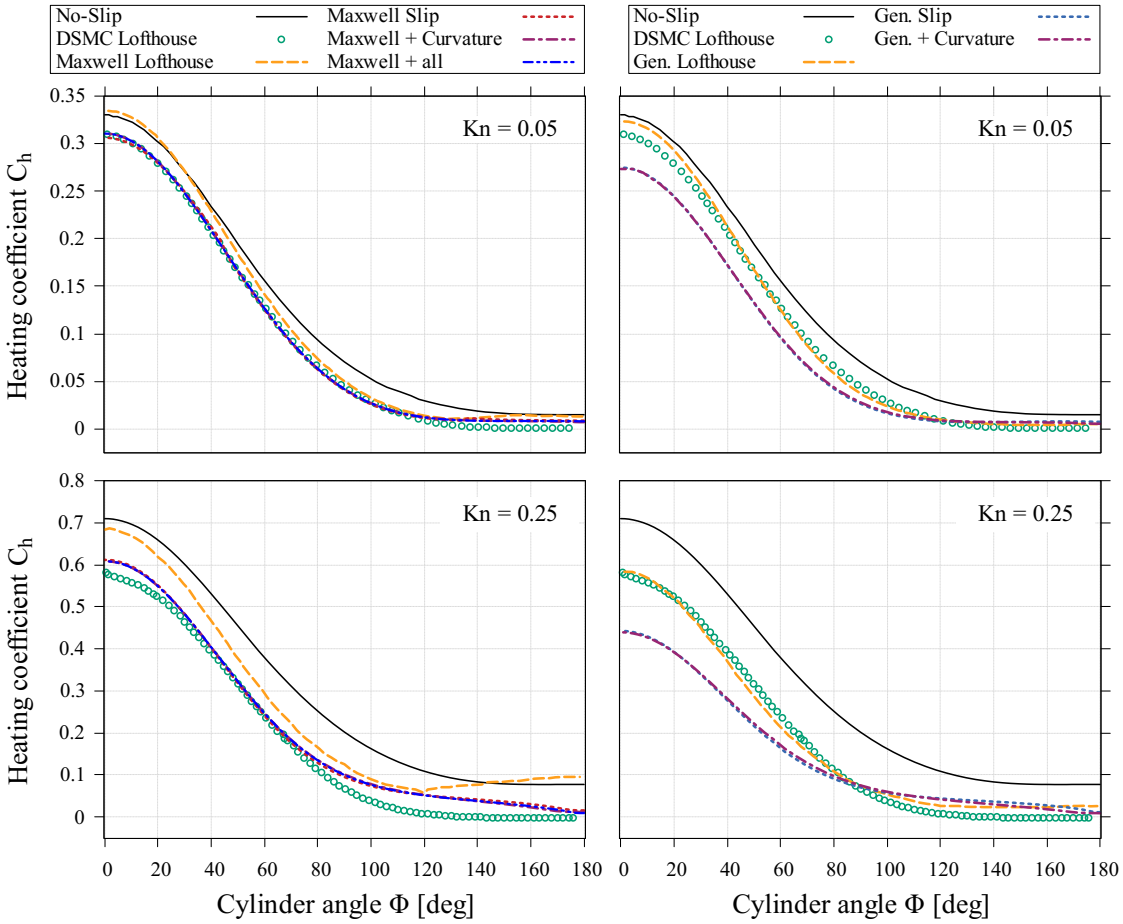

Figure 5.13.: Heating coefficient C_h along the cylinder surface at Kn = 0.05 and Kn = 0.25. The Maxwell slip conditions are displayed on the left and the generalised slip conditions on the right. Reference Lofthouse data from [2].

Fig. 5.13 shows the heating coefficient along the cylinder surface for the different boundary conditions. Here, Fourier's law was used to compute the heat transfer at

the wall without the sliding friction terms. Adding the sliding friction term used in the flat plate cases (equ. (2.14)) caused jumps in the distribution of heating coefficient along the cylinder surface. Furthermore, using the corrected shear stress for non-planar walls for the sliding friction term (equ. (2.15)) also did not eliminate these jumps. As seen in fig. A.8, the heating coefficient computed with only Fourier's law captured the smooth shape of the DSMC curve best and is also consistent with Lofthouse's heat flux evaluation.
For both Knudsen numbers, the no-slip solution systematically overestimates the heating coefficient, where the deviation from the DSMC data is strongest for the $\mathrm{Kn} = 0.25$ case. Moreover, the additional terms do not significantly impact the heating coefficient for both slip boundary conditions, independently of the Knudsen number. At $\mathrm{Kn} = 0.05$, the additional terms combined with the Maxwell slip show some minor changes at the stagnation point of the cylinder compared to the simple Maxwell solution. At $\mathrm{Kn} = 0.25$, the additional terms slightly decrease the heating coefficient at the leeward side of the cylinder for both slip conditions but the overall changes are negligibly small compared to the differences between the remaining boundary conditions.

For $\mathrm{Kn} = 0.05$, the Maxwell slip solutions agree accurately with the DSMC data for the majority of the cylinder surface and only show a slight deviation from the DSMC curve for $\Phi > 120°$. The Lofthouse solution obtained with the Maxwell condition overestimates the peak heating and, compared to the no-slip solution, shows an improved prediction of the heating coefficient for only a fraction of the cylinder surface. In contrast, the generalised slip solutions underestimate the peak heating by more than 10 % and match the DSMC data only towards the stagnation point at the leeward side of the cylinder. The Lofthouse generalised slip solution slightly overpredicts the peak heating but agrees precisely with the DSMC curve for the majority of the cylinder surface.
For $\mathrm{Kn} = 0.25$, the same trends are observed. The Maxwell slip conditions slightly overestimate the peak heating and tend to overpredict the heating coefficient for $\Phi > 80°$. In between, the Maxwell slip solution agrees precisely with the DSMC curve and shows the best agreement with the DSMC data compared to Lofthouse's Maxwell solution and the no-slip solution. Compared to the $\mathrm{Kn} = 0.05$ case, a stronger underprediction of the peak heating is observed for the generalised slip solutions and the overall deviation from the DSMC data is increased. The Lofthouse

generalised slip solution, however, continues to agree precisely with the DSMC curve for the majority of the plate.

The peak heating at Kn = 0.05 is summarised in tab. 5.10 for all boundary conditions. The largest deviation from the DSMC data is observed for the generalised slip solutions, followed by Lofthouse's Maxwell slip solution and the no-slip solution. The best prediction is achieved with the Maxwell slip condition extended with the curvature term, showing a deviation from the DSMC value of only 0.4 %. However, the simple Maxwell solution without the curvature term only shows a slightly higher deviation. Furthermore, the thermal creep term does not seem to impact the peak heating.
The results for the Kn = 0.25 case are displayed in tab. A.1. Here, the same tendency is observed, except that the best agreement with the DSMC value is observed for Lofthouse's generalised slip solution. For the current implementation, however, the Maxwell slip combined with the curvature term shows the least deviation from the DSMC solution (4.5 %). As seen in the Kn = 0.05 case, including the curvature term only slightly decreases the deviation from the DSMC value compared to the simple Maxwell solution. Again, the thermal creep term does not affect the peak heating.

Fig. 5.14 shows the distribution of the pressure coefficient C_p along the cylinder surface. Here, similar tendencies as for the heating coefficient are observed. The additional terms show no significant impact on the pressure coefficient for both slip boundary conditions and for both Knudsen number cases.
For Kn = 0.05, all boundary conditions agree closely with the DSMC data along the whole cylinder. The use of slip boundary conditions leads to a slight overprediction of the pressure coefficient at the leeward side of the cylinder, where the generalised slip condition shows the highest deviation from the DSMC curve. At Kn = 0.25, the no-slip and Lofthouse solutions overestimate the pressure at the stagnation point on the windward side, whereas the Maxwell and generalised slip conditions show good agreement with the DSMC data at this position. For $\Phi > 70°$, all slip conditions tend to overestimate the pressure coefficient but the smallest deviation from the DSMC curve is observed for the Lofthouse slip solutions. As observed before, the generalised slip condition shows the strongest deviation from the DSMC solution, closely followed by the Maxwell slip condition. Surprisingly, the no-slip condition

agrees best with the DSMC curve at the leeward side of the cylinder for both Knudsen number cases.

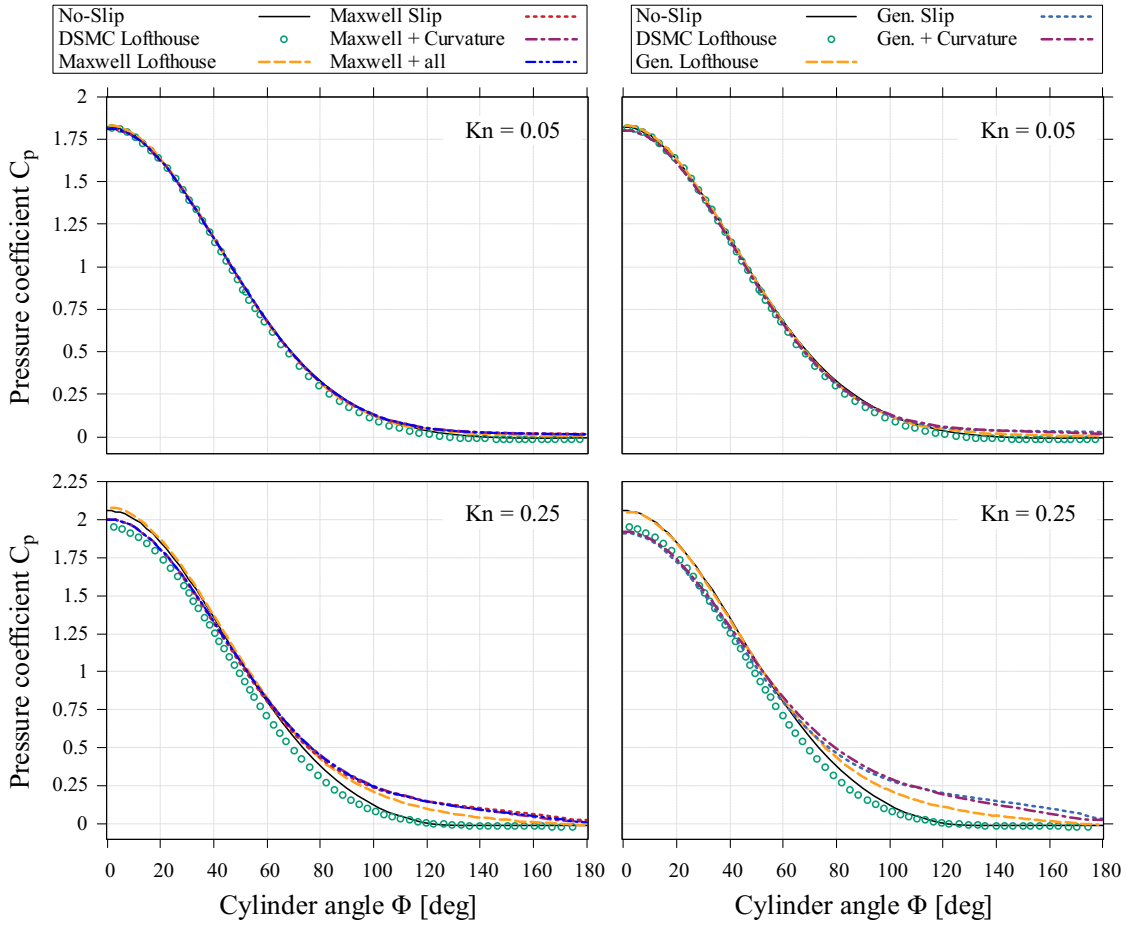

Figure 5.14.: Pressure coefficient C_p along the cylinder surface at Kn = 0.05 and Kn = 0.25. The Maxwell slip conditions are displayed on the left and the generalised slip conditions on the right. Reference Lofthouse data from [2].

5.2.3. Viscous Normal Force

During the analysis of the surface properties we observed the existence of a viscous normal force, which interferes with the pressure force at the surface of the cylinder. To analyse the whole force acting in the direction normal to the surface, we introduced a normal-force coefficient C_N analogously to the pressure coefficient C_p:

$$C_\mathrm{N} = \frac{(\mathbf{f}_\mathrm{loc} \cdot \mathbf{n}_i)/A_i - p_\infty}{\frac{1}{2}\rho_\infty U_\infty^2}$$

where $\mathbf{f}_{\text{loc}}$ describes the local force acting on the surface element and $\mathbf{n}_i$ and A_i describe the surface normal vector, pointing into the surface, and the area of the surface element. In the DSMC method, all local normal forces are interpreted as pressure forces and thus, for the DSMC solutions the pressure coefficient is equivalent to this definition of the normal-force coefficient. The distribution of the normal-force coefficient along the cylinder surface is displayed in fig. 5.15.
For Kn = 0.05, all conditions agree precisely with the DSMC data but some negative values are observed for $\Phi > 120°$. For Kn = 0.25, the no-slip and Maxwell slip solution match the DSMC curve well up to an angle of $\Phi = 80°$. Both solutions then proceed to predict negative normal -force values, where the Maxwell solution shows a stronger deviation from the DSMC data. The generalised slip solution overpredicts the normal force at the windward side of the cylinder and proceeds to underpredict it on the leeward side. In contrast to Kn = 0.05, negative normal-force values are already observed for $\Phi > 100°$ for the slip boundary conditions. The same trends were observed for the slip boundary conditions when extended with the additional curvature and thermal creep terms.

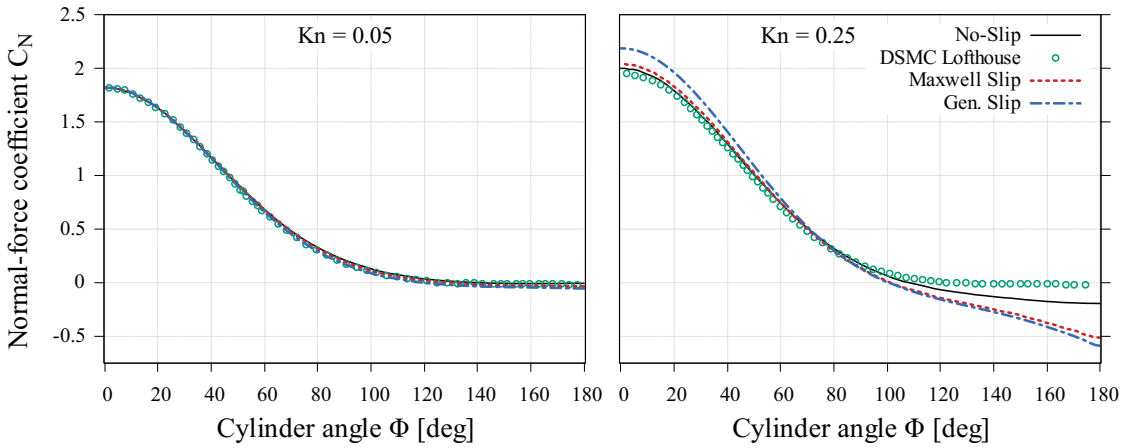

Figure 5.15.: Normal-force coefficient C_N along the cylinder surface at Kn = 0.05 and Kn = 0.25. Reference Lofthouse data from [2].

Comparing fig. 5.14 and 5.15, the pressure and normal-force coefficients are almost identical for the Kn = 0.05 case. For the Kn = 0.25 case, however, considering the viscous normal force eliminates the overestimation by the no-slip condition at the windward side of the cylinder. Moreover, the strong overprediction observed for the slip boundary conditions at the leeward side of the cylinder is removed. Yet, the viscous normal force creates negative force values at the leeward side of the cylinder

for all boundary conditions, leading to a strong underprediction of the normal force.

Furthermore, we analysed the influence of the viscous normal force on the drag coefficient. In contrast to the flat plate, the drag of the cylinder is not solely due to skin friction. Instead, the drag coefficient is composed of a skin friction and pressure part and, as discussed below, a viscous normal force part.
Fig. 5.16 shows the total drag separated into the contributing forces. Here, the viscous forces are divided into tangential and normal components, referred to as friction and viscous normal force. For both Knudsen numbers, the contribution of the viscous normal force to the total drag is negligible ($< 1\,\%$) for the no-slip solution. At $\mathrm{Kn} = 0.05$, the contribution is smaller than $3\,\%$ for the generalised slip conditions and smaller than $1.5\,\%$ for the Maxwell slip conditions. In contrast, at $\mathrm{Kn} = 0.25$ the viscous normal force accounts for more than $12\,\%$ of the total drag for the generalised slip conditions and less than $10\,\%$ for the Maxwell conditions.

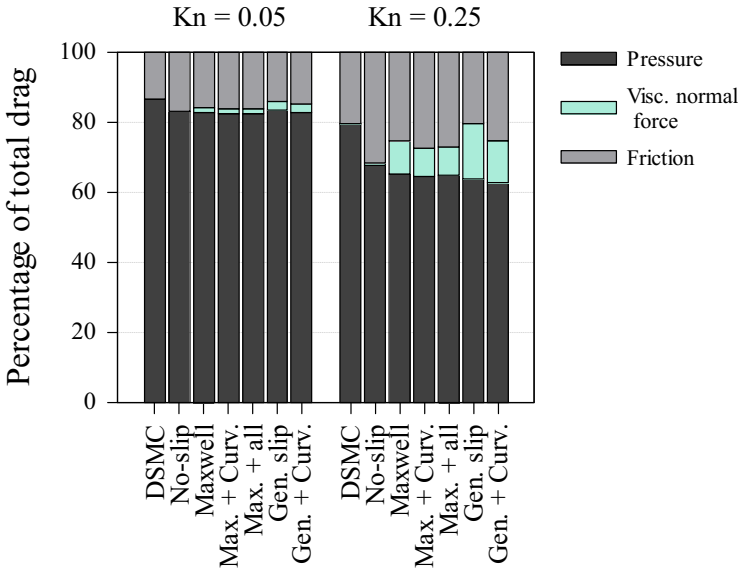

Figure 5.16.: Contribution to the toal drag of the pressure, friction and viscous normal force components at $\mathrm{Kn} = 0.05$ and $\mathrm{Kn} = 0.25$. Reference DSMC data from [2].

In general, the existence of a viscous normal force is not a side effect of the slip boundary conditions, since it is observed for the no-slip condition as well. However, the use of slip boundary conditions seems to intensify this phenomenon. Towards lower Knudsen numbers, the viscous normal force becomes less pronounced, leading to the assumption that it is a rarefaction effect that only occurs in a highly rarefied

flow. As observed in fig. 5.16, the contribution of the viscous normal force to the total drag is not negligible for large Knudsen numbers.
From a physical perspective, a negative normal force would result in the fluid to "tug" at the surface. To answer whether this phenomenon describes the actual physics at the wall or is just a computational artefact requires further investigations.

5.2.4. Drag Coefficient

In tab. 5.10, the drag coefficient C_D is displayed for all boundary conditions at Kn = 0.05. The results for the Kn = 0.25 case are displayed in tab. A.1.
All boundary conditions predict the drag coefficient with a deviation of less than 4 % from the DSMC value. The generalised slip solutions, including Lofthouse's solution, show the best prediction of the drag coefficient, closely followed by the Maxwell solutions. As observed for the peak heating, the effect of the curvature and thermal creep terms is rather small. In the case of the Maxwell slip condition, adding the curvature and thermal creep terms slightly increases the deviation from the DSMC data but the changes are in the magnitude of 0.1 %. The same is observed for the generalised slip condition, where the addition of the curvature term slightly decreases the deviation from the DSMC result.

Table 5.10.: Surface properties for the cylinder case and the percentage deviation from DSMC data at Kn = 0.05. Lofthouse data from [2].

Surf. Property (% dev.)	Drag C_D	Peak heating [kW m^{-2}]
DSMC Lofthouse	1.499 (0.0 %)	15.85 (0.0 %)
No-Slip	1.557 (3.9 %)	16.80 (6.0 %)
Maxwell Lofthouse	1.536 (2.5 %)	17.20 (8.5 %)
Maxwell	1.533 (2.3 %)	15.57 (-1.8 %)
Maxwell + Curvature	1.538 (2.6 %)	15.79 (-0.4 %)
Maxwell + Curv. + Therm. Creep	1.537 (2.5 %)	15.79 (-0.4 %)
Gen. Slip Lofthouse	1.508 (0.6 %)	16.63 (4.9 %)
Gen. Slip	1.491 (-0.5 %)	13.97 (-11.9 %)
Gen. Slip + Curvature	1.504 (0.3 %)	13.90 (-12.3 %)

For Kn = 0.25, the generalised slip solution provides the best agreement with the

DSMC data, followed by the simple Maxwell slip and no-slip solutions. Here, including the curvature and thermal creep terms increases the deviation from the DSMC value for both slip conditions by 2 % to 6 %. Compared to the Lofthouse solutions, the current implementation shows a significant increase in the deviations from the DSMC data. For the Maxwell slip solution, the deviation is doubled and the deviation for the generalised slip condition increases by 10-fold. However, the Kn = 0.25 flow is a highly rarefied case and the purpose of the current implementation is to model flows in the near continuum and slip regime.

As depicted in fig. 5.16, the drag coefficient is dominated by the pressure forces for both Knudsen numbers. At Kn = 0.05, the pressure part accounts for approximately 83 % of the total drag and the friction part accounts for 15 % on average. At Kn = 0.25, the pressure only amounts to an average of 66 % and the friction part adds up to an average of approximately 20 %. Hence, for both Knudsen numbers, differences in the local skin friction distribution are contributing little to the overall drag coefficient which is dominated by the prediction of the pressure forces.

5.2.5. Discussion

In general, the differences between Lofthouse's results and our results are attributed to the gradient update method used in the current implementation. Furthermore, Lofthouse implemented the generalised slip condition as originally proposed by [9], resulting in rather strong deviations from the results computed with the generalised slip condition used in this study.
Compared to Lofthouse's results, a clear improvement in the agreement of the heating coefficient with the DSMC data is achieved with the current implementation of the Maxwell slip condition. For the skin friction, the current implementation provides different solutions compared to Lofthouse's results, over- or underestimating the DSMC data at different positions of the cylinder. Yet, the overall deviations from the DSMC data remain nearly unchanged for small Knudsen numbers, as discussed for the drag coefficient. The pressure coefficient appears to be generally less sensitive to changes in the wall boundary conditions but the same trend as for the skin friction is observed. The overall deviation from the DSMC data appears to remain the same, whereas the current implementation improves the prediction of the surface pressure compared to Lofthouse's results in some places and impairs it in other places. In general, the results of both studies agree sufficiently well with

the DSMC data in the slip regime.

The additional terms appear to influence the skin friction the most but show only small changes for the heating and pressure coefficient. However, this trend was to be expected, since the additional terms only influence the slip velocity at the wall and thus, directly affect the skin friction but the other flow properties are affected only indirectly.

5.3. Test Case 3: SHEFEX III

In this section, we investigated the applicability of the current implementation on a practical re-entry configuration. As a third test case, we simulated the DLR SHEFEX III vehicle, which is a slender re-entry configuration from the SHEFEX flight test programme. Here, reference experimental data [53] for the aerodynamic forces are available from measurements in the 2nd test section of the Hypersonic Vacuum Wind Tunnel Göttingen (V2G) at the German Aerospace Center, Göttingen.

The test gas is nitrogen and the gas properties are the same as in tab. 5.1. As for the flat plate cases, nitrogen was modelled as an ideal gas in thermal equilibrium. Hannemann et al. [25] investigated the effect of the Maxwell slip condition, as implemented into the TAU code by Winkler [24] (see sec. 4.1), on the aerodynamic forces acting on the vehicle at four different Knudsen numbers. In this study, we chose the Knudsen number cases closest to the continuum regime and furthest away from the continuum regime. The simulation conditions for the two Knudsen number cases are displayed in tab. 5.11. Both conditions were simulated at an angle of attack (AOA) of 30° and condition 1 was further tested at an angle of attack of 0°. Note that the denotation of the two flow conditions is not equivalent to the one in [25].

Table 5.11.: Simulation conditions for the SHEFEX III configuration.

	ρ_∞ [kg m^{-3}]	Ma$_\infty$	U_∞ [m s^{-1}]	T_∞ [K]	T_w [K]	Gas	Kn
Cond. 1	$2.8113 \cdot 10^{-5}$	23.33	1693.12	12.67	300	N_2	$7.28 \cdot 10^{-3}$
Cond. 2	$2.8076 \cdot 10^{-4}$	11.97	995.57	16.64	300	N_2	$7.21 \cdot 10^{-4}$

In her Master's thesis, Winkler [24] performed a grid independence study for the SHEFEX configuration, which strongly suggested the grid independence of the presented solutions. Thus, no separate grid independence study was conducted here and the grid from Winklers's work [24] was adapted. A section of the computational grid is displayed in fig. 5.17. The grid consists of a structured grid in the proximity of the vehicle's surface combined with an unstructured grid in the remaining simulation area.

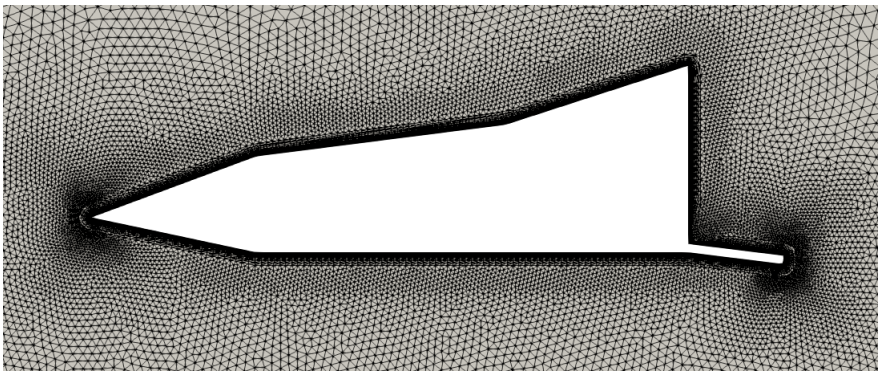

Figure 5.17.: Section of the computational grid for the SHEFEX III configuration.

In the following sections, the distribution of the local surface forces along the vehicle is evaluated for a contour parallel (red, fig. 5.18) to the symmetry axis and a contour perpendicular (blue, fig. 5.18) to the symmetry axis. The contour parallel to the symmetry axis is shifted slightly from the actual symmetry axis to rule out any edge effects. Furthermore, the surface normal vector is not clearly defined directly on the symmetry axis, which interferes with the evaluation of the surface forces.

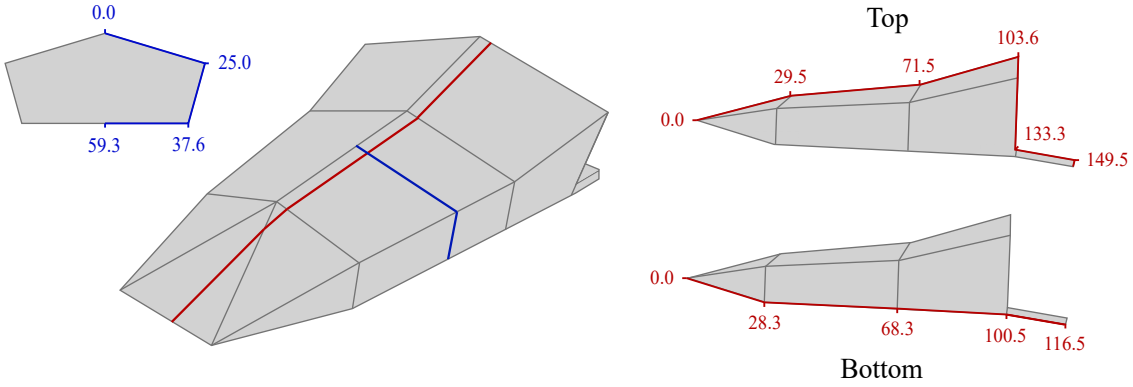

Figure 5.18.: Surface contours parallel and perpendicular to the symmetry axis. The numbers mark the distance from the leading edge or the symmetry axis measured in mm. Adapted from [25].

In this section, we directly acknowledge the possible existence of a viscous normal force and compare the different boundary conditions based on the normal-force coefficient C_N and tangential-force coefficient C_T:

$$C_\mathrm{N} = \frac{|\mathbf{f}_\mathrm{N}|}{\frac{1}{2}\rho_\infty U_\infty^2 \cdot A_i} \qquad \text{and} \qquad C_\mathrm{T} = \frac{|\mathbf{f}_\mathrm{T}|}{\frac{1}{2}\rho_\infty U_\infty^2 \cdot A_i}$$

where $\mathbf{f}_\mathrm{N}$ and $\mathbf{f}_\mathrm{T}$ describe the local normal and tangential force acting on the surface element A_i. Note that, compared to the cylinder case, the normal-force coefficient has been slightly modified here to be consistent with the definition of the tangential-force coefficient.

5.3.1. Angle of Attack 30°

Fig. 5.19 and 5.20 show the normal-force and tangential-force coefficients along the surface contour parallel to the symmetry axis. The labels "top" and "bottom" refer to the leeward and windward parts of the surface contour. In both cases, the distance from the leading edge measures the length of the contour, starting at the leading edge. In the following, only the effects of the Maxwell and generalised slip conditions have been analysed without including the additional terms. Extending the conditions with the curvature and thermal creep terms resulted in the simulations becoming unstable.

At the bottom of the vehicle, all boundary conditions agree closely with the DSMC solution. For condition 1, some minor differences between the individual boundary conditions are observed towards the back of the vehicle, where the generalised slip predicts the highest normal-force, followed by the Maxwell slip and the no-slip condition. For condition 2, these differences do not exist, since all solutions agree precisely with each other along the whole bottom of the vehicle.
At the top of the vehicle, the DSMC solution predicts almost no normal forces for condition 1, whereas the Navier-Stokes solutions are fluctuating strongly. Close to the leading edge, the slip solutions agree better with the DSMC solution than compared to the no-slip solution but then proceed to overestimate the normal forces. For a small section, the no-slip solution agrees closely with the DSMC curve but towards the back of the vehicle all boundary conditions tend to overestimate the normal forces. The results for the normal-force coefficient for condition 1 are inconclusive regarding which boundary condition provides the best agreement with the

DSMC data.The strong peaks observed in the normal-force distribution indicate the positions on the vehicle where two planes meet and create a sharp edge. The use of slip boundary conditions seems to intensify the magnitude of these peaks.

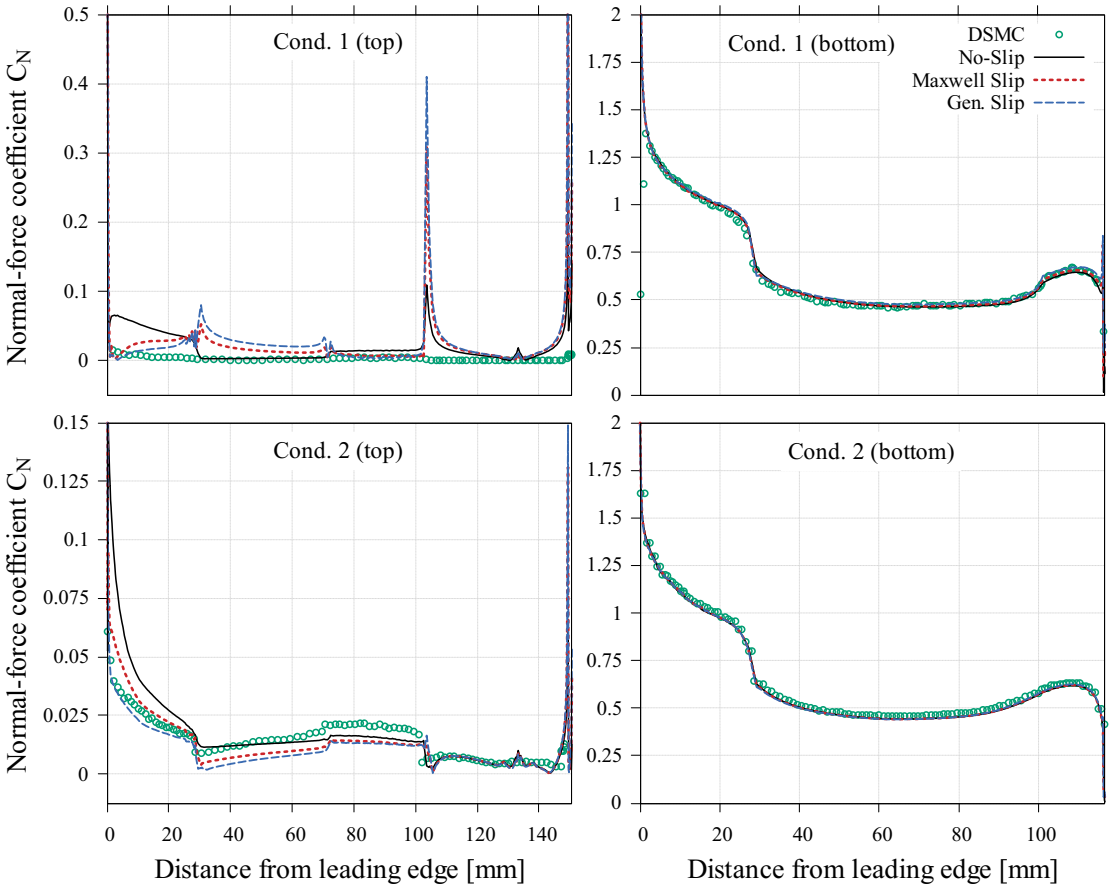

Figure 5.19.: Normal-force coefficient C_N for conditions 1 and 2 at 30° angle of attack, plotted along the top and bottom of the SHEFEX configuration. DSMC data from [25].

For condition 2, the DSMC solution shows non-zero normal forces along the whole top of the vehicle and the Navier-Stokes solutions capture the overall shape of the curve better than compared to condition 1. Towards the leading edge, the generalised slip condition agrees best with the DSMC curve but then slightly underestimates the normal forces towards the middle of the vehicle. The Maxwell slip solution shows the opposite behaviour. First, the normal force is overestimated but then the Maxwell slip solution agrees closely with the DSMC curve. The no-slip solution generally overestimates the normal force at the leading edge and along the whole front plane of the vehicle. However, along the middle of the vehicle, the no-

slip solution slightly underestimates the normal force but shows the lowest deviation from the DSMC curve. Towards the back of the vehicle, all boundary conditions agree closely with each other and the DSMC solution except for the peak at the trailing edge. Compared to condition 1, the normal force distribution is more continuous and shows only some minor peaks around the edges of the vehicle at this flow condition.

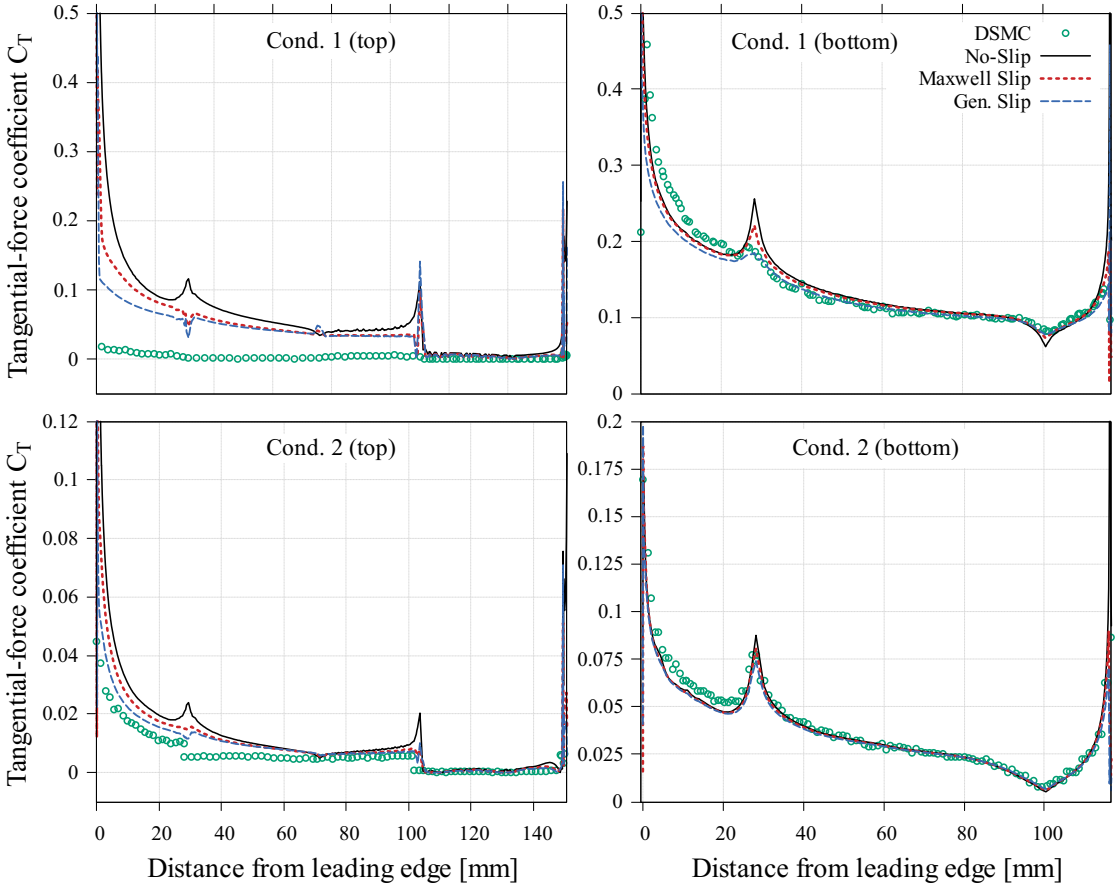

Figure 5.20.: Tangential-force coefficient C_T for conditions 1 and 2 at 30° angle of attack, plotted along the top and bottom of the SHEFEX configuration. DSMC data from [25].

Fig. 5.20 shows the tangential-force coefficient along the vehicle's top and bottom side for both flow conditions. At the bottom of the vehicle, all boundary conditions underestimate the tangential forces along the complete front plane at both flow conditions. Similar to the normal-force coefficient, there are some minor differences between the individual boundary conditions for condition 1, whereas these differences disappear for condition 2. For condition 1, the generalised slip solution agrees best with the DSMC data for the majority of the bottom side except for the

plane at the leading edge. Here, the no-slip and Maxwell slip solutions are closest to the DSMC curve but they proceed to overestimate the peak where the front plane connects to the next plane. For condition 2, all boundary conditions agree closely with each other and the DSMC solution for the majority of the bottom side of the vehicle. The prediction of the peak, where the front and middle plane connect, appears to be slightly improved by the use of slip boundary conditions.

Along the top of the vehicle, the DSMC solution predicts almost no tangential forces for condition 1, similar to the normal forces. Here, applying slip boundary conditions shows a clear improvement of the predicted tangential forces for the majority of the vehicle. At the front of the vehicle, the generalised slip solution is closest to the DSMC solution but some deviation remains. For the rest of the vehicle, the Maxwell and generalised slip solutions are almost identical and slightly improve the prediction of the tangential forces compared to the no-slip solution. At the back of the vehicle, all boundary conditions agree closely with each other and match the DSMC data well except for the peak at the trailing edge.
The same trend is observed for condition 2. However, here the DSMC solution predicts non-zero tangential forces and the deviations from the DSMC data are significantly smaller for all boundary conditions than compared to condition 1. As for the bottom side of the vehicle, the differences between the individual boundary conditions are smaller compared to condition 1.

Fig. 5.21 displays the normal and tangential-force coefficient along the surface contour perpendicular to the symmetry axis of the vehicle. For the normal-force coefficient, all boundary conditions agree well with the DSMC data for both flow conditions. For condition 1, the no-slip solution agrees precisely with the DSMC data at the top of the vehicle, whereas the slip conditions tend to slightly overestimate the normal force near the symmetry axis and towards the edge of the top plane. At the side of the vehicle, the no-slip solution matches the DSMC curve well but the solutions obtained with the slip boundary conditions better capture the qualitative shape of the DSMC curve for this section. Where the side plane joins the bottom plane, the Maxwell slip solution matches the DSMC data best, while the no-slip solution slightly overestimates the normal forces and the generalised slip solution underestimates them. The generalised slip solution overestimates the DSMC solution lightly at the bottom of the vehicle, where the no-slip solution matches the

DSMC curve accurately. For this section of the vehicle, the Maxwell slip condition does not seem to influence the normal forces and agrees precisely with the no-slip solution. As seen before, the use of slip boundary conditions increases the intensity of the peaks around the edges of the vehicle.
For condition 2, the differences between the different boundary conditions are minor and all solutions match the DSMC data well. At the side and bottom of the vehicle, however, all conditions slightly underestimate the normal forces, where the no-slip curve is closest to the DSMC curve.

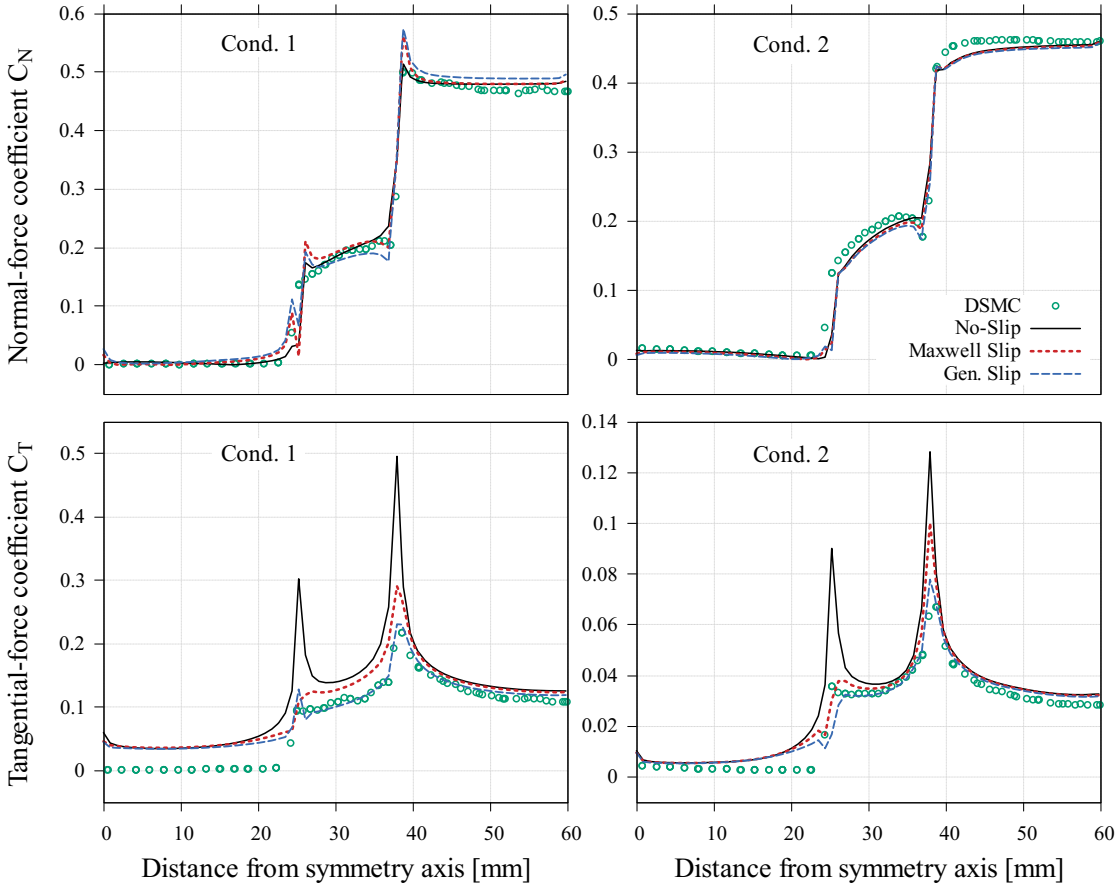

Figure 5.21.: Normal- and tangential-force coefficients C_N and C_T for conditions 1 and 2 at 30° angle of attack, plotted perpendicular to the symmetry axis of the SHEFEX configuration. DSMC data from [25].

The tangential-force coefficient shows clear differences between the individual boundary conditions especially at the side of the vehicle. For both flow conditions, all boundary conditions agree closely with each other at the top and bottom of the vehicle but start to vary towards the edges of the vehicle. In contrast to the normal-

force distribution, the peaks in the tangential-force distribution around the edges of the vehicle are most pronounced in the no-slip solution. Here, applying slip boundary conditions significantly decreases the intensity of these peaks.
For condition 1, all boundary conditions overestimate the tangential forces at the top of the vehicle but the no-slip solution further overpredicts the tangential force at the edges of the vehicle drastically. Compared to the no-slip solution, the Maxwell slip condition decreases the deviation from the DSMC data especially along the side of the vehicle. Yet, the generalised slip condition matches the DSMC curve best at the side and bottom plane of the vehicle.
The same trend is observed for condition 2 but the overall differences between the individual boundary conditions and the deviation from the DSMC data is smaller than compared to condition 1. Furthermore, all boundary conditions agree well with the DSMC data at the top of the vehicle and only slightly overestimate the tangential forces towards the side of the vehicle.

5.3.2. Angle of Attack 0°

For condition 1, we further simulated the SHEFEX case at an angle of attack of 0° to analyse the effects of the slip boundary conditions without the highly rarefied flow at the top of the vehicle, as observed for 30° angle of attack.
Fig. 5.22 shows the normal- and tangential-force coefficient along the vehicle parallel to the symmetry axis. At the top and bottom of the vehicle, all boundary conditions overestimate the normal force directly at the leading edge. At the top of the vehicle, the generalised slip solution agrees well with the DSMC curve at the beginning of the front plane but then joins the Maxwell slip and no-slip solutions and slightly overestimates the normal forces. Along the middle of the vehicle, the generalised slip and Maxwell slip solutions both agree precisely with the DSMC curve but the Maxwell slip appears to match the DSMC data slightly better. The no-slip solution shows only a small deviation from the DSMC curve as well. Towards the back of the vehicle, the no-slip solution agrees accurately with the DSMC curve, whereas the generalised and Maxwell slip tend to overestimate the normal forces slightly. At the back of the vehicle, all boundary conditions agree closely with each other where the no-slip solution is closest to the DSMC curve.

At the bottom of the vehicle, applying slip boundary conditions improves the prediction of the normal forces along the whole surface. The generalised slip solution

tends to slightly underestimate the normal forces, while the Maxwell slip solution tends to overestimate them. However, both slip conditions are in close agreement with the DSMC data along the whole bottom side. The no-slip solution shows the strongest deviation from the DSMC data but still predicts the normal forces sufficiently well. Again, the peaks around the edges of the vehicle are intensified by the use of slip boundary conditions, where the generalised slip shows the strongest peaks.

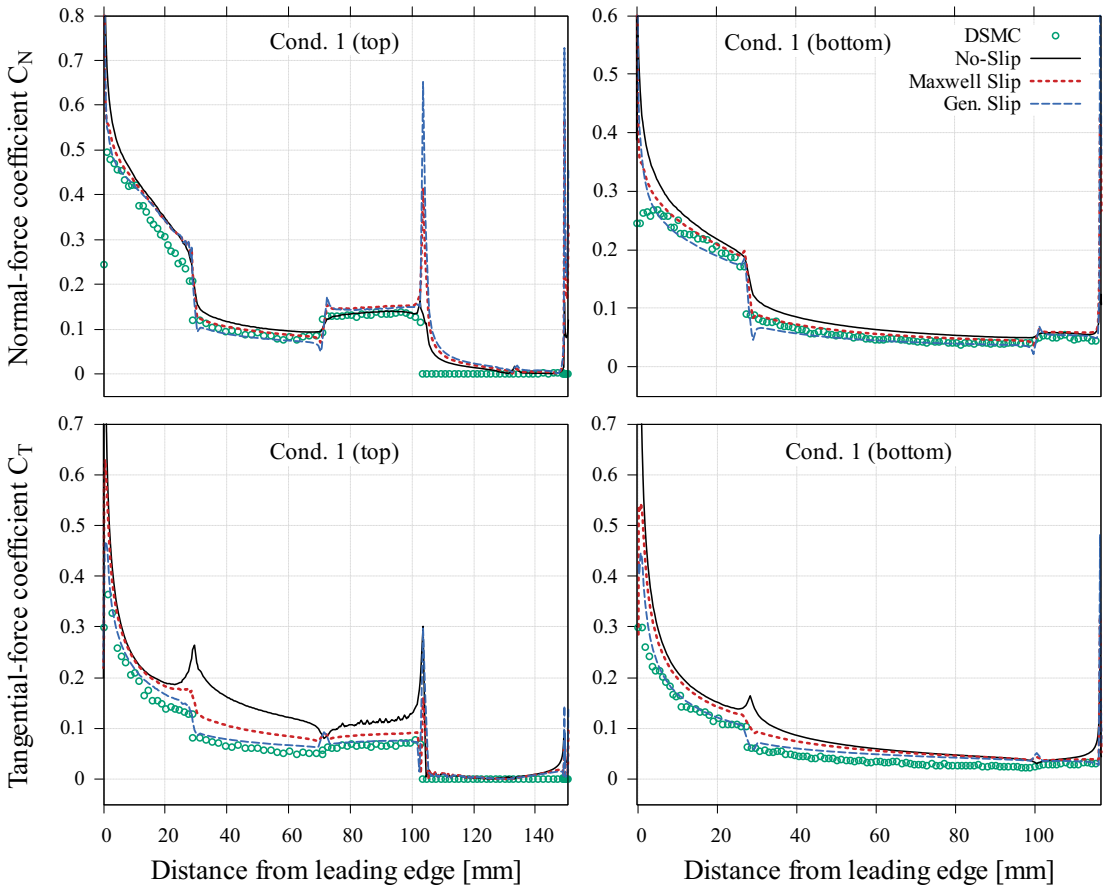

Figure 5.22.: Normal- and tangential-force coefficients C_N and C_T for condition 1 at 0° angle of attack, plotted along the top and bottom of the SHEFEX configuration. DSMC data from F. Ziese[4].

For the tangential-force coefficient, a clear trend can be observed at the top and bottom of the vehicle. Here, the generalised slip solution agrees best with the DSMC data along the whole vehicle, followed by the Maxwell slip and no-slip solutions.

[4]Personal communication

At the top of the vehicle, all boundary conditions show only small differences between each other in the front and back of the vehicle. Along the middle of the vehicle, however, strong deviations between the individual boundary conditions are observed. Here, the no-slip solution strongly overestimates the tangential forces and shows some fluctuations towards the back of the vehicle. The Maxwell slip solution decreases the deviation from the DSMC data compared to the no-slip condition but not as effectively as the generalised slip condition.
At the bottom of the vehicle, the differences between the individual boundary conditions and the deviations from the DSMC data are smaller compared to the top of the vehicle. The slip boundary conditions show the strongest effect at the front of the vehicle but then slowly converge towards the no-slip solution. At the trailing edge, some minor deviations from the no-slip solution are observed for both slip conditions, slightly improving the agreement with the DSMC data. As observed at 30°, the use of slip boundary conditions reduces the intensity of the peaks at the edges of the vehicle.

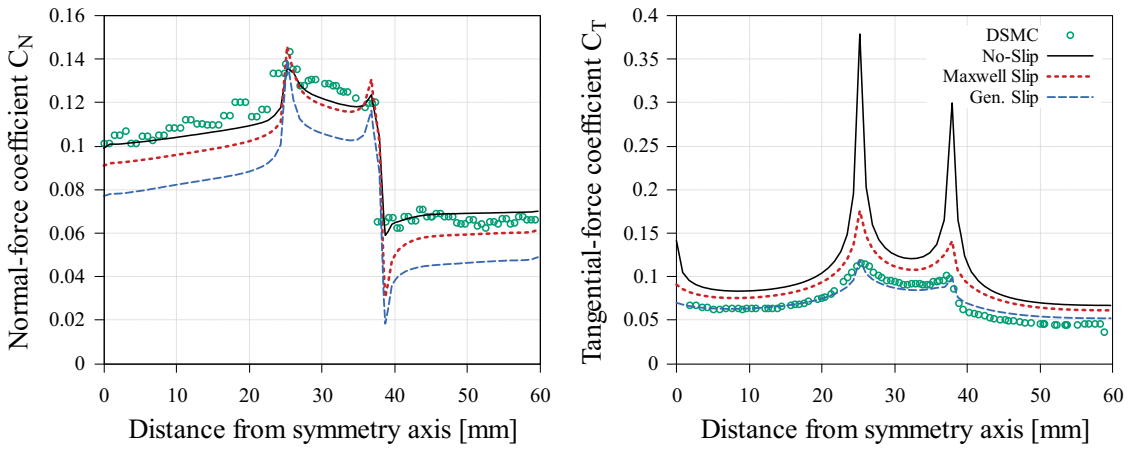

Figure 5.23.: Normal- and tangential-force coefficients C_N and C_T for condition 1 at 0° angle of attack, plotted perpendicular to the symmetry axis of the SHEFEX configuration. DSMC data from F. Ziese[5].

Similar trends are observed for the normal and tangential-force coefficient along the surface contour perpendicular to the symmetry axis (fig. 5.23). The no-slip solution provides a good prediction of the normal forces along the complete surface contour, agreeing well with the reference DSMC data. Here, the use of slip boundary condition increases the deviation from DSMC data for both slip conditions. While the

[5]Personal communication

Maxwell solution shows only minor differences from the no-slip solution at the side of the vehicle, the generalised slip condition strongly underestimates the normal forces along the whole surface contour.
For the tangential-force coefficient the exact opposite behaviour is observed. The generalised slip solution agrees precisely with the DSMC curve along the complete contour, while the no-slip solution significantly overestimates the tangential forces. As in fig. 5.22, the Maxwell slip solution decreases the deviation from the DSMC data compared to the no-slip solution but not as strongly as the generalised slip. Overall, the differences between the boundary conditions are more pronounced for the tangential-force coefficient than for the normal-force coefficient. The peaks around the edges of the vehicle are decreased by the application of slip boundary conditions, as observed at an angle of attack of 30°.

5.3.3. Aerodynamic Efficiency

To better quantify the effects of the slip boundary conditions we analysed the drag and lift coefficients of the vehicle and its aerodynamic efficiency. Fig. 5.24 shows the computed absolute value of the aerodynamic efficiency for all three cases. At an angle of attack of 0°, the vehicle is pushed downwards resulting in a negative lift coefficient and thus a negative aerodynamic efficiency.

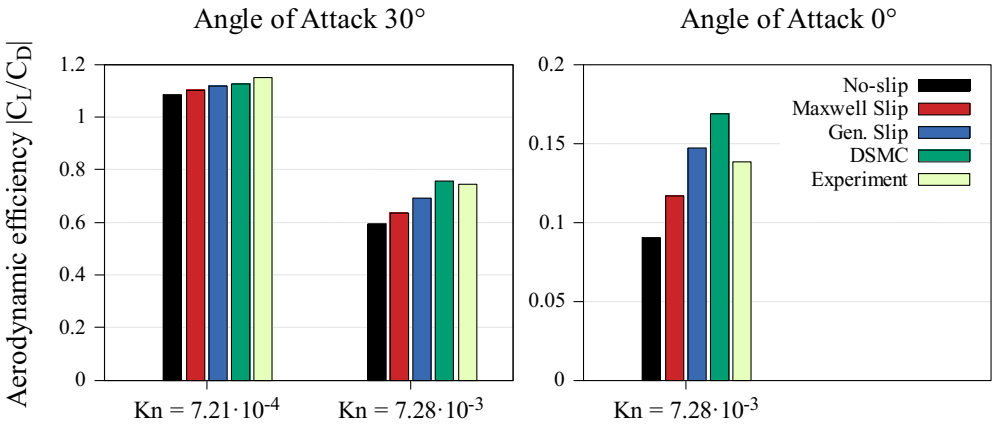

Figure 5.24.: Aerodynamic efficiency of the SHEFEX configuration for the three flow conditions. DSMC and experimental data from [25, 53].

For all three cases, a clear trend is observed that the slip boundary conditions decrease the deviation from the DSMC data compared to the no-slip condition. The generalised slip condition shows the least deviation from the DSMC and experimen-

tal data, followed by the Maxwell slip condition. As observed for the local force distributions, the differences between the specific boundary conditions are larger for the high Knudsen number flow (cond. 1). However, the changes in the deviation from the DSMC and experimental data are strongest at an angle of attack of 0°. Here, the generalised slip solution agrees even better with the experimental data than compared to the DSMC result.

Table 5.12.: Surface properties for the SHEFEX configuration and the percentage deviation from experimental data for condition 1. Experimental data from [53].

Prop.	Cond. 1, 30° AOA		Cond. 1, 0° AOA	
(% dev.)	Drag C_D	Lift C_L	Drag C_D	Lift C_L
Exp.	0.6200 (0.0 %)	0.4610 (0.0 %)	0.2970 (0.0 %)	-0.0409 (0.0 %)
DSMC	0.6114 (-1.4 %)	0.4620 (0.2 %)	0.3060 (3.0 %)	-0.0516 (26.2 %)
No-slip	0.7500 (21.0 %)	0.4444 (-3.6 %)	0.4171 (40.4 %)	-0.0376 (-8.1 %)
Maxwell	0.7112 (14.7 %)	0.4530 (-1.7 %)	0.3664 (23.4 %)	-0.0427 (4.4 %)
Gen. Slip	0.6838 (10.3 %)	0.4714 (2.3 %)	0.3184 (7.2 %)	-0.0467 (14.2 %)

Prop.	Cond. 2, 30° AOA	
(% dev.)	Drag C_D	Lift C_L
Exp.	0.4590 (0.0 %)	0.5280 (0.0 %)
DSMC	0.4589 (-0.02 %)	0.5169 (-2.1 %)
No-slip	0.4662 (1.6 %)	0.5054 (-4.3 %)
Maxwell	0.4584 (-0.1 %)	0.5052 (-4.3 %)
Gen. Slip	0.4536 (-1.2 %)	0.5068 (-4.0 %)

Table 5.13.: Surface properties for the SHEFEX configuration and the percentage deviation from experimental data for condition 2. Experimental data from [53].

The drag and lift coefficients of all three cases are displayed in tab. 5.12 and 5.13. Applying slip boundary conditions generally decreases the drag coefficient and increases the lift coefficient, raising the aerodynamic efficiency of the vehicle. As observed above, the use of the generalised slip condition results in a stronger deviation from the no-slip solution compared to the Maxwell slip for the lift and drag values.

For condition 1, the no-slip solution overestimates the drag by 21 % at an angle of attack of 30° and by approximately 40 % at 0° angle of attack. The generalised slip solution reduces this deviation from the experimental value to approximately 10 % at an angle of attack of 30° and shows an even lower deviation for 0° angle of attack. For the lift coefficient, the Maxwell solution provides the best agreement with the experimental data for both angles of attack. However, at 30° angle of attack all boundary conditions agree well with the experiment and show only small deviations ($< 4\,\%$). At an angle of attack of 0°, the DSMC solution shows the highest deviation ($\approx 26\,\%$) for the lift coefficient, leading to the overestimation of the aerodynamic efficiency observed in fig. 5.24. For the Navier-Stokes solutions, the generalised slip solution deviates strongest from the experimental data, followed by the no-slip and Maxwell slip solution. In this case, the aerodynamic efficiency appears to be dominated by changes in the drag coefficient, since the changes in the deviations between the individual boundary conditions are a magnitude larger for the drag coefficient than compared to the lift coefficient.
For condition 2, the drag coefficient deviates from the experimental value by less than 2 % for all boundary conditions, where the Maxwell slip shows the smallest deviation. For the lift coefficient, all boundary conditions show approximately the same deviation of 4 %. As expected, the differences between the individual boundary conditions are smaller at the lower Knudsen number, resulting in less variation of the aerodynamic efficiency at this flow condition.

5.3.4. Discussion

Fig. A.10 shows the distribution of the local Knudsen number along the surface contour parallel to the symmetry axis. As expected, for an angle of attack of 30° the local Knudsen numbers are generally larger along the whole vehicle for condition 1 than compared to condition 2. Furthermore, the Knudsen numbers at the top of the vehicle are 2- to 3-fold higher than the ones at the bottom of the vehicle. Due to the rather high angle of attack the flow along the top of the vehicle is strongly rarefied, leading to an increase of the local Knudsen number.
The differences in the local Knudsen numbers along the top and bottom of the vehicle explain the variation in the differences between the individual wall boundary conditions. At the bottom of the vehicle, the local Knudsen number is small and thus, less variation between the different boundary conditions is observed for the normal- and tangential-force coefficients. Furthermore, the distribution of the local

Knudsen number is more continuous along the bottom of the vehicle, whereas the Knudsen number fluctuates strongly at the top of the vehicle. This explains why the results at the top of the SHEFEX configuration are less conclusive regarding which boundary condition provides the best agreement with the DSMC solutions. At an angle of attack of 0°, the local Knudsen numbers are of the same order of magnitude along the top and bottom of the vehicle, resulting in the differences between the individual boundary conditions to be more consistent along the top and bottom side of the vehicle.

As for the normal- and tangential-force coefficients, the peaks around the edges of the SHEFEX vehicle are also present in the local Knudsen number distributions. However, the physical interpretation and origin of these peaks is unclear. Furthermore, why the use of slip boundary conditions intensifies the peaks for the normal-force coefficient but reduces the peaks for the tangential-force coefficient is uncertain and requires further investigation.

6. Conclusion and Outlook

6.1. Conclusion

Table 6.1 summarises the effects of the Maxwell and generalised slip condition on the investigated test cases compared to the no-slip condition. The use of slip boundary conditions evidently improves the agreement of the local skin friction and heat flux with the DSMC data compared to the no-slip condition for all investigated test cases. Regarding the pressure and normal-force coefficients, the results were less conclusive. For the flat plate cases, the slip boundary solutions predict the surface pressure better than compared to the no-slip condition. For the cylinder and SHEFEX configuration, however, the no-slip condition already provides a good prediction of the pressure and normal-force coefficients, which is not generally improved by the use of slip boundary conditions.
Moreover, the prediction of the drag coefficient is clearly improved by applying slip boundary conditions for all cases. The prediction of the lift coefficient is generally improved as well but some discrepancies between the Maxwell and generalised slip conditions were observed.

For the flat plate cases and the SHEFEX configuration, the generalised slip condition reduces the deviation from the DSMC data most effectively for the majority of the surface properties. In contrast, for the cylinder case, the Maxwell slip condition is clearly superior to the generalised slip condition regarding the accuracy of the predicted skin friction and heating coefficients. Here, the improved agreement of the drag coefficient with the DSMC data observed for the generalised slip is due to the compensation of over- and underestimations of the local surface forces. This is further the reason for the good prediction of the integral heat flow by the no-slip condition, observed for Gökçen's flat plate case.
The addition of the curvature and thermal creep terms influence the local surface properties slightly but the effects on the integral properties are comparatively small.

Overall, which slip boundary condition provides the best agreement with the DSMC data strongly depends on the individual test case and the Knudsen number.

Table 6.1.: Summary of the effects of slip boundary conditions on the investigated test cases compared to the no-slip condition. The tangential-force coefficients are summarised in the friction results and the normal-force coefficients are summarised in the pressure results. +: Improvement, −: Impairment, /: Inconsistent results.

Test case	Boundary condition	Local Properties			Integral Properties		
		Friction	Heat	Pressure	Drag	Lift	Heat
Plate Gökçen	Maxwell	+	+	+	+	+	−
	Gen. Slip	+	+	+	+	+	−
Plate Metcalf	Maxwell	+	+	+	+	+	+
	Gen. Slip	+	+	+	+	−	+
Cylinder	Maxwell	+	+	−	+		
	Gen. Slip	−	−	−	+		
SHEFEX 30°	Maxwell	+		/	+	+	
	Gen. Slip	+		/	+	+	
SHEFEX 0°	Maxwell	+		/	+	+	
	Gen. Slip	+		/	+	−	

6.2. Outlook

In a subsequent study, the efficiency of the current implementation could be improved by implementing a routine that recomputes only the wall and near point gradients. The gradient calculation is computationally expensive and the current implementation performs the computation routine twice in each time step (fig. A.1). Since the slip velocities and temperatures at the wall only influence the gradients in the wall and near points, recomputing the gradients at all grid points is redundant. Limiting the second gradient computation to the wall and near points should thus reduce the computational cost of the slip boundary conditions.

Regarding the TAU-code, the current implementation should be tested with the other features of the code, such as different heat transfer conditions at the wall, simulation of gas mixtures or grid motion. For moving objects, the curvature term might be relevant for planar geometries as well, as discussed by Lockerby et al. [14]. Moreover, nitrogen was modelled as an ideal gas with no internal energy modes in this study but the effect of thermal non-equilibrium on the performance of the slip boundary conditions should be analysed in further studies.

To improve the performance of the slip boundary conditions, a study with various momentum and thermal accommodation coefficients could be conducted, similar to Le et al. [16]. Concerning the heat flux, the new temperature jump condition proposed by Le [18] showed promising results for the heat flux of a flat plate and might improve the agreement with the DSMC data for the flat plate cases investigated in this study. Further, the incorporation of a pressure jump condition into the TAU-code could be considered, to eliminate the inconsistencies observed for the normal-force distributions of the SHEFEX configuration.
To further test the current implementation, the SHEFEX coniguration could be simulated at more angles of attacks, similar to the study conducted by Hannemann et al. [54]. Finally, the origin and physical accuracy of the observed viscous normal forces should be subject to further investigations.

A. Supplementary Material

A.1. TAU-code

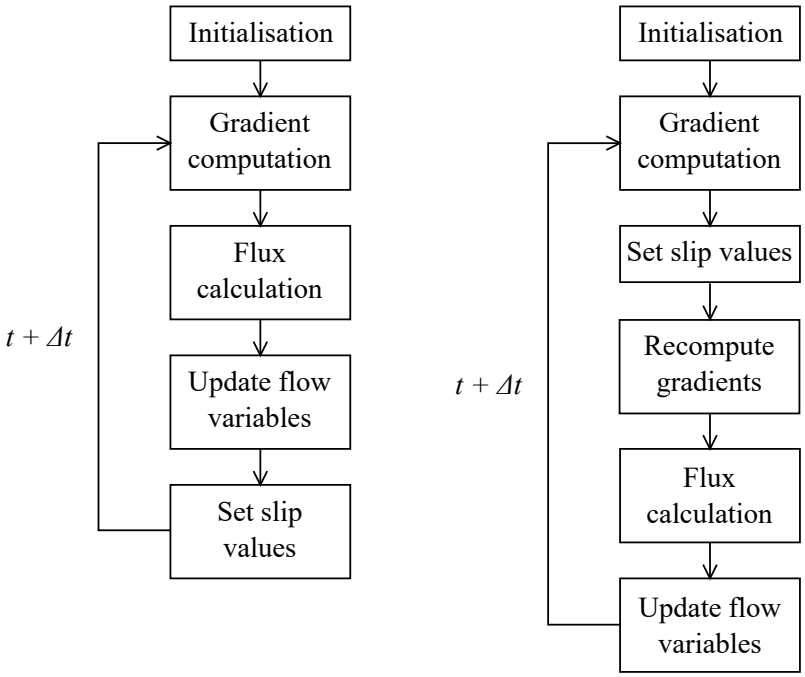

Figure A.1.: Simplified scheme of the TAU-code for an explicit time-stepping scheme. On the left, the slip values are set at the end of every time step, as described in sec. 4.2. On the right, the slip values are set after the initial gradient computation, as described in sec. 4.3.

A.2. Flat Plate

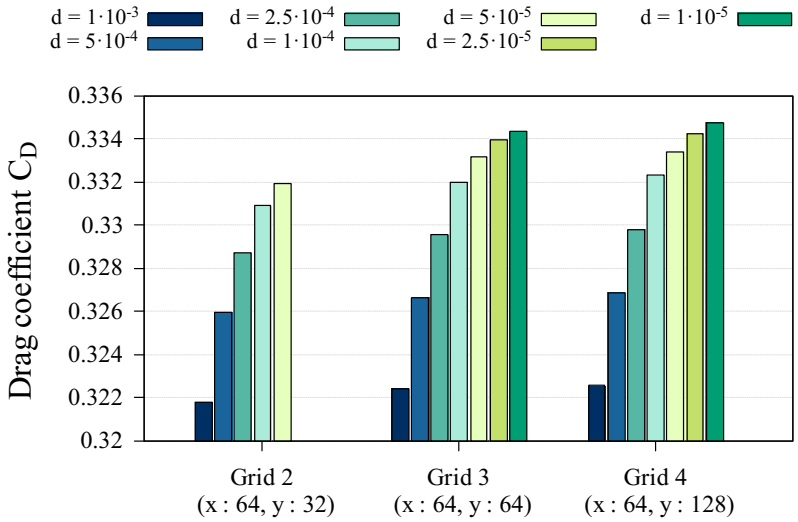

Figure A.2.: Grid independence study based on the drag coefficient C_D for the no-slip condition at Re = 100 and Kn = 0.104. The wall distance is denoted by d and the x and y values give the number of grid points parallel and perpendicular to the plate.

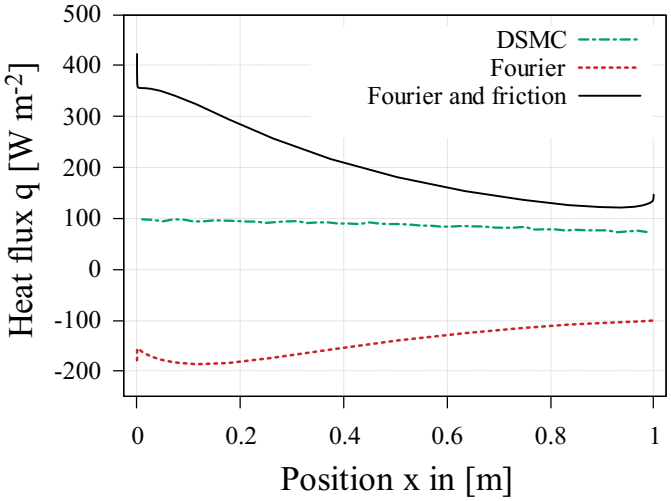

Figure A.3.: Heat flux q for the generalised slip condition along the flat plate, computed with and without the sliding friction term (equ. (2.14)) at Re=100 and Kn = 0.104. DSMC data from C. Hepp (personal communication).

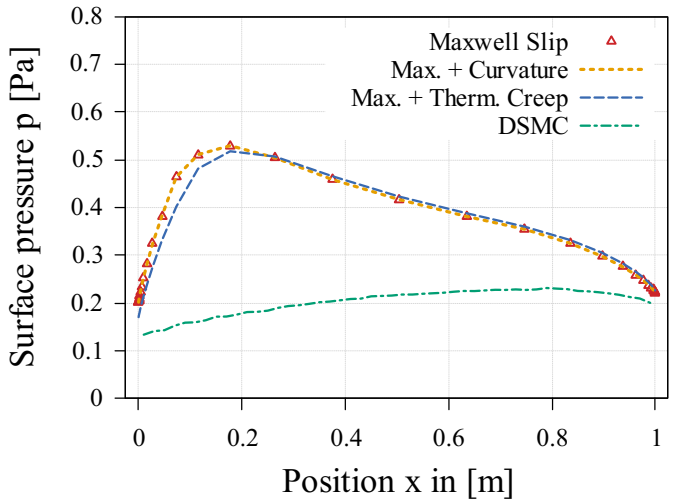

Figure A.4.: Surface pressure p along the plate for the Maxwell slip condition with and without the additional terms at Re = 100 and Kn = 0.104. DSMC data from C. Hepp (personal communication).

A.3. Cylinder

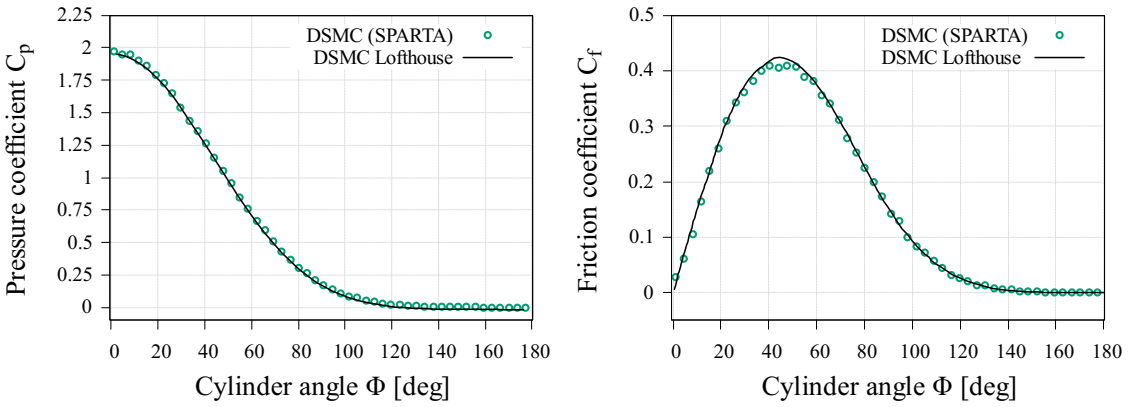

Figure A.5.: Validation of Lofthouse's DSMC results [2] for the pressure and friction coefficient C_p and C_f for the cylinder case. DSMC data from F. Ziese and C. Hepp (personal communication).

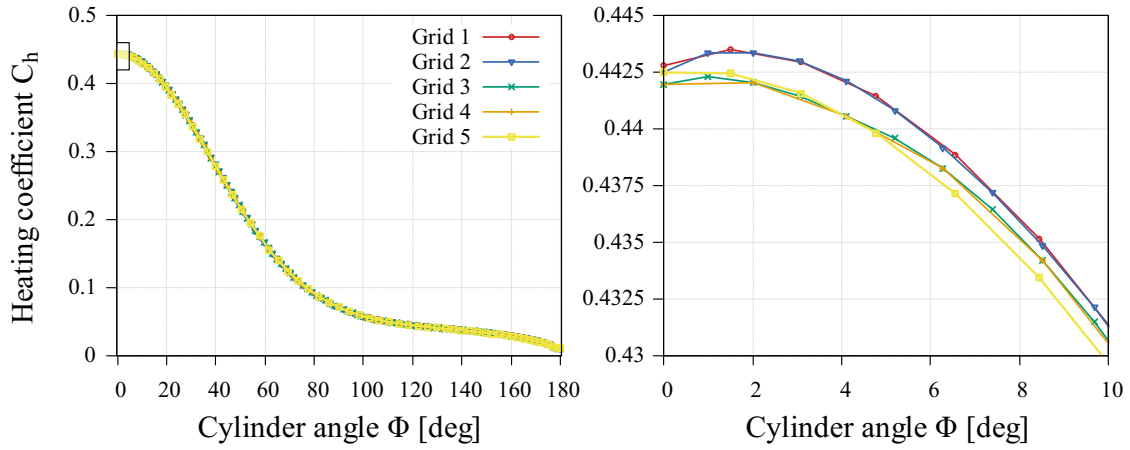

Figure A.6.: Grid independence study for the generalised slip condition based on the heating coefficient C_h, plotted along the cylinder surface at Kn = 0.25. The box in the left plot marks the magnified area displayed on the right.

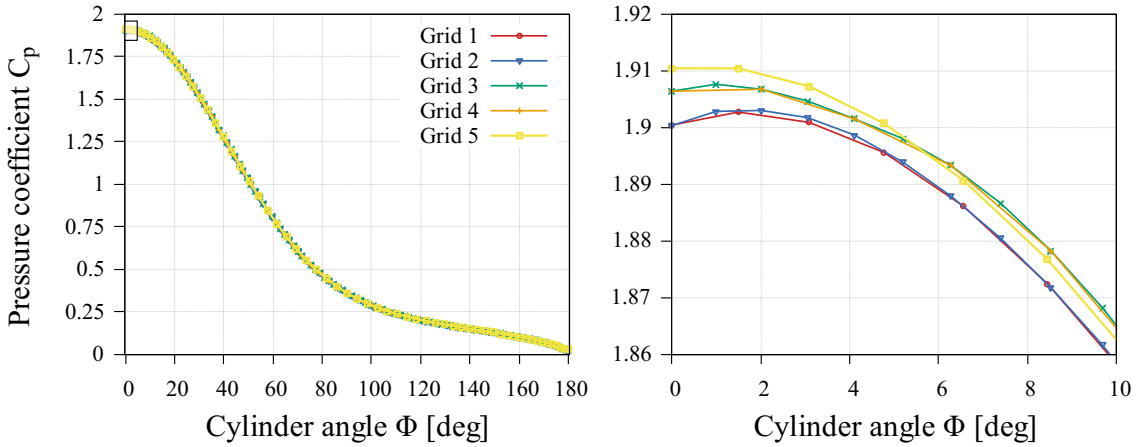

Figure A.7.: Grid independence study for the generalised slip condition based on the pressure coefficient C_p, plotted along the cylinder surface at Kn = 0.25. The box in the left plot marks the magnified area displayed on the right.

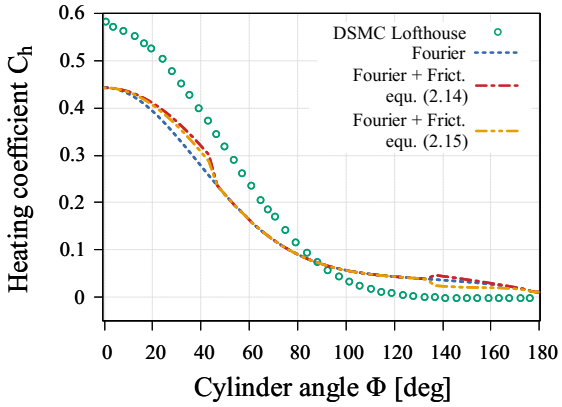

Figure A.8.: Heating coefficient C_h for the generalised slip condition along the cylinder surface, computed with and without the sliding friction terms (equ. (2.14) and (2.15)) at Kn = 0.25. DSMC data from [2].

Table A.1.: Surface properties for the cylinder case and the percentage deviation from DSMC data at Kn = 0.25. Lofthouse data from [2].

Surf. Property (% dev.)	Drag C_D	Peak heating [kW m^{-2}]
DSMC Lofthouse	1.769 (0.0 %)	5.926 (0.0 %)
No-Slip	2.213 (25.1 %)	7.227 (22.0 %)
Maxwell Lofthouse	1.941 (9.7 %)	7.040 (18.8 %)
Maxwell	2.095 (18.4 %)	6.228 (5.1 %)
Maxwell + Curvature	2.145 (21.3 %)	6.194 (4.5 %)
Maxwell + Curv. + Therm. Creep	2.137 (20.8 %)	6.193 (4.5 %)
Gen. Slip Lofthouse	1.748 (-1.2 %)	6.011 (1.4 %)
Gen. Slip	1.996 (12.8 %)	4.505 (-24.0 %)
Gen. Slip + Curvature	2.103 (18.9 %)	4.472 (-24.5 %)

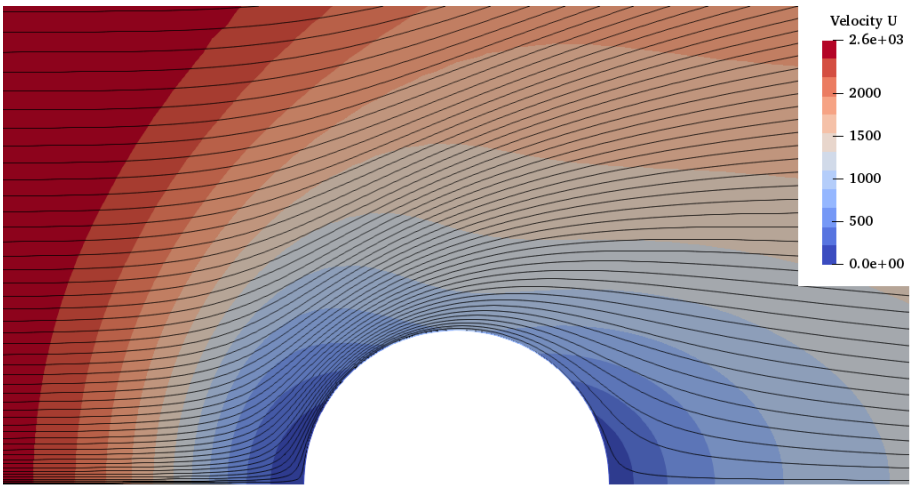

Figure A.9.: Streamlines and velocity isolines for the cylinder case, computed with the generalised slip condition at Kn = 0.25.

A.4. SHEFEX

Fig. A.10 shows the gradient-length local Knudsen number $\mathrm{Kn}_{\mathrm{GLL}}$ for both flow conditions at an angle of attack of 30°. The local Knudsen number is calculated based on the shear stress τ [25]:

$$\mathrm{Kn}_{\mathrm{GLL}} = \frac{\lambda}{\tau/|\boldsymbol{\nabla}\tau|}$$

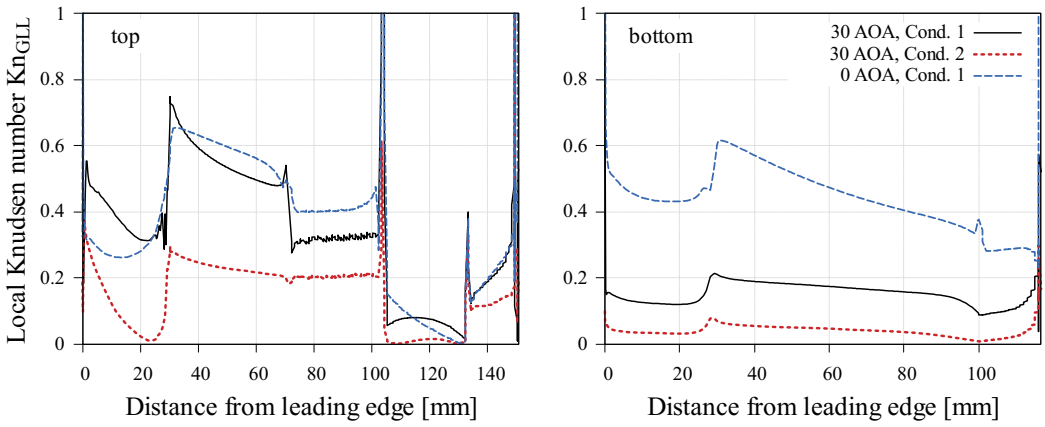

Figure A.10.: Local Knudsen number $\mathrm{Kn}_{\mathrm{GLL}}$ along the surface contour parallel to the symmetry axis of the SHEFEX configuration for all three flow conditions. Here, the local Knudsen number is computed with the Maxwell slip condition but the same trends were observed for the no-slip and generalised slip conditions.

Bibliography

[1] J. D. Anderson Jr. *Hypersonic and High-Temperature Gas Dynamics*. American Institute of Aeronautics and Astronautics, 2nd edition, 2006.

[2] A. J. Lofthouse. *Nonequilibrium hypersonic aerothermodynamics using thedirect simulation Monte Carlo and Navier-Stokes models*. PhD thesis, University of Michigan, 2008.

[3] C.-M. Ho and Y.-C. Tai. Micro-electro-mechanical-systems (mems) and fluid flows. *Annual Review of Fluid Mechanics*, 30(1):579–612, 1998.

[4] N. G. Hadjiconstantinou. The limits of navier-stokes theory and kinetic extensions for describing small-scale gaseous hydrodynamics. *Physics of Fluids*, 18 (11):111301, 2006.

[5] W.-M. Zhang, G. Meng, and X. Wei. A review on slip models for gas microflows. *Microfluidics and Nanofluidics*, 13(6):845–882, December 2012.

[6] J. C. Maxwell. On stresses in rarefied gases arising from inequal-ities of temperature. *Philos. Trans. R. Soc.*, 170(1):231–256, January 1879.

[7] M. Smoluchowski von Smolan. Über wärmeleitung in verdünnten gasen. *Annalen der Physik*, 300(1):101–130, 1898.

[8] A. J. Lofthouse, L. Scalabrin, and I. D. Boyd. Velocity slip and temperature jump in hypersonic aerothermodynamics. *Journal of Thermophysics and Heat Transfer*, 22(1), January 2008.

[9] T. Gökçen, R. W. Maccormack, and D. R. Chapman. Computational fluid dynamics near the continuum limit. *8th Computational Fluid Dynamics Conference*, June 1987. doi: 10.2514/6.1987-1115.

[10] A. Gavasane, S. Sachdev, B. Mittal, U. Bhandarkar, and A. Agrawal. A critical assessment of the maxwell slip boundary condition for rarified wall bounded

flows. *International Journal of Micro-Nano Scale Transport*, 2(2-3):109–116, 2011.

[11] R. Votta, G. Ranuzzi, A. Schettino, and M. Marini. Evaluation of local effects of transitional knudsen number on shock wave boundary layer interactions. *39th AIAA Thermophysics Conference*, June 2007. doi: 10.2514/6.2007-4545.

[12] A. Lofthouse, L. Scalabrin, and I. Boyd. Hypersonic aerothermodynamics analysis across nonequilibrium regimes using continuum and particle methods. *39th AIAA Thermophysics Conference*, June 2007. doi: 10.2514/6.2007-3903.

[13] Kai Luo, Yueming Yang, Hua Liu, Xuewei Xin, and Xuewei Liu. Numerical investigation of hypersonic slip flow. *2015 International Conference on Automation, Mechanical Control and Computational Engineering*, April 2015. doi: 10.2991/amcce-15.2015.354.

[14] D. A. Lockerby, J. Reese, D. Emerson, and R. W. Barber. The velocity boundary condition at solid walls in rarefied gas calculations. *Physical Review E: Statistical Physics, Plasmas, Fluids, and Related Interdisciplinary Topics*, 70 (1), July 2004.

[15] R.W. Barber, Y. Sun, Xiao-Jun Gu, and D. Emerson. Isothermal slip flow over curved surfaces. *Vacuum*, 76:73–81, October 2004.

[16] N. Le, Ch.J. Greenshields, and J.M. Reese. Evaluation of nonequilibrium boundary conditions for hypersonic rarefied gas flows. *Progress in Flight Physics*, 3:217–230, January 2012.

[17] N. T. P. Le, C. White, J. Reese, and R.S. Myong. Langmuir-maxwell and langmuir-smoluchowski boundary conditions for thermal gas flow simulations in hypersonic aerodynamics. *International Journal of Heat and Mass Transfer*, 55(19-20):5032–5043, September 2012.

[18] N. T. P. Le, N. A. Vu, and L. T. Loc. New type of smoluchowski temperature jump condition considering the viscous heat generation. *AIAA Journal*, 55(2): 474–483, 2017.

[19] C. J. Greenshields and J. M. Reese. Rarefied hypersonic flow simulations using the navier-stokes equations with non-equilibrium boundary conditions. *Progress in Aerospace Sciences*, 52:80 – 87, 2012.

[20] S. H. Maslen. On heat transfer in slip flow. *Journal of the Aerospace Sciences*, 25(6):400–401, 1958.

[21] N. T.P. Le, N. A. Vu, and L. T. Loc. Effect of the sliding friction on heat transfer in high-speed rarefied gas flow simulations in cfd. *International Journal of Thermal Sciences*, 109:334 – 341, 2016.

[22] A. Assam, N. Kalkote, N. Dongari, and V. Eswaran. Use of the pressure jump boundary condition in the high speed rarefied gas flows. *ECCM 6 and ECFC 7 Proceedings*, September 2018. URL `http://www.eccm-ecfd2018.org/frontal/default.asp`.

[23] Z. Guo, J. Qin, and C. Zheng. Generalized second-order slip boundary condition for nonequilibrium gas flows. *Physical review. E, Statistical, nonlinear, and soft matter physics*, 89:013021, January 2014.

[24] V. Winkler. Implementation of a slip boundary condition into the dlr tau code and numerical analysis of rarefaction effects on the aerodynamic coefficients of a re-entry configuration. Master's thesis, Justus-Liebig-Universität Gießen, November 2018. (unpublished).

[25] K. Hannemann, C. Hepp, M. Grabe, and V. Hannemann. Numerical analysis of re-entry configuration aerodynamics in the near continuum rarefied flow regimes. *32nd International Symposium on Shock Waves*, July 2019.

[26] S. Metcalf, D. Lillicrap, and C. Berry. *A study of the effect of surface temperature on the shock-layer development over sharp-edged shapes in low-Reynolds-number high-speed flow*, pages 619 – 634. Academic Press, 1. edition, 1969.

[27] Nam T. P. Le, C. White, J. M. Reese, and R. S. Myong. Langmuir-maxwell and langmuir-smoluchowski boundary conditions for thermal gas flow simulations in hypersonic aerodynamics. *International Journal of Heat and Mass Transfer*, 55(19):5032 – 5043, 2012.

[28] G.A. Bird. *Molecular Gas Dynamics and the Direct Simulation of Gas Flows*. Number 42 in Oxford Engineering Science Series. Clarendon Press, 1994.

[29] J.D. Anderson Jr. *Fundamentals of Aerodynamics*, page 62. McGraw-Hill, 5. edition, 2011.

[30] J. N. Moss and G. A. Bird. Direct simulation of transitional flow for hypersonic reentry conditions. *Journal of Spacecraft and Rockets*, 40:830–843, September 2003.

[31] S.A. Schaaf and P.L. Chambre. *Flow of Rarefied Gases*. Princeton University Press, 1961.

[32] E. F. Toro. *Riemann Solvers and Numerical Methods for Fluid Dynamics - A Practical Introduction*. Springer, 1997.

[33] J. D. Anderson Jr. *Computational Fluid Dynamics - The Basics with Applications*. McGraw Hill, international edition, 1995.

[34] F. M. White. *Viscous fluid flow*, page 28. Mechanical engineering series. McGraw-Hill, 2 edition, 1991.

[35] J. Shu, J. B. M. Teo, and W. K. Chan. Fluid velocity slip and temperature jump at a solid surface. *Applied Mechanics Reviews*, 69(2), 2017.

[36] D. Schwamborn, T. Gerhold, and R. Heinrich. The dlr tau-code: Recent applications in research and industry. *European Conference on Computational Fluid Dynamics ECCOMAS*, September 2006.

[37] S. J. Plimpton, S. G. Moore, A. Borner, A. K. Stagg, T. P. Koehler, J. R. Torczynski, and M. A. Gallis. Direct simulation monte carlo on petaflop supercomputers and beyond. *Physics of Fluids*, 31(8):086101, 2019.

[38] S. Plimpton and M. Gallis. Stochastic parallel rarefied-gas time-accurate analyzer (sparta). URL `https://sparta.sandia.gov/`. Accessed: 16.10.19.

[39] V. Hannemann. *Forschungsbericht 97-07: Numerische Simulation von Stoß-Stoß-Wechselwirkungen unter Berücksichtigung von chemischen und thermischen Nichtgleichgewichtseffekten*, pages 46–47. German Aerospace Center (DLR) Göttingen, 1997.

[40] B. van Leer. Towards the ultimate conservative difference scheme. - v. a second-order sequel to godunov's method. *Journal of Computational Physics*, 32:101–136, July 1979.

[41] W. Wagner. A convergence proof for bird's direct simulation monte carlo method for the boltzmann equation. *Journal of Statistical Physics*, 66(3-4): 1011–1044, February 1992.

[42] A. Rohde. Eigenvalues and eigenvectors of the euler equations in general geometries. *15th AIAA Computational Fluid Dynamics Conference*, June 2001. doi: 10.2514/6.2001-2609.

[43] H. J. Kowalsky. *Lineare Algebra*. Walter de Gruyter, Berlin, New York, 9. edition, 1979.

[44] I. N. Bronstein and K. A. Semendjajew. *Taschenbuch der Mathematik*. BSB B. G. Teubner Verlagsgesellschaft, Nauka-Verlag, Leipzig, Moskau, 21. edition, 1981.

[45] K. Fritzsche. *Grundkurs Analysis 2 - Differentiation und Integration in mehreren Veränderlichen*, page 36. Elsevier, München, 1. edition, 2006.

[46] D. J. Mavriplis. Revisiting the least-squares procedure for gradient reconstruction on unstructured meshes. *16th AIAA Computational Fluid Dynamics Conference*, June 2003. doi: 10.2514/6.2003-3986.

[47] T. J. Barth. A 3-d upwind euler solver for unstructured meshes. *10th Computational Fluid Dynamics Conference*, June 1991. doi: 10.2514/6.1991-1548.

[48] Technical documentation of the dlr tau-code release 2017.1.0. Technical report, Institute of Aerodynamics and Flow Technology, Braunschweig/Göttingen.

[49] C.-D. Munz and T. Westermann. *Numerische Behandlung gewöhnlicher und partieller Differenzialgleichungen*, page 228. Springer, 3. edition, 2012.

[50] R. D. Boettcher, G. Koppenwallner, and H. Legge. Flat plate skin friction in the range between hypersornic continuum and free molecular flow. *Progress in Astronautics and Aeronautics, Rarefied Gas Dynamics*, 51:349–359, 1997.

[51] G. Karniadakis, A. Beskok, and N. Aluru. *Microflows and Nanoflows: Fundamentals and Simulation*, page 61. Interdisciplinary Applied Mathematics. Springer, 2005.

[52] G. Koppenwallner. The drag of simple shaped bodies in the rarefied flow regime. *AIAA 20th Thermophysics Conference*, June 1985. doi: 10.2514/6.1985-998.

[53] T. Schlegat and K. Hannemann. Experimental investigation of rarefaction effects on aerodynamic coefficients of slender and blunt re-entry vehicles. *International Conference on High-Speed Vehicle Science and Technology*, November 2018.

[54] K. Hannemann, C. Hepp, V. Winkler, V. Hannemann, T. Schlegat, and M. Grabe. Numerical and experimental analysis of rarefaction effects on aerodynamic coefficients of a slender re-entry vehicle. *International Conference on High-Speed Vehicle Science and Technology*, November 2018.

Erklärung Ich versichere hiermit, dass ich die vorliegende Arbeit ohne fremde Hilfe selbstständig verfasst und nur die von mir angegebenen Quellen und Hilfsmittel verwendet habe. Wörtlich oder sinngemäß aus anderen Werken entnommene Stellen habe ich unter Angabe der Quellen kenntlich gemacht. Die Richtlinien zur Sicherung der guten wissenschaftlichen Praxis an der Universität Göttingen wurden von mir beachtet. Eine gegebenenfalls eingereichte digitale Version stimmt mit der schriftlichen Fassung überein. Mir ist bewusst, dass bei Verstoß gegen diese Grundsätze die Prüfung mit nicht bestanden bewertet wird.

Göttingen, den

(Theresa Hoppe)